Montanuniversität Leoben

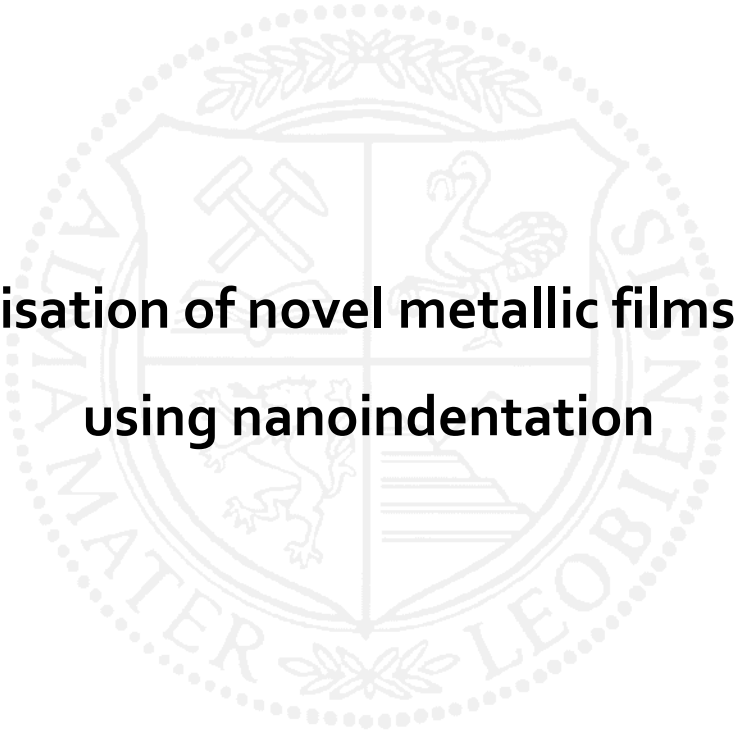

Characterisation of novel metallic films on silicon using nanoindentation

Diploma Thesis

Juliane KAMPICHLER

This thesis has been accomplished at the Department Material Physics, Montanuniversität Leoben in cooperation with the Materials Center Leoben (MCL).

Leoben, 14.09.2017

AFFIDAVIT

I declare in lieu of oath, that I wrote this thesis and performed the associated research myself, using only literature cited in this volume.

Leoben, 14.09.2017

Signature

Financial support by the Austrian Federal Government (in particular from Bundesministerium für Verkehr, Innovation und Technologie and Bundesministerium für Wissenschaft, Forschung und Wirtschaft) represented by Österreichische Forschungsförderungsgesellschaft mbH and the Styrian and the Tyrolean Provincial Government, represented by Steirische Wirtschaftsförderungsgesellschaft mbH and Standortagentur Tirol, within the framework of the COMET Funding Programme, as well as from the FFG, Produktion der Zukunft (Proj. No. 853467), "ProQualiKu" is gratefully acknowledged.

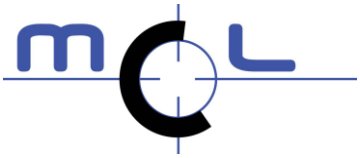

ACKNOWLEGMENT

At the beginning on the part of the Material Center Leoben I would like to thank my supervisor Dr. Roland Brunner, for the chance to work on important fundamental research in the field of characterisation of newly developed material. He continuously encouraged a high level of self-dependence, whereby I learned a lot during this thesis. Furthermore, I like to thank my project colleague Andi Wijaya for our good collaboration during the project and the colleagues from the Material Center Leoben for all their support during my thesis.

My thanks on the part of the university belong to Prof. Dr. Daniel Kiener for his support during this thesis. Even though his time schedule is always very full, he offered important input and found time for me and my thesis. Certainly, a great "Thank you" belongs to everyone at the Department of Material Physics for their support and advice during the work for my thesis, especially Silke Modritsch and Dipl. Ing. Alexander Leitner should be mentioned here.

Moreover, I am indebted to Dr. Verena Maier-Kiener, who sacrificed a lot of her rare spare time for the nanoindentation measurements, as well as for meetings and all nanoindentation related questions during this thesis. Thank you sincerely for your time and support.

Maria Ebner-Eschenbach once said, "During youth one learn, with age one will understand". During this thesis I have learned a lot and understood even more. But my curiosity has not faded and even though it was not easy, I am thankful for having this opportunity. Now I am looking forward to accept new challenges.

Thanks to my family and friends for their support in any situation of my life.

CONTENT

1. INTRODUCTION

Nature is one of the most talented and efficient material designers in our world, therefore the intention of mankind to imitate and recreate those inventions is understandable. Especially in the field of durable lightweight construction and energy absorption nature trusts in its open- and closed-cell structures, as can be seen with the examples of wood, bone or sponge. Those porous structures bear the secret of outstanding performance in the field of mechanical and physical properties, for example high stiffness compared with low specific weight, high gas permeability and thermal conductivity. Hence, interest in foam construction is increasing, which can be seen by new applications for foam constructions in the man-made world in various fields every day, such as applications for biomedical implants [1,2], devices like heat-exchanger substrate or catalysts [3], and actuators [4].

The reason for the usage of open- and closed-cell material depends on four different points, where either one or a combination of those are pushing the development of porous materials. These points are the *morphology of the material*, a required *microstructural metallurgy*, the *necessity of processing* composites and special shaped foams or *economic reasons* like low cost and a high-volume production[5]. Foam constructions can be found in different industries like automotive, aerospace, railway, shipping, construction, sporting equipment and biomedicine.

Open- and closed-cell construction are reasonable solutions to the demand of durable light weight constructions combined with multiple other desired physical and mechanical properties. Nevertheless, for reasonable material design the material behaviour has to be understood, otherwise effective improvements are depending on sheer luck, money and time. While closed-cell macro and micro foams with a high porosity (>70%) and their behaviour are well investigated by Gibson and Ashby [6], the research on open-porous material with a mainly intermediate porosity of 10 to 70% is still underrepresented. Therefore, the possibilities and limitations of characterisation on open-porous material needs to be investigated. In case of this thesis the possibility of nanoindentation is of most interest.

The task for this thesis was to determine Young's modulus and Hardness values by nanoindentation. Nanoindentation gives the possibility to test small dimensions as nanoparticles, small areas of interest in a material e.g. bainit or in case of microelectronic devices thin layers. During the indentation process two parameters, load and penetration depth of the indenter tip, are monitored, from which the Hardness and the modulus can be calculated. Through continuous stiffness measurement technique Hardness and modulus are known for every indentation depth.

For this discourse, we have been provided with a newly developed sintered porous copper material. The layers have been produced through stencil printing and possessed a thickness of 100 µm and lower. As it has been shown by S. Bigl et.al. [7], the main influence during nanoindentation for pure copper is its surface roughness and tilt. Countable papers have been published dealing with nanoindentation problems through roughness and sample tilt [8-11]. Therefore, a structure analysis has been performed to explain the materials behaviour during the indentation. Indeed, the roughness of an open porous material is severe. Therefore, the boundaries for the nanoindentation measurement, but also possible preparation methods to obtain useful surface roughness, will be mentioned in this thesis.

An additional goal was to provide a guideline for production and values for further measurements, which links the porosity and the Young's modulus of porous material. The state of the art method for modulus determination on porous material is the Ashby-Gibson (AG)-model [6], though especially for sintered material the model reveals huge discrepancies [1, 12]. As a result of this work, the correlation of the young´s modulus to the AG-model, its boundaries and other possible models like Hashin-Shtrikman, Mori-Tanaka and the self-consistency method have been investigated.

2. THEORY

2.1. Porous material

2.1.1. Terminology of porous materials

The field of Bionics is trying to implement the systems of nature in the modern technology. Porous systems and its interesting mixture of different valuable material properties are one example for those. In case of porosity it can be distinguished in two different kinds of porosity, open- and closed-porosity. Open porosity describes the state of a connected pore system. With increasing porosity, the possibility of self-contained pores decreases. The composition of the total porosity has been illustrated as can be seen in Figure 1; by B. Schulze in his dissertation [13]. Between 8 and 15% the closed porosity drops significantly and at 30% nearly all pores are open, but only at 45% porosity the statistical possibility of closed pores runs against zero.

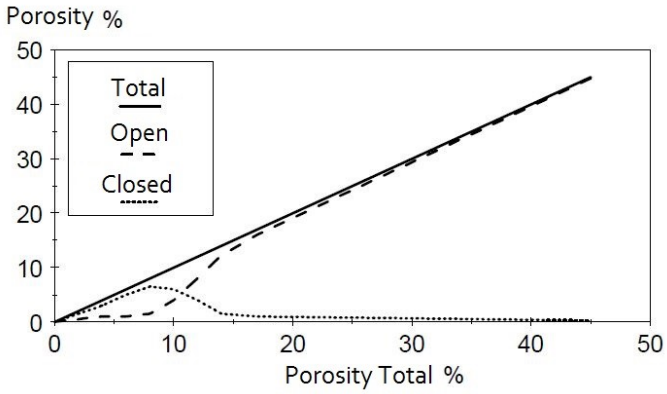

Figure 1; Composition of the total porosity through open and closed pores. Below 10% total porosity the pores are mainly closed. At 15% and up the share of the closed pores is very low, therefore at a percentage of 45% the material can be seen as 100% open porous [18].

During research for this thesis, different definitions of terms in connection with open- and closed-porous material have been found, in order to give a clear definition of the further terms a brief explanation of those should be made. The explanation of the terms used in this thesis accords to the work of J. Banhart [5]. He listed terms based on the different materials matter of states, where dispersant and solvent matter built a matrix. This matrix is shown in Table 1. In the context of porous material, the terms "foam", "cellular solid" and "slurry" might be the most interesting. The term "foam" is often used in different contexts but originally it is only meant for gas dispersions in liquid. The morphology of a foam is described by a closed-cell structure. The base material is always liquid metal and the gas is distributed into the material through casting or mechanical and chemical methods. "Cellular solids", also solid foams,

describe the dispersion of gas in a solid. The base material is in most cases powder, which can either be pressed or applied as slurry. A "slurry" describes a fine solid material dispersed in liquid, if the liquid possesses a high viscosity e.g. polymer resin, the literature also describes it as paste. In case of slurry or paste the material need to be cured after the application, while a pure powder is sintered.

Table 1; Nomenclature matrix for porous material introduced by J.Banhart. The most important terms for the production of porous material have been thickened.

		Solvent		
		gas	liquid	solid
Dispersant	gas	gas mixture	**foam**	**cellular solid**
	liquid	fog	emulsion	gel
	solid	smoke	**slurry**	embedded particles

Cellular solids can possess open- or closed-cell porosity. An open porous material is sometimes revered as open foam, but more accurate is the term "sponge". Depending on the level of porosity, the voids of the material are more or less connected as given in Figure 1. The method, which is used to process the porous material influences the kind of porosity and the surface structure. Surface roughness has to be taken in consideration for material with open porosity as well as for processed material after cutting.

The applications can differ from simple structural to simple functional and the porosity shows different behaviour for open, particular open and closed cell structure. Hence, a broad variety of applications is possible [5], as can be seen in Figure 2. The porous sintered copper material was mainly used as heat exchanger. From the application chart it can be seen, that no special structure is necessary, because the application is mainly functional and requires an open porosity.

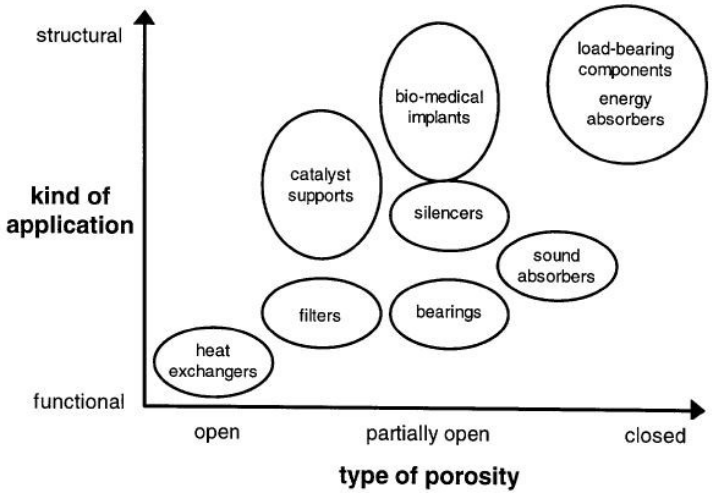

Figure 2; Different porosity structures are needed to obtain various applications. In the application chart, the required porosity types for different applications are illustrated. The material for this thesis was mainly used as heat exchangers [5]

2.1.2. Processing of cellular solids

To process cellular material the starting metal can be in the state of vapour, liquid, powder or ions, as given in Figure 3. Every state leads to different method options, but the two brighter boxes of starting materials, liquid and powder, are the most common, which can be seen due to the numerous listed techniques.

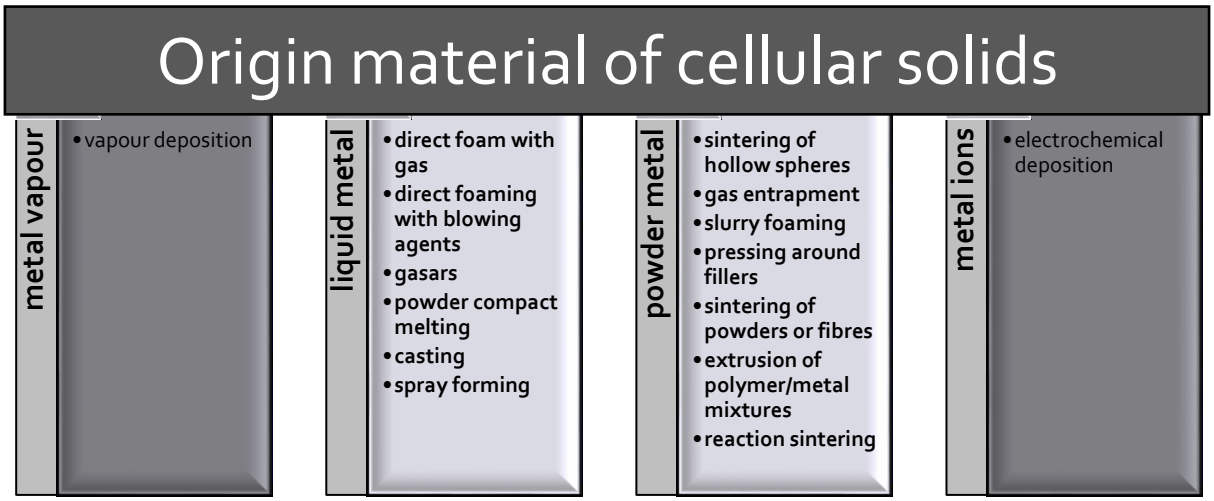

Figure 3; Cellular metal production can be accomplished with metal in four different phases (vapour, liquid, powder and ions). Most processes are foaming techniques and based on liquid or powder metal.

Fabrication of porous copper can be accomplished in several ways [14–17]. The latest developments are focusing on ink-jet applications, due to its low cost, low waste production and easy processing. Countable research is running on finding the ideal paste composition because it's affecting the grain size distribution, porosity and the annealing behaviour of the material. The material for this thesis was produced through stencil printing, it is alike ink jet technology, but with more material application in one run. Stencil printing (SP) is a low-cost process to produce conductive layers and interconnects with a high yield per time. The technique originates on the screen printing process which is best known in the textile industry for t-shirt prints. To process the material, it has to possess a pasty condition. Therefore, SP is commonly used with solder or so called isotropic conductive adhesives (ICA). Those ICAs are a mixture of metallic conductive particles (Ag, Cu, Au, Ni or coated particles) and a polymeric resin with a minimum percentage of 25% conductive particles [18]. A copper ICA was used to produce the material for this thesis. The exact composition is not known. In the SP process a so-called squeegee, an angled blade, is settled on a stencil with a defined pressure and pulled across the stencil´s aperture with a defined velocity, as can be seen in Figure 4. After applying the paste on the substrate, the material is set to cure. Throughout curing the resin diminishes and the particles get in contact, where a sponge-structure resides. For material produced with

space holder techniques it has been observed that the residual surface of the sponge possess micro-pores [12]. As a consequence, the resin and paste selection can influence the mechanical behaviour noticeably.

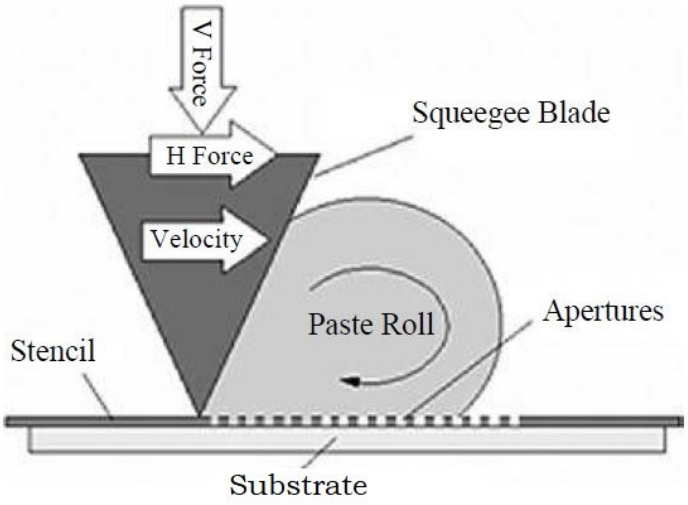

Figure 4; Stencil Printing. A squeegee is pulled over a preproduced aperture. The holes in the stencil are filled with an ICA. One stencil can be used multiple times. Stencil Printing allows high production volume at low costs. [18]

Further factors have effects on the printing performance, like stencil production, printing material, parameters and conditions and the environment [18]. This study is focusing on a comparison of different carrier resins. The material provided for this research study was processed through SP with an ICA consisting of copper particles and two different resins. Next to an influence on the pore structure, the paste also has an influence on the bonding strength between the particles [19]. Therefore, the mechanical properties of the copper material are of utmost interest and have been investigated through nanoindentation.

2.2. Copper

2.2.1. Introduction

Copper (lat. cuprum) was named after its place of ancient occurrence, Cyprus. It is a ductile metal with a reddish appearance. Copper counts to the group of precious metals and can thus be found in solid form. Therefore, and due to the fact that it can easily be casted, copper was already used in prehistoric time in beads and pottery. The problem with pure copper is that it is too soft. Through addition of further metals, like tin and zinc, the alloys gain an increased strength and hardness. Thus, items like weapons and tools were possible and very important for the bronze era [20].

Next to its appearance as pure metal, copper ores like Chlakopyrit ($CuFeS_2$), Bornite (Cu_5FeS_4) and Malachit $CuCO_3.Cu(OH)_2$ are the main supplier for the increasing demand of copper. The sulphide ores are the most common and can be purified through converting into blister copper followed by electrolytical refinement out of casted anode material or the hydrometallurgical way with electrolytical production out of the electrolyte.

2.2.2. Material Properties of pure copper

The mechanical, thermal and physical properties of pure copper as used in the experiments and calculations are mentioned in Table 2. The moduli are calculated on the basis of the Young's modulus mentioned by S. Bigl et all. [7]

Table 2; Properties of copper based on [7] for * marked values and [12] *for the rest*

Parameters	Values	Parameters	Values
Atomic number	29	***Elect. Conductivity***	$58*10^6$ S/m
Crystal structure	Face cent. cubic (fcc)	***Heat Conductivity***	401 W/mK
Density	8.92 g/cm^3	***Poisson's Ratio****	0.32
Melting Point	1357.6 K (1084.4°C)	***Youngs' Modulus****	110 GPa
Sintering temperature	600 – 900°C	***Shear Modulus****	41.67 GPa
Sp. Heat capazity C_p	385 J/kgK	***Bulk (compr.) modulus****	101.85 GPa

The advantages of copper consist of its high thermal and electrical conductivity and corrosion resistance. For pure copper applications corrosion resistance is one main property. When copper is getting in contact with air or a mild alkaline solution an inert patina is built and prohibits the material from corroding. Consequently, copper is well used for chemical constructions and domestic plumbing. The electrical conductivity of aluminium is only in comparison with the weight better than the one of copper, whereas compared to the volume copper is undeniable leading [21]. An additional advantage of copper is the resistance against electro-migration [22], whereas aluminium suffers severely under the influence of electro migration. As a consequence, pure copper is found in application in the field of electrical wiring and microelectronics ,e.g. wires and conductor strips.

2.2.2. Modulus definition of pure copper

One major problem with pure copper is the high dependence of the modulus on the layer orientation. Values from 70 to 130 GPa can be measured. Through an electron beam scatter diffraction (EBSD) analysis of the stencil printed porous material, a part of the ongoing dissertation of A. Wijaya [23], it has been verified, that there was no preferred plane orientation of the copper grains for the samples of interest.

The case of a randomly orientated polycrystalline copper layer has been discussed by S. Bigl et al. [7], due to the random texture an average Young's modulus (*E*) of 109 GPa has been assumed. For this thesis, the modulus has been oriented to that paper and was set at 110 GPa. The shear (*G*) and compression (*K*) modulus have been calculated from this value and the given Poisson's ratio (ν). For the nanoindentation the Young's modulus and the Poisson's ratio are the most important input parameters. Below the different calculations for the moduli used in this thesis are listed.

$$K = \frac{E}{3(1-2\nu)} \qquad G = \frac{E}{2(1+\nu)} \qquad E = \frac{9}{\frac{1}{K}+\frac{3}{G}} \tag{1}$$

2.2.3. Poisson's ratio of porous copper

In a composite system material-air, the Poisson's ratio of air is strongly related to the geometry of the foam structure, not the porosity itself. Therefore, values from -0,7 to 0,5 can occur [6], which leads to difficulties in the measurement of the ratio and usage of methods relying on the Poisson's ratio, like nanoindentation. To annihilate the uncertainty of the Poisson's ration the material was infiltrated through a material with known properties.

2.3. Mechanical Models

2.3.2. Introduction

The most used model to explain mechanical behaviour of foam material is the Ashby-Gibson (AG) model. But foams are nothing less than a composite of material and air. A composite is a material which consists of two or more phases. The industry is interested in models to predict composite response on mechanical stress, therefore various attempts for defining a reasonable calculation model can be found [24]. On one side, there are sophisticated and more or less complex models like the Mori-Tanaka (MT) model, self-consistency (SC) model, the generalised self-consistency (GSC) model and the three-phase (TP) model, but there are also the models which are only relating on the material properties and volume fraction [25], like the Ashby-Gibson (AG), Voigt-/ Reuss- and Hashin-Shtrikman (HS) model. Those three will be discussed in more detail now.

2.3.3. Ashby-Gibson

The Ashby-Gibson model was defined for open and closed cells. Both models are based on a cube model, where in case of an open cell the corners are connected through bulks along the edges and in case of the closed cell the side planes are closed as well (Figure 5). For more stability, every next plane is shifted by a half side length [6].

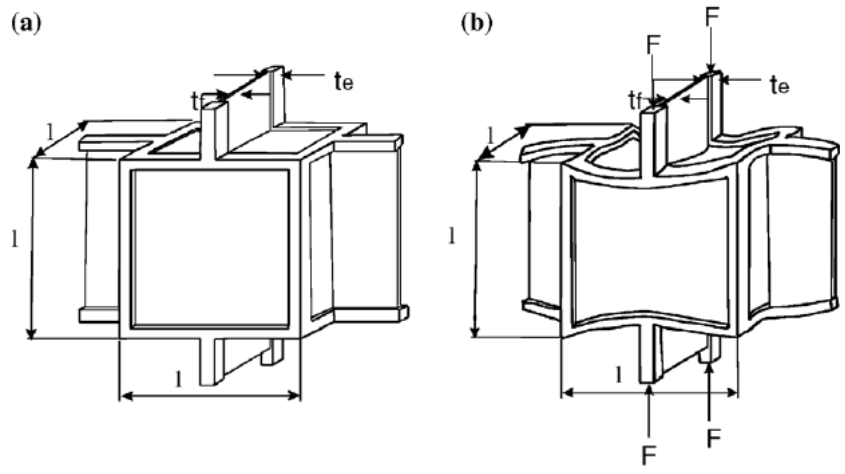

Figure 5; a. Ashby-Gibson Cube Model b. Ashby-Gibson Cube Model under load. For more stability, the next cubes are always shifted by half a side length. As a result, the load is always applied in the middle of the edge beams [6].

Discrepancies regarding the predicted AG-model for sintered materials are documented in various papers [1 ,12]. There it is shown, that the AG-model is similar for sintered material with a porosity of 80% and more, but below that the experimental values and the theoretical values deviate noticeable from each other. For porosities below 20% there's a switch from mainly open cell porosity to mainly closed cell porosity. Therefore, the AG-model should be changed as well. As a reason for this deviations B. Wang et al. [19] reconsidered that cell edges and faces are declared as homogeneous solids, whereas through sintering micro-pores occur at the surface. As a result, the binding between the particles might be reduced.

The open cell model is easily calculated through the standard beam theory and the universal cube model (Figure 5.b.), which leads to equation 2. Through the model the Youngs's modulus of the cellular solid (E^*) can be calculate. It is basing on the Young's modulus of the bulk material (E_S) and the ratio of the cellular solid density to the density of the bulk material ($\frac{\rho^*}{\rho_S}$).The constant C_1 is commonly taken as 1 and the constant C_2 possess the value 3/8.

$$\frac{E^*}{E_S} = C_1 * \left(\frac{\rho^*}{\rho_S}\right)^2 \qquad \frac{G^*}{G_S} = C_2 * \left(\frac{\rho^*}{\rho_S}\right)^2 \tag{2}$$

For the closed cell model, the calculation is quite more complicated. The matrix material along the edges and the residual material in the planes have to be considered separately. Φ is between 1 and 0 and describes the material ratio in the edges, while $(1-\Phi)$ describes the material ratio left for the planes. This is required due to two deformation mechanisms, first an edge bending and second stretching of the side planes. The pressure inside the cell will be neglected and the modulus can be calculated, as given in equation 3. The plane volume is in most cases marginal in comparison to the edge volume, therefore the

second term can be neglected. The constant *C1* is the same as in equation 2.

$$\frac{E^*}{E_S} = C_1 \Phi^2 \left(\frac{\rho^*}{\rho_S}\right)^2 + C_1{}'(1-\Phi)\frac{\rho^*}{\rho_S} \tag{3}$$

2.3.4. Reuss-Voigt

The physical model behind Voigt and Reuss can be explained through a laminar compound with two different moduli. According to their laminate orientation due to the pressure, either the elongation of the material can be constant, which is represented by the Voigt-model, or the tension can be constant, which is represented by the Reuss-model (Figure 6)

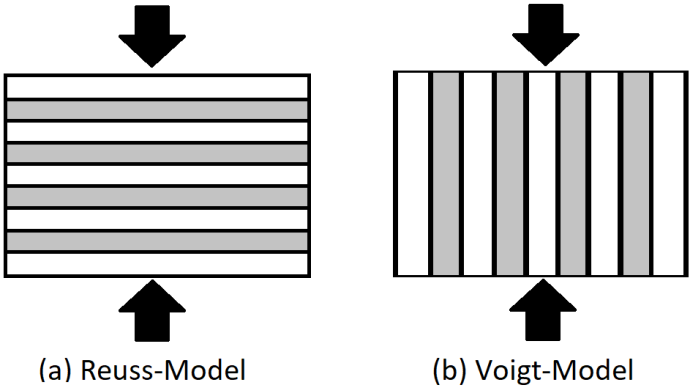

Figure 6; (a) Reuss-Model (σ=const.) and (b) Voigt-Model (ε=const.). The black arrows symbolise the direction of the force. Those are most simple models for composite structures and therefore give the upper and lower limit of mechanical properties of composites.

The material consists of in-plane isotropic material and an anisotropic macrostructure. Broadly speaking Voigt behaves like a series circuit and Reuss behaves like a parallel circuit. Which results in a material behaviour explained trough following formula, Voigt explained by equation 4 and Reuss by equation 5. E^* is the Young's modulus of the compound, whereas E_1 and E_2 are the Young`s moduli of the two participating materials. The two variables c_1 and c_2 are defined as the volume ratio of the two materials.

$$\mathrm{E}^* = E_1 c_1 + E_2 c_2 \tag{4}$$

$$\frac{1}{E^*} = \frac{c_1}{E_1} + \frac{c_2}{E_2} \tag{5}$$

Thus, those are outer extreme models of composite material structure. As a result, the Voigt and Reuss model give the limits for all effective characteristics. Due to the fact, that every alteration of those models leads to values in between those limits. The advantage of the Voigt and Reuss limits is their simplicity. Through an extremum principle the two outer limits for a heterogenic material can be calculated.

Nevertheless, there's also the disadvantage hidden, because the limits are very far apart from each other. In addition, it has to be mentioned that those models neglect the Poisson's ratio [25].

2.3.5. Hashin-Shtrikman

The Hashin-Shtrikman (HS) model was specially designed for heterogeneous materials by Hashin and Shtrikman [26]. Here the volume is filled with different sizes of coated spheres, because only the ratio from sphere radius to coating radius is defined [27]. Every sphere is uninfluenced by the others. As a result of the predefined round shape voids inside the model can occur. This leads to a structure like in Figure 7. Where the grey spheres are referred as inhomogeneities and the white sphere around the inhomogeneity referred as matrix material.

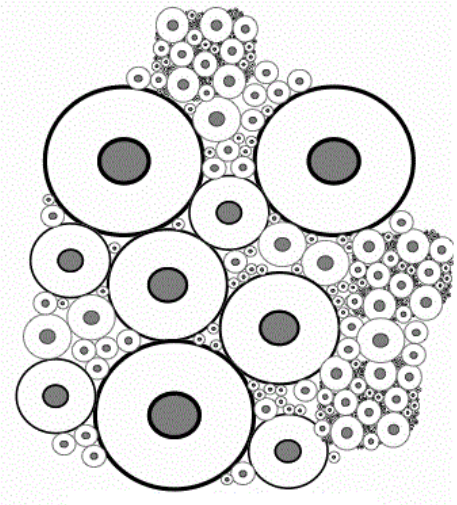

Figure 7; HS model. The ratio between inner and outer circuit are constant. The material consists out of an inhomogeneity (grey) and a matrix (white). An upper and lower limit can be calculated through switching the inhomogeneity and the matrix. Lower limit describes the case of a stiff inhomogeneity and a soft matrix, with the upper limit it is the other way around [28]

The compression modulus of the composite (K^*) can be explained via Equation 6. The formula has been taken from [25] and then been transformed to Equation 7. *K* is the bulk modulus and *G* is the shear modulus, *c* describes the volume fraction of the material. The indices **M** stand for properties belonging to the matrix and **I** for the properties belonging to the inhomogeneity.

$$K^* = K_M + \frac{c_I}{\left(\frac{1}{K_I - K_M} + \frac{3c_M}{3K_M + 4G_M}\right)} \tag{6}$$

$$G^* = G_M + \frac{c_I}{\left(\frac{1}{G_I - G_M} + \frac{6c_M(K_M + 2G_M)}{5G_M(3K_M + 4G_M)}\right)} \tag{7}$$

The advantage of the HS model is, that it delivers an upper and a lower level. Those are defined through the assembly of matrix and inhomogeneity. The lower limit describes the model where the

inhomogeneity is stiffer than the matrix, for our model given as copper for the inhomogeneity and epoxy resin as matrix material. Whereas the upper limit describes it the other way around [26]. Between the HS-limits the composition of the structure changes. At the lower limit 100% of the inhomogeneity consisting of copper, at the upper limit 100% of the inhomogeneity consisting of epoxy. In the middle between the limits the matrix and the inhomogeneity consisting out of 50% copper and 50% epoxy. The field of possible material properties becomes smaller compared to the previous model of Voigt and Reuss. Nevertheless, the model itself is not very accurate compared to the material structure of open-porous copper samples. For more accurate material structure models, one has to switch to more sophisticated models, like the Mori-Tanaka (MT) model and the self-consistency (SC) model. These need an increasing investment in calculation.

2.3.6. Mori-Tanaka

The Mori-Tanaka (MT) model is related to the HS-Model, if the geometry of the inhomogeneities is considered round within an isotopic matrix [23, 24]. The difference between the HS and MT model is that the matrix shape is not predefined, therefore no voids between the areas occur. The inhomogeneities in the different areas are uninfluenced by each other like the spheres of the HS model. In Figure 8 a sketch of the MT model is shown. In each area is one inhomogeneity (grey).

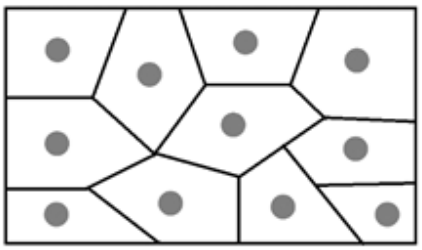

Figure 8; Sketch of the Mori-Tanaka Model. In every area one inhomogeneity (grey) is placed. The area shape itself is in the calculation seen as an infinite expanded area, therefore none of the areas are influencing each other.

The MT model equations have been calculated as mentioned in Equation 8 and 9. *K* is the bulk modulus and *G* is the shear modulus, *c* describes the volume fraction of the material. The indices **M** stand for matrix and **I** for the inhomogeneity. The two geometry factors α and β for round inhomogeneities are listed under Equation 10.

$$K^* = K_M * \left(1 + \frac{c_I * (K_I - K_M)}{K_M + (1 - c_I) * \alpha * (K_I - K_M)}\right) \tag{8}$$

$$G^* = G_M * \left(1 + \frac{c_I * (G_I - G_M)}{G_M + (1 - c_I) * \beta * (G_I - G_M)}\right) \tag{9}$$

$$\beta = \frac{6*(K_M+2*G_M)}{5*(3*K_M+4*G_M)} \qquad \alpha = \frac{3*K_M}{3*K_M+4*G_M} \tag{10}$$

If the shape of the inhomogeneities is not round the local distribution have to be considered as well, which leads to an alteration of the factors α and β. In the case of not round inhomogeneities the calculation effort increases tremendously. The MT model also only delivers one lower limit and no upper limit. This might only be useful if the material behaviour follows the model exactly like a trendline.

2.3.5. Self-consistency model

The self-consistency model is the most realistic model of the here introduced models. In this model, the inhomogeneities are looked at one by one in a matrix, they are influencing each other in the residual distortion field [24]. The properties of the matrix are homogeneous but unknown.

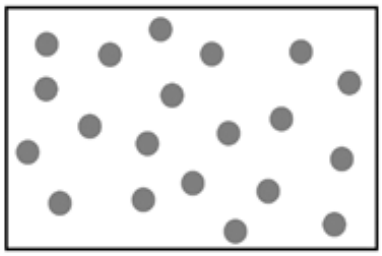

Figure 9; Self-consistency Model. The inhomogeneities inside the matrix are interacting with each other. The distortion is calculated from inhomogeneity to inhomogeneity.

To calculate the effective matrix properties the effective elastic properties are needed, which leads to an implicitly formula. After transformation, this results in a non-linear algebra equation. This way, the matrix properties and all the inhomogeneities get calculated into a on itself-consisting model. Again, *K* is the bulk modulus and *G* is the shear modulus, *c* describes the volume fraction of the material. The indices **M** stand for matrix and **I** for the inhomogeneity.

$$K^* = K_M + c_I * (K_I - K_M) * \left(1 + \alpha * \left(\left(\frac{K_I}{K^*}\right) - 1\right)\right)^{-1} \tag{11}$$

$$\alpha = \frac{3K^*}{3K^*+4G^*} \tag{12}$$

$$G^* = G_M + c_I * (G_I - G_M) * \left(1 + \beta * \left(\left(\frac{G_I}{G^*}\right) - 1\right)\right)^{-1} \tag{13}$$

$$\beta = \frac{6*(K^*+2G^*)}{5*(3K^*+4G^*)} \tag{14}$$

To eliminate the effective elastic parameters, the shear modulus is transformed to an equation, which only includes c_I, K_I. K_M, G_I and G_M, but no longer G^* or K^*.

$$K^* = \frac{4*G^**(c_I*(K_I-K_M)+K_M)+3*K_IK_M}{4*G^*-3(c_I*(K_I-K_M)-K_I)} \tag{15}$$

$$\beta = \frac{6*\left(8G^{*2}-2G^**(c_I*(K_I-K_M)-3K_I-2K_M)+3K_IK_M\right)}{5*(16G^{*2}+12G^**(K_I-K_M)+93K_IK_M)} \tag{16}$$

Those two equations are inserted into Equation 13. It has been tried to calculate the self-consistency model with MatLab R2016b but fail because it results in a polynomial of fifth order. Polynomials of fifth order have no algebraic solution (Abel-Ruffini theorem). For a possible solution transformation and predictions would be needed, however this would exceed the content of this thesis. (APPENDIX C)

2.3.6. Calculation of the models

All the models have been calculated for the model of an epoxy matrix and copper inhomogeneities, except the additional calculation of the HS upper limit, where the matrix was stated as copper and the inhomogeneity as epoxy resin. The two-phase models have been calculated with the values in Table 3. The Young's modulus and the Poisson's ration of epoxy have been taken from a book by P.K. Sinha, "Composite Materials And Structure"-Chapter 4 [29].

Table 3; material properties necessary for the two-phase-model calculations. The inhomogeneity, copper (I) and the matrix material, epoxy (M).

Index	Material	E-Mod [GPa]	G-Mod [GPa]	K-Mod [GPa]	Poisson
I	copper	110	41.67	101.85	0.32
M	epoxy	3.45	1.28	3.83	0.35

As shown by A. Kraatz in his dissertation [24] a calculation for the system air and copper, would be possible too, but here again the problematic with the unknown Poisson's ration and moduli of air has an noticeable effect on the model calculation.

2.4. Nanoindentation

2.4.1. Introduction

Depth-sensing indentation, also known as nanoindentation gives the possibility to measure the elastic and inelastic behaviour at once. Next to the Young's modulus and Hardness characterisation of strain-rate sensibility [30], fracture toughness, stiffness and thermal drift [31] can be investigated. The indentation measurement can be accomplished through different tip designs e.g. spherical, three sided pyramid (cube corner or Berkovic) or a flat punch [32].

2.4.2. Continuous stiffness measurement

The nanoindentation measurements have been performed utilising continuous stiffness measurement (CSM). This brought the advantage of constant monitoring of the load against the indentation depth [33]. Hence, instead of just one value per measurement, as presented by Oliver and Pharr [34] a continuous data history is generated. This adds the further advantages, that CSM minimise the indentation size effect and surface roughness influence on the measurement, through statistical treatment [35]. The mechanism behind CSM is an oscillation of the indenter tip in only one plane, which results in a the calculation of a simple-harmonic oscillation with the possibility of damping. The CSM oscillation formula includes a mass (m) regarding the indenter, a damping coefficient (D) and a stiffness coefficient (K). The mass is oscillating at a defined frequency (ω) and amplitude (F_o). Through contact with the surface a phase shift (Φ) occurs and is measured by the amplifier together with the amplitude of the displacement response (z_o).[31].

$$-m\omega^2 + iD\omega + K = \frac{F_0}{z_0}(\cos\Phi + i\sin\Phi) \tag{17}$$

Equation 17 can be separated in a real part (18) and an imaginary part (19)

$$\frac{F_0}{z_0}\cos\Phi = K - m\omega^2 \tag{18}$$

$$\frac{F_0}{z_0}\sin\Phi = D\omega \tag{19}$$

The dynamic compliance z_o/F_o is necessary to be calculated once for the indenter in free hanging state and another time in contact mode. To receive the dynamic compliance Equation 18 and 19 have to be squared and added (Equation 20). Finally Equation 20 has to be solved for z_o/F_o, resulting in Equation 21.

$$\left(\frac{F_0}{z_0}\right)^2(\cos\Phi^2 + \sin\Phi^2) = (K - m\omega^2)^2 + (D\omega)^2 \tag{20}$$

$$\frac{z_0}{F_0} = \frac{1}{\sqrt{(K-m\omega^2)^2+(D\omega)^2}} \tag{21}$$

Figure 10.a. is an exemplary CSM load curve. The mean values follow a standard load curve, but through the oscillation of indenter, additional micro load curves are applied. For each micro-loading, a contact stiffness value can be generated similar to the Oliver and Pharr method, as seen in Figure 10.b. The difference between Oliver Pharr and CSM is that instead of the contact stiffness K_c the contact stiffness S is used. S is only relying on load and displacement data [34], whereas CSM has a quite more complicated formula, as can be seen in Equation 22.

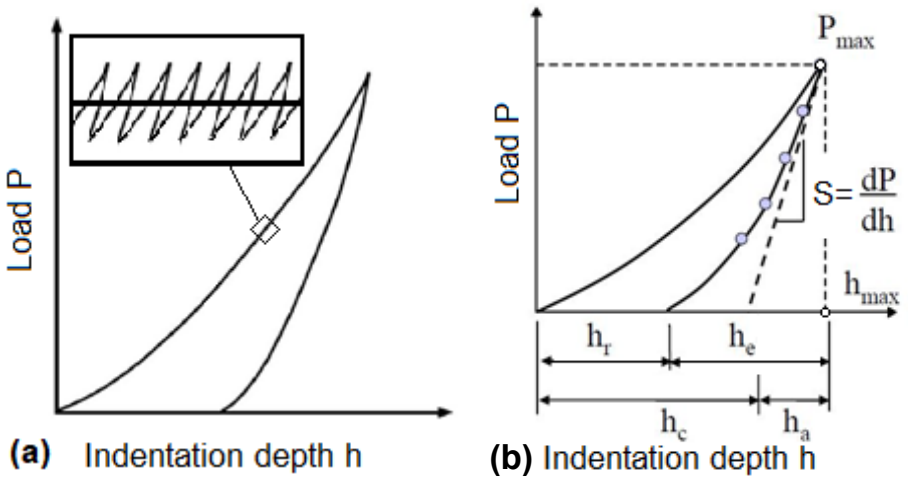

Figure 10; Display of two load curves, (a) CSM load curve, oscillation along the load curve, leading to stiffness values along the entire loading time (b) Stiffness determination from an load curve performed by Oliver-Pharr method.

For CSM the contact stiffness (K_C) is needed instead of the semi-static contact stiffness *S* used for Oliver-Pharr method. K_c is based on the frame stiffness (K_f) and the behaviour in non-contact position [31].

$$K_C = K_f \frac{\left[\frac{F_0}{z_0}\cos\Phi - \left(\frac{F_0}{z_0}\cos\Phi\right)_{free-hanging}\right]}{K_f - \left[\frac{F_0}{z_0}\cos\Phi - \left(\frac{F_0}{z_0}\cos\Phi\right)_{free-hanging}\right]} \tag{22}$$

After determining K_C, it is possible to calculate, together with the two monitored parameters load *(P)* and displacement *(h)*, the contact depth *(h_c)*. The formula is completed by the factor ε, a geometric constant.

$$h_C = h - \frac{\varepsilon P}{K_c} \tag{23}$$

For the final calculation of Hardness *(H)* and the reduced Young's modulus *(E^*)* the contact area *(A)* is necessary. The contact area is depending on the geometry of the indenter tip and the indentation depth. In this thesis, a Berkovich tip was used and most of the measurements have been performed with an indentation depth < 2 µm. For a perfect Berkovich tip (theoretical tip value of 24.56) A is calculated as can be seen in Equation 24. *C* is a constant depending on the indenter tip and is defined through a pre-indent on known material e.g. fused quartz. For perfect Berkovic tips the value is settled at 150 nm [36].

$$A = 24{,}56\ {h_C}^2 + C\ h_C \tag{24}$$

Finally, the Hardness *(H)* and the reduced Young's modulus *(E^*)* can be calculated. Both of these are affected by the stiffness K_c. In the case of the Hardness K_c is indirectly included, because it is contained in *A* and for E^* it is directly included and again indirectly included through A in the formula [31].

$$H = \frac{P}{A} \qquad\qquad E^* = \frac{\sqrt{\pi}}{2}\frac{K_C}{\sqrt{A}} \tag{25}$$

2.4.3. Roughness influence on Hardness and Young's Modulus

Surface roughness, depending on the porosity and tilt influence on nanoindentation are topics with increasing awareness every year. This is also linked to the interest in development of new open-porous applications. Roughness can influence the measurement directly or indirectly, because even the tip geometry has an influence on the analysis, as it is outlined by S. Bigl et al. [7]. If the tip geometry represents the roughness shape more or less, such conditions can lead to overestimation of Hardness and modulus. While S. O. Kuchevey et al. [32] is researching the fracture behaviour of low-density brittle nanoporous material with different nanoindentation tips, Laurent-Brocq et al. [8] is focusing on different roughness and tilt stages measured by a Berkovich tip (Figure 11.a.). She recommended three criteria to obtain a sufficient Hardness measurements with deviations below 10%. First the indentation depth h_C should be > 20x arithmetic roughness (Ra), then a tilt angle below 2% is preferred and finally they advise that the roughness between the indents should never increase over 50%. Additional work was spent on finite element analysis of the roughness influences [10]. Varieties of tilt have been investigated by M.S. Kashani et al. [9], confirmed that a tilt of 5° underestimates the area with 8% and due to that an overprediction of Hardness with 8% and 4% for the Young's modulus occurs. Furthermore L. Cheng et al. [11] declare that if roughness is present, the effect of an increased tip radius is difficult to estimate, because the roughness effects are too strong (Figure 11.b.)Those simulations have been done with an Berkovich tip. As a consequence, the rough surface of the open porous material needs to be investigated to better understand the achieved nanoindentation curves and values. The evaluation of the surface roughness in this thesis is expressed through 3D roughness parameters.

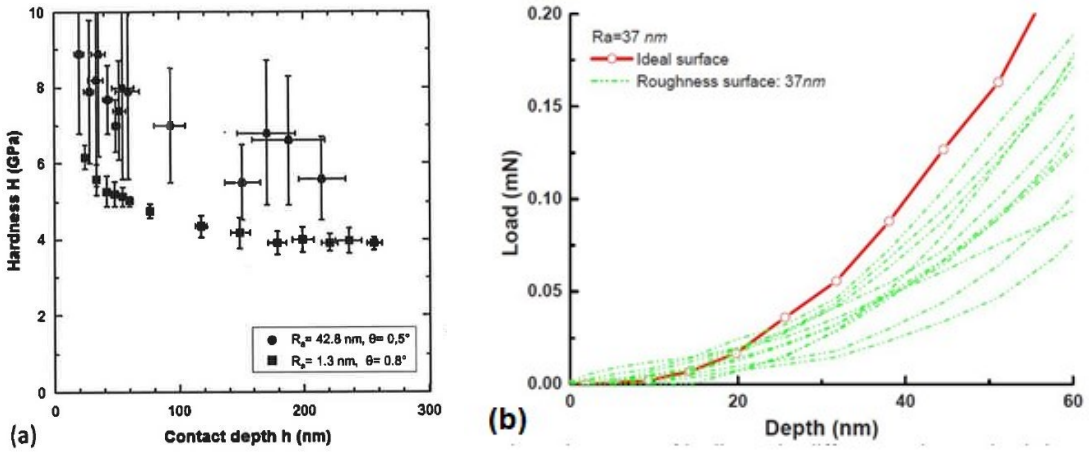

Figure 11; Deviations and spread through surface roughness a.) Hardness [8] *and b.) on the load-displacement curve* [11].

2.4.4. 3D Roughness parameters

Since 1990 the EU established a research group for the development of new characterisation parameters for roughness in 3D. Finally, the research group postulated the "Birmingham 14", which has been written down in the ISO 25178 [37].

The measurement of the 3D structure can be accomplished by using contacting method or optical method. For the contacting method a tapping needle, in most cases diamond, screens a linear profile of the surface and continues in parallel order. At least the data is summarised into a topological information of the surface. This method is time consuming and not suitable for soft material, because it can lead to residual damage. The optical method operates with spot sensors or field sensors (CMOS-Chip or CCD). The system uses either interferometry, autofocus or the often-used confocal chromatic sensors [38].

Additional to the height parameters based on the linear 2D roughness parameter, further structural and functional parameters had been included, to sufficiently describe the 3D structure of the surface. The parameters can be divided into five main groups based on their focus on geometry, structure and functionality[37–40]. A list of all parameters and the group they belong to is given in Table 4.

Table 4; List of all the 3D Roughness Parameters and the group they belong to, according to the ISO 25178 [37]*. The main focus for the application is set on the height and functional parameters*

3D Roughness Parameters -BIRMINGHAM 14				
HEIGHT	**SPATICAL**	**HYBRID**	**FUNCTIONAL**	**STRUCTURAL**
Sa, arithmetic mean height **Sq,** root mean height **Sp**, maximum peak height **Sv,** maximum dale height **Sz,** maximum height **Ssk,** skewness **Sku**, kurtosis	**Sal,** autocorrelation length **Str,** Texture-aspect ratio	**Sdr**, developed interfacial area ratio **Sdq**, root mean square gradient	**Spk**, reduced peak height **Svk**, reduced dale height **Sk,** core roughness **Smr1,** peak material portion **Smr2**, dale material portion	**Spd,** Peak density **Spc**, peak curvature **Additional algorithms:** Watershed, Wolf pruning, Closed and open areas;

The open-porous sintered copper material analysed in this thesis shows a functional application (as shown in Figure 2). Therefore, the two groups of the height and functional parameters are of most interest in this thesis. The **height parameters** are similar to the well-established 2D parameters. The arithmetic mean height (Ra) and the root mean square height (Rq) converted into the 3D parameter Sa and Sq. The values for Sp, Sv and Sz are not that easily converted due to their way of calculation. But the relation

between them is still the same (Sz = Sp+Sv). The Ssk describes the height distribution in comparison to the average plane. It can be above, under or symmetrical to the plane. The kurtosis describes the surface. When Sku > 3, then one or several points on the surface appear spiked, while a Sku < 3 appears as a squashed surface. The higher the value, the shaper the peak.

The **functional parameters** focus on the functional structure behaviour, like crests for contact mechanics, striations for lubrication or cooling and the core area for maximum bearing loads. The most important tool is the Abbott-curve (Figure 12.a.), where the material ratio of the surface is drawn in relation to the height of the cross-section. In Figure 12.a. the determination of the core roughness (Sk), reduced peak height (Spk), reduced dale height (Svk), as well as the peak material portion (Smr1) and the valley material portion (Smr2) are described. Sk gives the residual roughness of a load bearing surface after an initial attrition process. Additional to the parameters itself the shape of the Abbott-curve also gives qualitative information about the roughness profile, as can be seen in Figure 12.b. A specific surface shape (the roughness profile), given in column 1, cause a defined Abbott-curve shape, given in column 2.

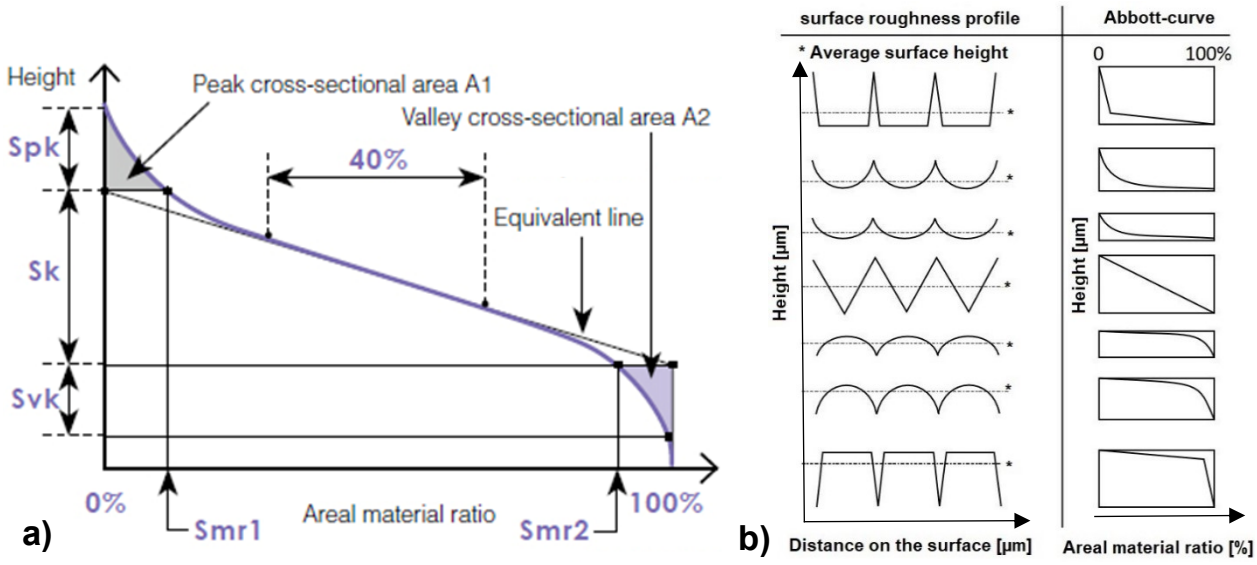

Figure 12; The Abbott-curve; a) Functional parameters and their way of determination from the Abbott-curve. b) Different surface structures/roughness profiles causes characteristic Abbott-curves. Therefore, The Abbott-curve shape already gives a qualitative estimation of the roughness profile.

The groups of **spatial, hybrid** and **structural parameters** will not be explained in detail. But for structural applications they can deliver useful information. Spatial parameters for example, describe the structural behaviour of the surface. The values are determined through the autocorrelation function. The function compares the similarities of the surface, to look for preferred directions. As example, a function value of zero is given for blasted surfaces, while milled surfaces show directional texture. The main concern of the hybrid parameters is the surface gradient. The value for Sdq is between zero (even surfaces) and 1

(roughness flanks with 45°). Whereas, the structural parameters base on techniques of the geology and try to explain the topology of the surface through parameters and algorithms.

2.5. Preparation

2.5.1. Introduction

In order to generate sufficient values during the nanoindentation measurement for open-porous sintered material, due to extreme roughness, preparation was necessary. For nanoindentation and material characterisation a low roughness, small amount of micro deformation and a limited heat transfer into the material are preferred. Otherwise the structure which might appear is different from the original material, due to mechanical (e.g. mechanical tension, deformation), thermal (e.g. phase transformations, diffusion) or electro-chemical (e.g. corrosion, impurities) input. The material hardness effects the thickness of the affected layer. The affected layer consists out of a rough zone and major and minor deformations. Harder material possesses a smaller affected zone, than soft material. To again obtain the true material, preparation is necessary. The term "preparation" includes all the steps from sample pre-preparation, to preparation and the final follow-up treatment [21]. In Figure 13 the preparation procedure is illustrated. Every main point is consisting of two minor steps, the main purpose of preparation, next to obtain a sufficient roughness, is the annihilation of the affected layer.

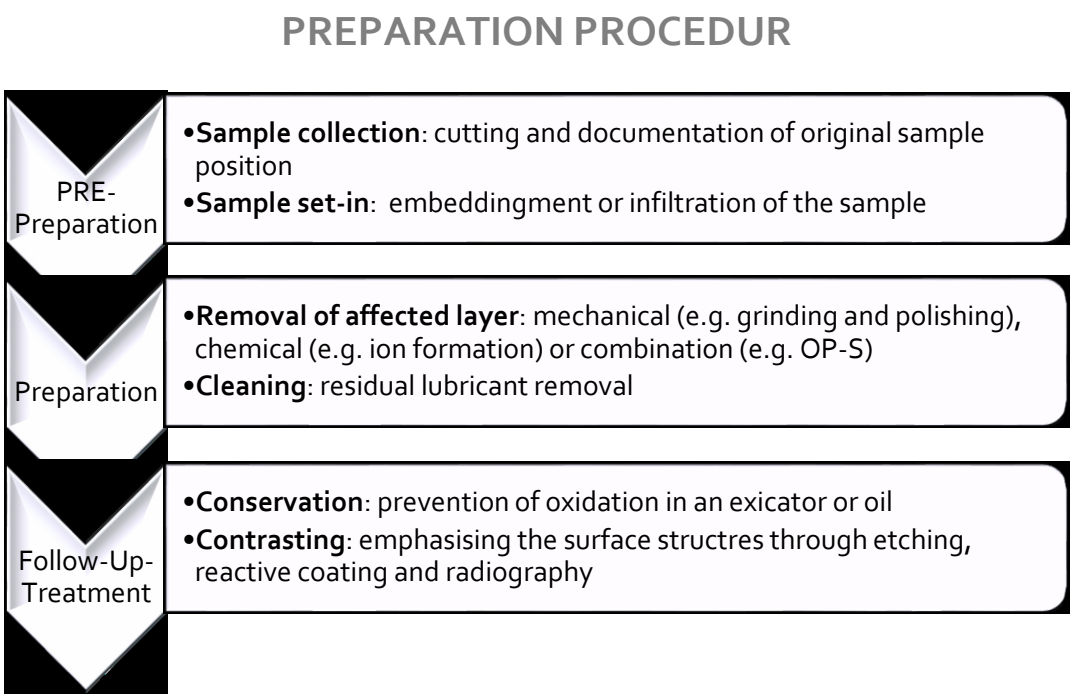

Figure 13; Processing steps of the preparation procedure. The main points Pre-preparation, Preparation and Follow-up-treatment are listed together with the steps which are included those main points.

For bulk material a roughness <0,1 µm is required to obtain a surface smooth like a mirror, which can reflect light without losses. Material deformation at the surface should never be over 1 µm, otherwise it will not be annihilated during the chemical etching process. In best case scenario deformations should be avoided completely [21]. For open-porous material the required roughness of <0,1 µm might result in the loss of the true structure, especially for material with higher porosity, due to voids between the particles. In case of pure porous copper, roughness can or rather should never be extinguished completely. A equilibrium between roughness diminishing and saving the "true" material structure has to be determined, because porosity is part of the material and posse a specific material response. Hence, five techniques along the process and their effect on the nanoindentation have been investigated, one belonging to the follow-up treatment (chemical etching), three belonging to the preparation (ion milling, OP-S and fine grinding) and one last technique belonging to pre-preparation, an alternative sample set-in (infiltration).

2.5.2. Preparation of open-porous copper surface

The later the alterations are settled in the preparation process, the higher are the probability to obtain the true material structure and less alteration of the original condition occur. Nevertheless, without levelling of the surface structure, the nanoindentation values will not sink beneath the allowed deviation maximum. Four different attempts to improve the surface roughness have been performed.

Fine grinding presents the strongest modification of the original surface. It describes the last stage of the grinding process and is normally followed by a polishing process to finish the first part of the preparation, the removal of the affected layer. **OP-S** stands for oxide particle suspension, it bases on silicon oxide and belongs to the group of chemo-mechanical polishing and finishes the step "removal of the affected layer". Those particles possess a diameter of 40 nm and create an environment with a pH value of 9,8. Only a minimal affected material layer may remain. The true material can be measured [21]. The disadvantage is, that only small samples can be prepared with the given equipment (around 7x7 mm). **Ion milling** removes the material atom by atom through argon ions, therefore very even surfaces can be accomplished. For this thesis, the material is worked from the top side to generate an even surface of the cross-section. The disadvantage is, that only a small area can be worked in a reasonable time (between 3-5 hours) and when applied on the surface it mostly possesses mentionable tilt. The residual lens is around 70 µm deeper than the primary surface. **Chemical etching** belongs to the contrasting step of the follow-up treatment. Through this method no severe changes should be made to the true material. The goal is to dissolve copper oxides. For pure copper different etching solutions are recommended for example methansulfon acid, tempered acidic acid or diluted ammonium sulphate.

2.5.3. Infiltration of open-porous copper

Infiltration is commonly used to prevent loses of porous or powdery material and deformation during the preparation and belongs to the pre-preparation stage. A common rule says, that infiltration of material is possible with a porosity of 30% and higher. This is related to the connectivity of the pore system in the material. As already given in Figure 1, it is known that, a complete connectivity can be guaranteed at 45% porosity, but from a minimum of 30% porosity the share of closed pores becomes nearly neglectable. The geometry of the pores and their connection have a high influence on the mechanism of infiltration. It determines if the material will be impregnated, infiltrated or soak completely. The difference between infiltration and impregnation for large bulk material is the depth, everything <100 µm is referred as impregnated [21]. To accomplish the infiltration of the porous copper material three different enhancements have been tested.

Ultrasonic seemed to be a possible option, because vibration during the embedding eases the escape of air reservoirs out of the pore system. Furthermore, the circulation of the agent can be enhanced, like mentioned by H.Park et.al. [14]. Additional to the movement, heat is generated and leads to slight expansions of the copper structure, which enlarges the pores and the possibility of infiltration. **Vacuum** has as a consequence that the air is sucked out of the material. Also, residuals with low vapor pressure are extracted through this method [21]. Therefore, the appearance of vacuum enhanced embedding is very clear. During curing foam can occur on the surface. **Acetone-diluted embeddingment agent** is often used for biological samples. This technique is the most time-consuming method and requires several steps. Through the acetone, the viscosity of the agent is lowered and by that the infiltration and adhesion may be enhanced as discussed in forums and required in patents e.g. [42], [43].

3. EXPERIMENT

3.1. Order of events of the thesis

Within this experiment the main goal was to receive reproducible nanoindentation values with a deviation below the required 10% deviation to count as a valid measurement. The tested material has been four open-porous copper samples with slightly different production parameters, regarding the paste material. In Table 5 all the properties as given by the company have been listed. As already mentioned the main influence on nanoindentation for pure copper are roughness and tilt.

Table 5; List of all samples measured during this thesis as given by the production company properties and appearances. The porosity has been analysed through a gravimetric measurement. Three different paste materials have been used.

Sample name	Film	Max. Thickness [µm]	Porosity distribution	Porosity (Gravimetric) [%]	Grain size distribution	Comment
J1	On Si	100	Heterogen.	~30	Heterogen.	Paste J1 on substrate
J2	Foil	30	Heterogen.	~30	Heterogen.	Paste J1 without substrate
J3	Foil	25	Homogen.	~60	Homogen.	Paste J3
J4	Foil	35	Heterogen.	~40	Heterogen.	Paste J1
J5	Foil	20	Homogen.	~20	Homogen.	Paste l J5
J6	On Si	10	Homogen.	~20	Homogen.	Paste J5 on substrate

After primary test measurements with the base material J1, which have been invalid, the **first phase** focused on preparation techniques to obtain a sufficient surface smoothness. Nanoindentation measurements after the preparation techniques of fine grinding, OP-S, ion milling and etching have been performed, to find the equilibrium between sufficient levelling of the rough surface and still preserving the original material structure. Still mainly insufficient nanoindentation values and some surprising data from the ion milling processed material made it clear that there has not been enough information regarding the material structure in the first place.

Therefore, the **second phase** of the experiment emphasised on a proper characterisation of the material structure. To stabilise the structure and for easier handling and characterisation the samples have been infiltrated. Unfortunately, a complete infiltration of the base material J1 could not be accomplished, therefore further test samples of porous copper (J2, J3, J4, J5) have been provided as foils to increase the entering surface for the resin. For the infiltration three different techniques have been investigated, ultra-sonic enhanced infiltration, vacuum enhanced infiltration and infiltration with different blends of acetone diluted embeddingment agent. The shift from surface preparation to infiltration also stabilised the

nanoindentation measurements, due to a defined Poisson's ratio and a homeostatic stress field under the indent. At least different advanced models for infiltrated samples addressing the mechanical behaviour and porosity of the material have been tried to be matched with the obtained nanoindentation values. The purpose of this was to look if a prediction model, which links porosity and mechanical properties, for further developed similar material could be found. Several models have been calculated, but no model can be recommended without reservations.

3.2. Equipment and implementation

In phase 1 the focus was set on surface preparation, while in phase 2 the attention was set on material structure characterisation and enhancement. Therefore, the surface preparation techniques, starting with the strongest surface modification and ending at the weakest surface modification, will be mentioned first. The infiltration, roughness and porosity evaluation will follow and finally the nanoindentation will be addressed. The preparation techniques have been performed on J1 and J2.

3.2.1. Fine grinding of open-porous copper

At first the samples J1 and J2 were fixed with crystal bond on separate sample holders. The fine mechanical grinding was accomplished by hand on a Struers TEGRAMIN 30. The force is applied by hand. The sand papers in use and the time during polishing are listed in Table 6. Afterwards the sample's surface has been documented and nanoindentation measurements have been accomplished on the surface.
Sample J2 was infiltrated through the crystal bond and as a result did not possess an even surface. The removal of the layer was not uniform. Therefore, the second step was skipped and the grinding time of the third step was shortened. With J1 no problem occurred, the silicon substrate beneath the coating flattened the surface and prevented the coating of infiltration.

Table 6; Listing of all grinding steps, time and sand paper of sample J1 and J2.

Sample	Sand Paper	Suspension	Time
J1	Struers 1200- SiC	Water	2 min
	Buehler CarbiMetTM 2500	Water	6 min
	Struers 4000-SiC	Water	12 min
J2	Struers 1200- SiC	Water	2 min
	Buehler CarbiMetTM 2500	Water	-
	Struers 4000-SiC	Water	5 min 25 sec

3.2.2. Oxide dispersed particle suspension OP-S of open-porous copper

For the OP-S preparation, a Struers TEGRA Force 1 grinding and polishing table was used which is equipped with a Struers TEGRA POL-11 head and sample holder. The polishing suspension is added by a TEGRA Doser-5. The force application on the Struers TEGRA system is completely computerised, thus the program was the same for all samples. Only the disc changes have to be done manually, therefore a high reproducibility is given. Every material requests a specific program sequence. The program for pure copper is listed in Table 7. The goal is just a smoothening of the surface, therefore step 1, the grinding process, was left out and just the polishing steps have been carried out for a minimal material loss. The rotation of the head and the table are concurrently (↑↑) for step 1 to 3, whereas in step 4 the head rotates contrary to the table (↑↓). Finally, the surface was documented and nanoindentation measurements have been done.

If the assembling of the sample holder is not done with care, the seating of the sample surface can be askew and a tilt will be remaining on the polished sample, which again affects the nanoindentation. The sample size is limited through the carrier size to a diameter of 7 mm.

Table 7; Listing of the polishing program for pure copper. For every step a specified disc, suspension, force, duration time and velocity is necessary. Even the rotation relation between the head and table is defined.

STEPS	Disc	Suspension	Time	Force	Velocity	Rotation
1	MD-Largo	DiaPro All/Largo	4 min	15 N	Head 150/ Table 150	↑↑
2	MD-Dac	DiaPro Dac (3 µm)	5 min	10 N	Head 150/ Table 150	↑↑
3	MD-Nap	DiaPro Nap-R (1 µm)	3 min	10 N	Head 150/ Table 150	↑↑
4	MD-Chem	OP-S (0.04 µm)	3 min	10 N	Head 150/ Table 150	↑↓

3.2.3. Ion Milling of open-porous copper

Ion milling or ion slicing has been used for the infiltrated samples and sample J1. For the ion milling a Hitachi IM 4000+ was used. It is a combined cross-section and flat surface ion milling system and operates with an argon ion gun running with a standard voltage of 6 kV. The ion milling has been done on the cross-section of the samples, it might also be possible to perform the ion etching on the surface, but the residual etching lens would be concave. Through the attachment of a mask, a clear edge and a flat surface in the middle of the etching lens can be provided if the ion milling is performed on the cross-section. The sample is attached with conductive silver to the mask and the removable sample holder. For the nanoindentation the residual lens should be broad or shallow, otherwise the indenter tip may mount on the edges without contacting the surface.

Nevertheless, the disadvantages are obviously the preparation and preparation time. It depends on the dimension of the prepared area, the thickness of the sample and the material of the sample. For example, if a given 400 µm thick silicon wafer need to be sliced, a 10-50 µm deep slice requires 30 minutes. Everything over 100 µm needs 2 hours. A maximum of 200 µm thickness can be milled from one side. If the whole wafer cross-section should be sliced, the sample has to be turned around.

3.2.4. Etching of open-porous copper

The goal for the etching process was to remove oxides from the surface. For this, two solutions are recommended. Firstly acidic acid (98-100%) at 40°C and secondly a methansulfon acid. At elevated temperatures, the oxidation of copper occurs immediately. Therefore, the samples have been pasted to the sample holder before etching, otherwise the sample would have oxidised when placed on the liquid crystal bond. The crystal bond is dissolved through either acidic acid or metansulfon acid, as a consequence the etching solution was applied through soft rubbing of a soaked cotton swap. The connection between sample and sample holder could not be guaranteed for J2.

3.2.5. Infiltration of open-porous copper layers

With infiltration, the durability of the sample is increased and the uncertainty of the Poisson's ration of air in foams is avoided. As embedding agent EpoFIX™ cold-setting embedding resin was used. It consists out of a resin and a hardener. After mixing the resin with the hardener the substance starts to harden after 30 min, while a complete curing is accomplished after 8 h. It was chosen because it is built out of bisphenol-A-diglycidylether and together with the triethylenetetramine the hardener fabricates bisphenol-A-epoxy. The compound is preferred because of its high strength (75 Shore D) and due to insignificant shrinkage as well as viscosity (0,55 kg/ms) it is suitable for fibre infiltration. Adhesion and viscosity are depending on the infiltrated material, therefore different materials require further adjustments to infiltrate the material properly [41–43]. For this research, the basic EpoFiX™ was used owing to its reachability. Through investigation three techniques seem reasonable. The use of ultrasonic enhanced infiltration, followed by an acetone diluted embeddingment agent and finally vacuum enhanced infiltration. Every sample had been cleaned with acetone and isopropanol each for 5 min. in the ELMA Ultrasonic bath. Exceptions have been J3 and J5, because they didn't sustain the ultrasonic bath for even 1 min. As a consequence, these two samples have only been bathed in acetone and isopropanol for 10 min. After desiccating the samples, they have been put upright into the mould and held in that position by a clamp. Then the different procedures of infiltration with the embedding agent have been accomplished.

For **vacuum enhanced infiltration** an aspirator was used. Directly after combining the resin and the hardener the mixture was poured into the mould and put inside a bell jar, which was set under vacuum with the aspirator. After 60 min the aspirator was turned off and the mould rested for 10 h to cure completely.

With the **ultrasonic enhanced infiltration**, an ELMA ultrasonic bath with integrated temperature and time regulation was used. When the resin was mixed, and poured into the mould, it was immediately put inside the ultrasonic bath. Increasing temperature of the bath during running time due to the vibration led to a prolonged pot time. Therefore, the resting time in the ultrasonic bath had been 90 min.

The **acetone dilution** lowers the viscosity of the resin and increase the curing time. It is commonly used for biological samples like wool. The basic idea to this technique is to lower the surface tension and curing time of the embedding agent, so that smallest pores can be infiltrated before the curing starts. Nevertheless, the curing time of the diluted embeddingment agent is not bearable. Therefore, three different blends of acetone diluted agent have been prepared, each blend consist of a different ratio of acetone to epoxy resin (1:1, 1:3 and 0:1). For one sample three stages as listed in Table 8 have to be accomplished. At first every sample rests in blend 1 (1:1). After two hours the sample is lifted immediately from blend 1 (1:1) into blend 2(1:3) and again two hours later in blend 3 (0:1). The last blend is pure EpoFIX™ with a curing time of ten hours. But the curing time at the last stage has been extended, because procrastinated acetone from the former stage might have prolonged the curing time.

Table 8; Listing of all the stages the infiltration process "Acetone diluted embeddingment agent" needs and their resting time. Every blend consists of a different ratio acetone to epoxy resin. Through the processing the possibility of procrastinated acetone is given.

	Blend	acetone/epoxy resin	Time
Stage 1	1	1:1	2 h
Stage 2	2	1:3	2 h
Stage 3	3	0:1	12 h

3.2.6. Roughness measurement of an open-porous copper surface

To estimate the surface properties an area roughness analysis has been done for all samples (J1, J2, J3, J4, J5, J6) on their top side. Due to the production process, all foils possess a flatter and a rougher side. The foils have been stripped from the substrate. The substrate side (down side) therefore is flatter than the top side. A roughness measurement is a quick way to obtain information about the sample structure and functionality. An additional advantage is that the roughness analysis the samples do not need any treatment or preparation of the surface.

The measurements have been performed with a LEXT 3D Measuring Laser microscope OLS4100 (referred as LEXT). Through this, a non-contact 3D scanning roughness measurement of a surface can be completed fast and at a high-resolution at 10 nm in z-axis and at 100 nm in plane. For the laser microscope, the OLS4100 uses a 405 nm semiconductor laser as light source and a photomultiplier as a detector. The total magnification range from 108x – 17,280x, while the optical magnification is settled at 1x - 8x. The height measurement system is a revolving nosepiece vertical-drive system with a scale resolution of 0.8 nm and a movement resolution of 10 nm. The accuracy is a maximum of 0.2 measuring length per 100µm or less. For the coloured images a white LED is used as a light source and the detector is an 1/1.8-Inch 2-Megapixel Single-Panel CCD with a digital zoom of 1x- 8x. The objectives 5x and 10x are BF Plan Semi-apochromat, whereas the 20x, 50x and 100x are special LEXT-Dedicated Plan Apochromat objectives [47] To guarantee statistical reasonable values, every sample was analysed at three self-constrained areas and an average was calculated. Therefore, they are given with the significance of 3 to 4 digits, but only 2 are reasonable. Next to the roughness parameter output, high contrast and intensity laser scanning images of the surface have been taken and an Abbot-curve was attached to the report.

3.2.7. 2D Porosity analysis of open-porous copper layers

The porosity has been analysed along the cross-section of the samples. The material went through an infiltration and a cutting process with a final surface preparation step through ion slicing, so to grant an accurate measuring of the porous material. The measurement has been made with an OLYPMUS BX51 light microscope (referred as LIMI). It is equipped with a MÄRZHÄUSER WETZLAR TANGO Desktop and an ERGODrive System for accurate table movement and exact measurement as well as documentation along x-, y- and z-axis. The software used for the analysis of the pores is OLYPMUS Motion Stream and possess an integrated tool for calculating the porosity by defining a two-dimensional region of interest (ROI). The software analyses the percentage of the surface which is settled around a specific intensity range, defined as pores. The threshold for this specific intensity range could be selected manually or by the program itself. The different stages of the process are mentioned in Figure 14 [48]. To start with the measurement a sharp image of the material structure is needed. In case of the open-porous copper samples a 100x magnification was necessary to see the fine structure at least. Due to the high magnification and the residual lens geometry of the ion milling, the image was generated through z-stacks. Otherwise it would have not been possible to create a sharp image. The porosity analysis was done on coloured bright field images and binary converted images. Mostly such porosity analysis programs operate with greyscale images due to better resolutions, but with the OLYMPUS Motion Stream software, the measurement on a coloured image was less error-prone.

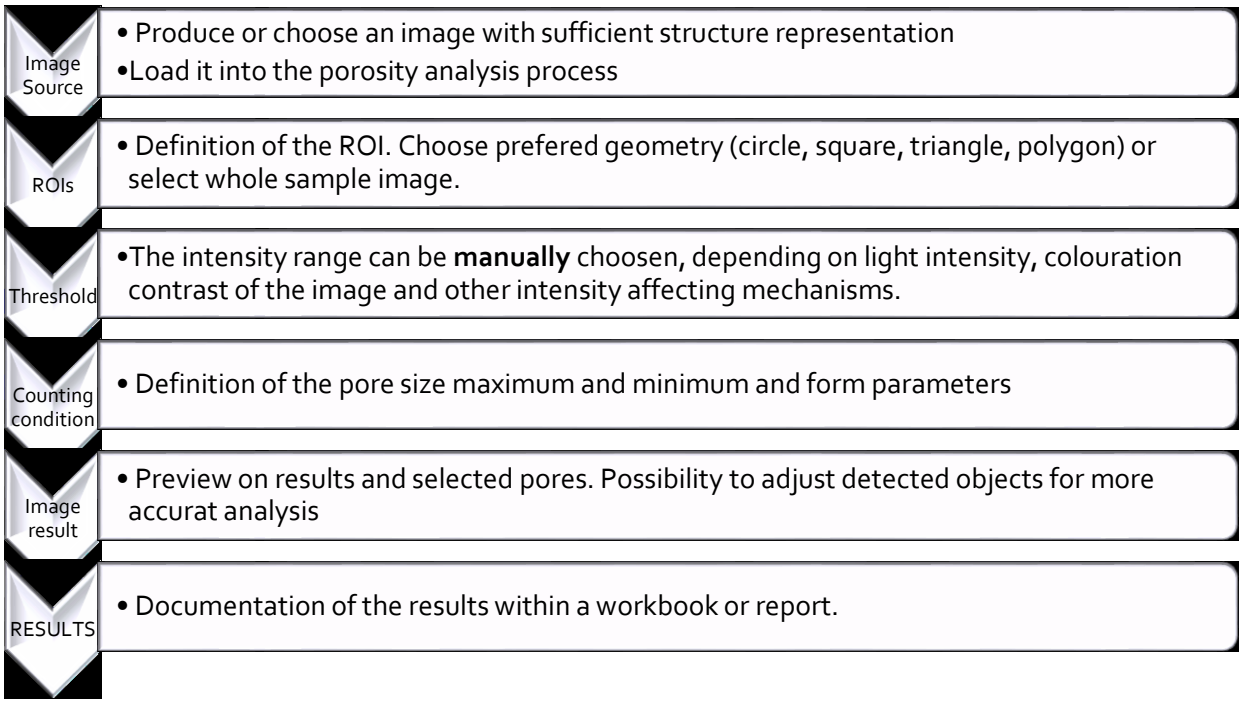

Figure 14; The six stages to obtain a porosity value with the Olympus STREAM Software

For the coloured image only the threshold has to be chosen manually for step 3. For all the images, it was set to a minimum of 150 and the upper limit was set to maximum. The manual threshold setting causes a certain error in the analysis. To generate the binary picture at step 1 the coloured image is converted into a greyscale image, so it is equal to an intensity picture. In step 2 the greyscale images are converted into a binary image. For step 3 morphological filters, like erosion and dilation, have been applied to extinguish noise and to smoothen the pore shapes. For a binary image, one has to choose the possible threshold 3 times and it also can be altered. The creation of a binary image with the OLYMPUS Motion Stream software is highly depending on human arbitrary. This also reflects in the partly unrealistic values. Due to the fact that most samples did not possess a flat top surface, the definition of the ROI was made through Polygon shaping. As a result, a maximum area could be defined and the porosity analysis gave a reasonable mean value. This was repeated at different contained areas along the sample. The porosity measurements for one kind of source image (colour or binary) have been performed by one person at one day, one sample after another to minimise human error. The values of the analysis are listed in Table 9.

Table 9; List of porosity values determined through 2D analysis with the software OLYMPUS Motion Stream on the colour and binary (black and white) image

Porosity [%]		J2	J3	J4	J5
	2D: colour image	36	55.4	43.1	36.7
	2D: binary image	38.6	44.1	55.1	49.7

3.2.8. Nanoindentation of open-porous copper layers

The aim of the nanoindentation is to determine Hardness and the Young's modulus of thin or microscopic particles. The nanoindentation was accomplished by the KEYSIGHT NanoIndenter G200. The indentation was done by a Berkovic tip at room temperature (RT). The temperature is not regulated, when operated at RT. Therefore, to minimise the temperature drift, the hub of the machine should never be opened for a long period, ideal would be a samples handling only through the small door integrated at the KEYSIGHT NanoIndenter G200 hub. If all this is considered, then the temperature inside the machine is stable around 27 °C. The software used for the analysis of the nanoindentation results within this thesis is called NanoSuite. The Berkovich indenter tip in use, was not a perfect tip. Therefore, the area function of the used tip was always defined through a pre-indentation on fused quartz, with the standard values of E = 68.8 ± 0.2 GPa and H = 9.54 ± 0.04 GPa [49]. NanoSuite implements this value automatically in its area function. Because all nanoindentation measurements have been done at different day, different area functions have been used. The indentation process was depth-controlled and regulated by a maximum strain rate of 0.05 nm/s. Strain rates between 0.05 and 0.2 nm/s are common [31]. For the measurement, the CSM-method was used. A frequency target of 45 was used. The advantage of CSM is that an exact contact stiffness is known for every indentation depth. All the samples for the pre-test and phase 1 have been taped on a simple sample holder by crystal bond. The sample holder was made out of aluminium or brass. The sample holder used for the phase 2 nanoindentation measurement was a clamping holder out of brass (Figure 15), where the samples are inserted with the ion milled lens upside and fixated through adjustment screws. The milling lens surface has to be placed slightly higher than the clamp surface, otherwise the indenter tip might get in contact with the edges.

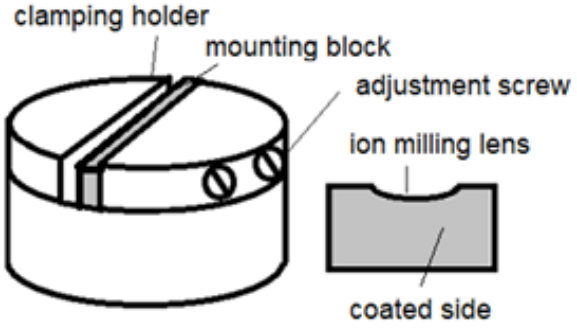

Figure 15, Clamping holder for phase 2 nanoindentation measurements. The infiltrated and ion milled cross-section is on top. The sample itself is fixated through adjustment screws and a mounting block.

Different indenter depths, surface preparation techniques and infiltration techniques had been tested, until the ideal setting was found (infiltrated through vacuum enhancement) and the main measurements with samples of different production parameters have been tested.

An overview from all measurements and the used parameters is given in Table 10.

Table 10; Summary of all nanoindentation measurements, which have been performed during this thesis

	Nanoindentation Test		Sample	Depth [nm]	Number of Indents
	PRE-Test (Depth sensibility)		J1	**2500**	9
			J1	**5000**	9
			J1	**10 000**	9
Phase 1 Surface Preparation Techniques	**Etching (Top side)**		J1	1000	6
			J2	1000	6
	Etching 180° (bottom side)		J2	1000	9
	Fine mechanical treatment		J1	1000	6
			J2	1000	6
	OP-S		J1	1000	9
			J2	1000	6
	Ion milling		J1	1000	10
Phase 2 Infiltration	**Infiltration Method**	**Vacuum**	**J1**	1000	10
		Vacuum	**J2**	1000	6
		Acetone	J2	1000	6
	Main Measurements Different processing parameters		**J2**	1000	6
			J3	1000	10
			J4	1000	10
			J5	1000	10
	Additional Tests		J5 SK	1000	9
			J6	1000	9

With the CSM-method it is possible to do the analysis for only one point, but the advantage of CSM is to do the analysis for a wider range of indentation depths. The values need to be stable to provide a useful statistical treatment, for the measurement analyses. Therefore, the selection of the range is important to the results. During the pre-tests following analysis ranges have been chosen: [1900 to 2400 nm] for the 2500 nm indentation, [4000 to 4900 nm] for the 5000 nm indentation and [4500 to 6000 nm] for the 10,000 nm indentation. All nanoindentation analyses for measurements up to 1000 nm indentation depth have been done for the range of 800 to 1000 nm.

4. RESULTS

The pre-tests and phase 1 are mainly focusing on J1 and have been developed further on from this specimen until in phase 2 the infiltration made it necessary to switch from layers on silicon to foil. Phase 2 also included the main measurements for this thesis. Consequently, for a better understanding first all results for J1 are given and afterwards the infiltrated foil samples with the different production parameters.

4.1. Phase 1- Pre-tests and surface preparation technique

The base material J1 was delivered on silicon and appears as a salmon coloured dull film. About the history of the materials only a few things are known. The material is a porous copper coating and has been applied to the substrate with stencil printing technique and then have been cured at 400°C.

4.1.1. Surface microstructure of J1

The coating material is extremely heterogenic and consist out of bright globular spots, elongated cracks and areas in between. In Figure 16 the images from the laser microscopy are given. In Figure 16 a), the coloured image shows brighter globular spots and elongated cracks which are against what was expected from the sintered porous material. The coppery areas in between seem to be fine structured. Especially in Figure 16 b) this can be seen clearer, due to the intensity images of the laser microscopy, where the areas are speckled with what seems to be small dimples.

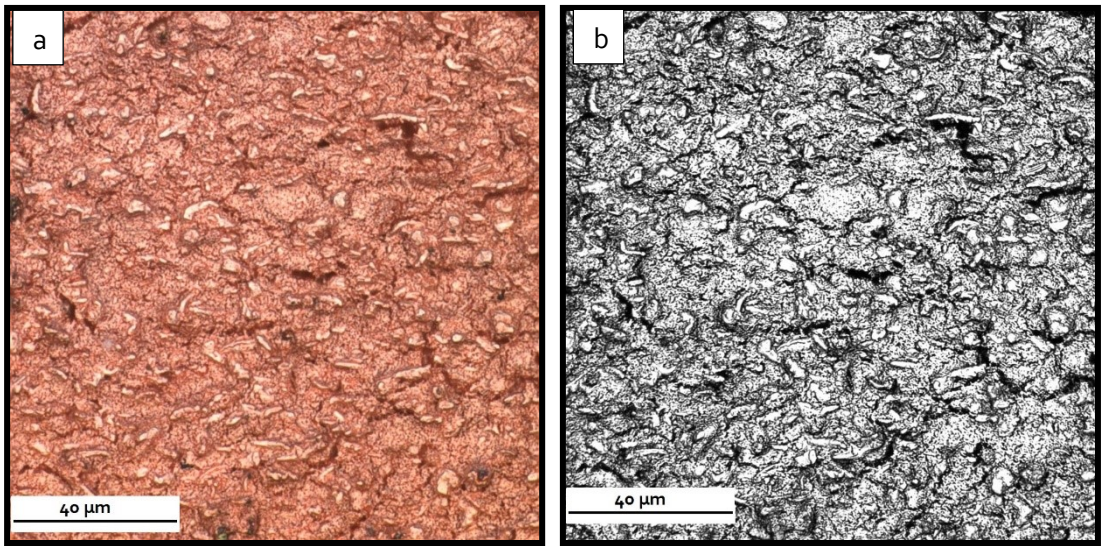

Figure 16; Surface image of J1 using the LEXT 3D laser microscop.In a) the coloured image can be seen and b) highly contrasted intensity image shows the same area.

4.1.2. Roughness profile of J1

A topological image obtained with the LEXT 3D Laser microscope gives a better understanding of the surface height. Figure 17 illustrate two different exemplary areas of J1. The surface consists on one hand of areas with wide peak-to-peak distance and height difference, on the other hand of areas with mostly the same height and small sinks. The scale went from the lowest point (violet) to the highest point (red) of the surface. The exact range of the height and the additional numbers are given by Sz in Table 11.

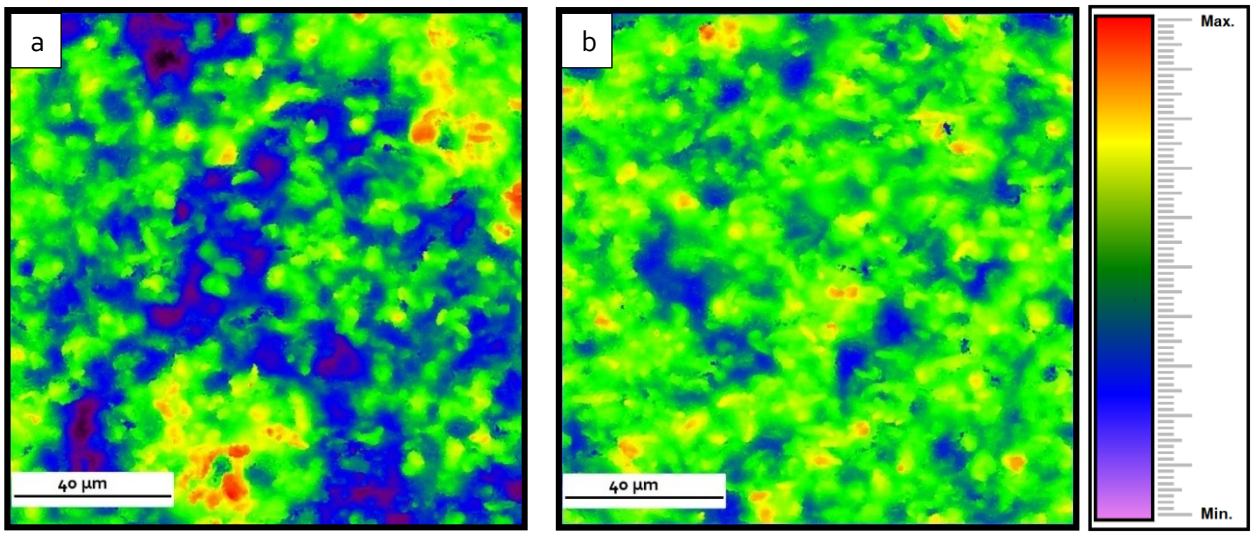

Figure 17; Topological image of the J1 surface using the LEXT 3D laser microscope. The surface consists out of wide dales and great height differences. Combined with the Roughness parameters from Table 1 it can be determined, that the maximum height is 8 µm.

The Table 2 mention the amplitude parameters for surface roughness (arithmetic mean height (Sa), skewness (Ssk), maximum pit height (Sv), maximum height (Sz), Kurtosis (Sku), root mean square height (Sq) and maximum peak height (Sp)). The Sz, gives the total range of height. It is 7.9±0.6 µm. The average line is at 3.3 µm (Average line = Sz – Sp).

Table 11; Roughness parameters of J1

J1	Sq [µm]	Ssk [µm]	Sku [µm]	Sp [µm]	Sv [µm]	Sz [µm]	Sa [µm]
Mean	1.072	0.287	2.936	4.551	3.370	7.921	0.858
б	0.062	0.139	0.092	0.348	0.206	0.554	0.045

Additional to these values the functional parameters of the surface have been analysed and graphically represented through an Abbott-curve, which is illustrated in Figure 18. The x-axis is listing the areal material ratio in percent and the y-axis the height in µm. From the Abbott-curve the core roughness depth (Sk) of 3.05 µm and a reduced peak height (Spk) of 2.40 µm with a reduced dale height (Svk) of 1.21 µm have been measured. From the curve it can be concluded, that no sharp tips or steep craters occur and the material ratio above and below the average line are alike.

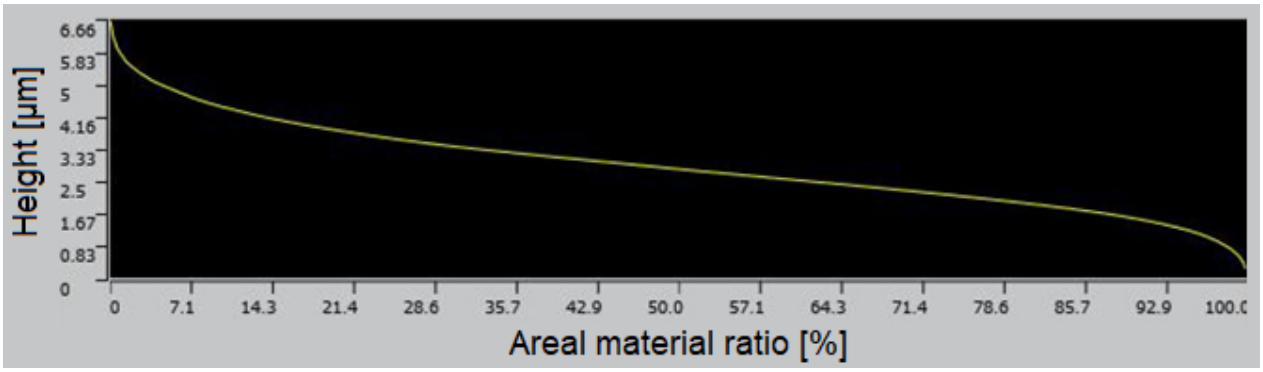

Figure 18; Abbott-curve of J1. Listing the areal material ratio (x-Axis) against the height of the surface (y-Axis).

4.1.3. Microstructure cross-section of J1

When the cross-section of the material was observed for the first time the composition of different areas could be explained. In Figure 19 a cross-section is illustrated, at the bottom of the image is the silicon wafer. On top of the substrate is the open-porous copper coating, consisting of three different structures. First, bright mainly round shaped areas (red boxes), further darker bluish structured areas and finally elongated dark pores. Those bright particles possess a dimension of around 5-15 µm. The pore systems have been measured and reach a maximum size of 95 µm at some places and seems to cross through the whole sample. As a consequence, the material might be open-porous. Furthermore, the surface roughness can be observed, due to the waviness of the top layer of about 5 µm height difference.

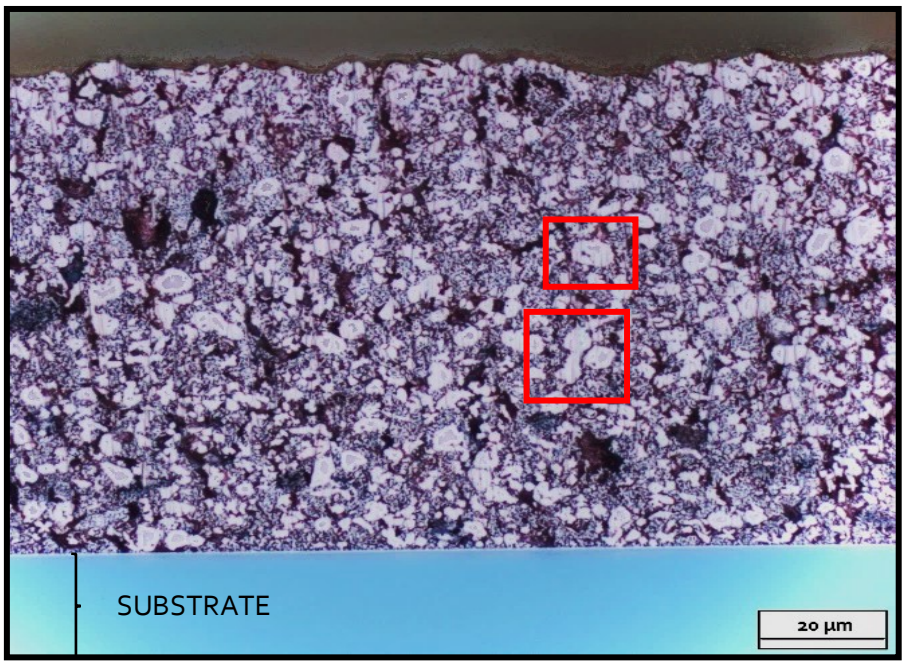

Figure 19; The cross-section image of J1 generated through light microscope (LIMI). At the bottom the substrate can be seen. On top of the substrate is the coating. Bright particles with a mainly round shape and bluish highly structured areas are composing the coating. The elongated pores can be seen as black voids with dimensions up to 95 µm.

At first, the dark blueish fine structured areas have been mistaken for dirt, but after a very clean processing and the fact that those structures occurred at every cross-section, the thought occurred that maybe merely the magnification of the light microscope was not high enough to give a proper declaration. Therefore, additional SEM has been performed. In Figure 20 a) a cross-section of the material (J1) can be seen. The cross-section consists out of particles with dimensions from a few hundred nanometres up to a few micrometres, surrounded by rougher and finer pore systems. The term particle is chosen because as can be seen, the particles are made up of different areas, which are grains. In b) a fine structured surface area is further magnified. A sponge-like open-porous structure can be seen with nanoscale particles. The sponge structure leads to a highly connected fine pore system.

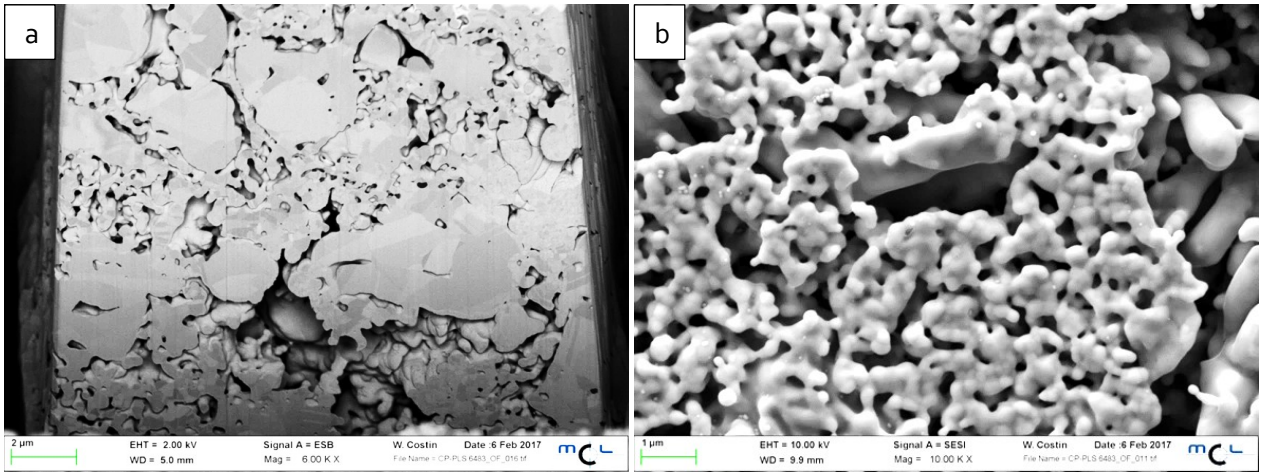

Figure 20; Microstructure of J1 recorded through SEM/FIB Tomography give a sufficient conclusion of the material. A) The bigger round particles consist out of different grains. The same is legit for the smaller particles. In b) those smaller particles have been magnified further. Here can be seen, that the bluish fine structures areas are nanoscales particles organised in a sponge-like structure. The sponge-like structure leads to a highly connected pore system with small pores as can be seen in b) and huge pores like at the bottom of a).

Those images have been taken from the associated work of A. Wijaya [23], where further information can be looked up. But it was necessary to include them in this work to explain the composition of the fine structure seen in the previous images and the nanoindentation behaviour completely.

4.1.4. Surface Preparation of J1 and J2

Surface preparations in Phase 1 have been performed on the samples J1 and J2. First the sample J1 will be explained, then the problems with J2 will be discussed.

In Figure 21 the different surfaces of J1 after the preparation techniques are shown. Listed under a) is the etched surface. The roughness tips are shining very bright, while the bottom of the surface seems to be dark. This is identical for all regions of the sample. In Figure 21. b). scratches from the preparation can still be seen. Although the original material structure can't be seen, little spots are still visible on the worked

surface. These dark spots might be pores of the original material. The next image c) illustrates the surface worked via OP-S. The structure consisting out of a similar structure as seen in the cross-section in Figure 19. The only difference is that the elongated pores are smaller. The roughness of the original surface was diminished. At least the surface worked with ion milling is shown under d). The picture is already known from the cross-section in Figure 19, because they have been preparated through ion milling.

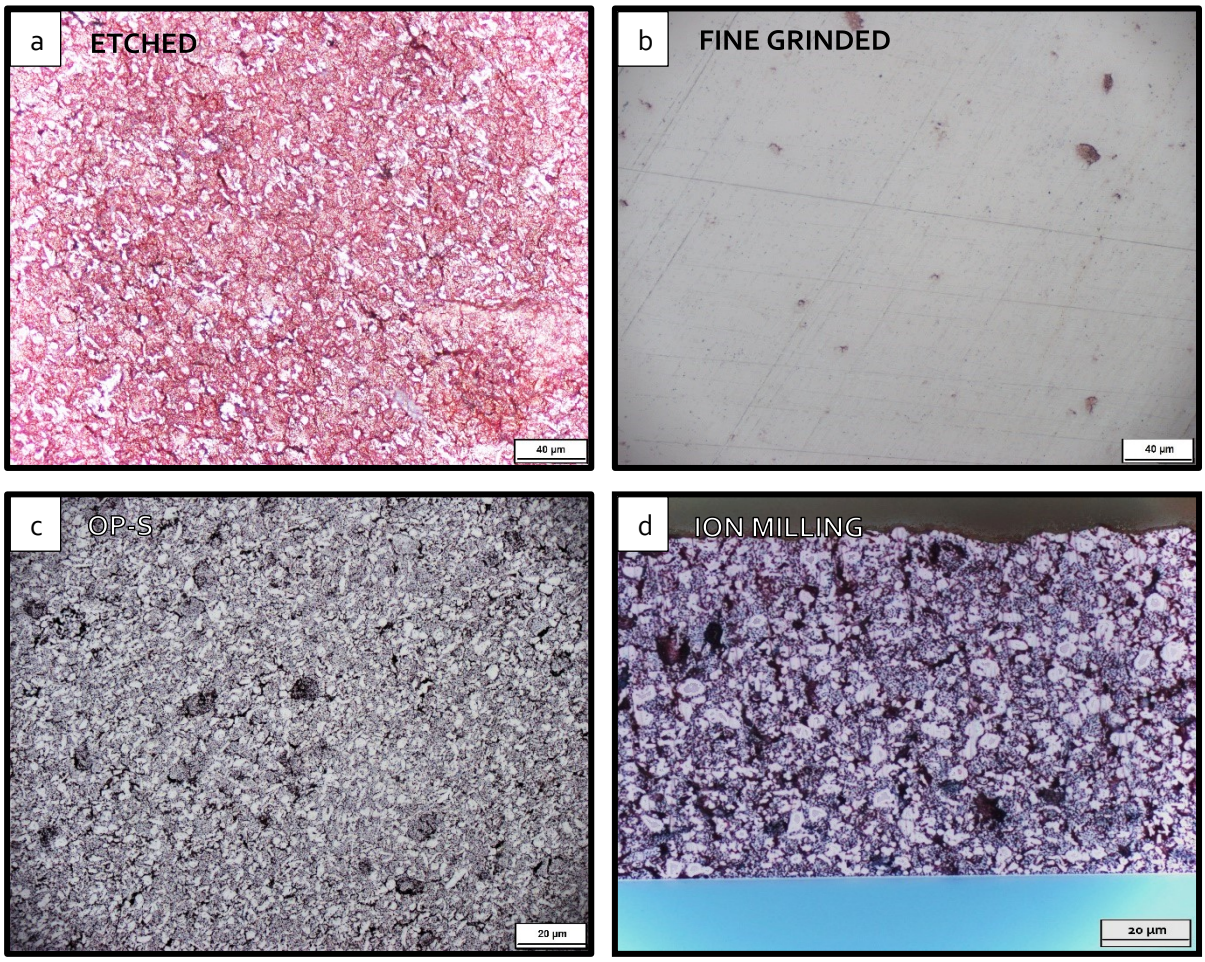

Figure 21; Different surfaces after preparation documented by using a LIMI. a) ***etched*** *b)* ***fine grinded*** *c)* ***OP-S*** *d)* ***ion milled****. At c) and d) the familiar structure can be observed, while in b) no structure at all can be observed. In a) the etched surface might be slightly polished by the cotton swap or the acid has been more aggressive on the tips. Therefore, the peaks appear more shine than the lower surface.*

The preparation techniques (fine mechanical treatment, OP-S and etching on both sides) have also been performed on J2. Difficulties with the preparation process of the foils, due to uneven positioning as a result of involuntary soaking with the crystal bond, led to poor performances in comparison to J1. Therefore, material loss was high and no sufficient surface smoothness could be accomplished. In Figure 22, the problems with J2 and different preparation techniques are illustrated. In Figure 22 a) and b) etching was performed. The material got soaked by crystal bond, but the methansulfon solution dissolves

crystal bond. The crystal bond looks like water over the material (Figure 22 a). Figure 22 b) on the right side illustrated the still infiltrated material, while on the left side etching dissolved the crystal bond. Figure 22 c) illustrates the OP-S worked surface and d) the fine grinded surface, in both cases still unworked material surface can be seen. This is related to the waviness of the material. As a consequence, the preparation process could not have been performed until a sufficient smooth surface could be reached, because a minimum thickness is required for indentation.

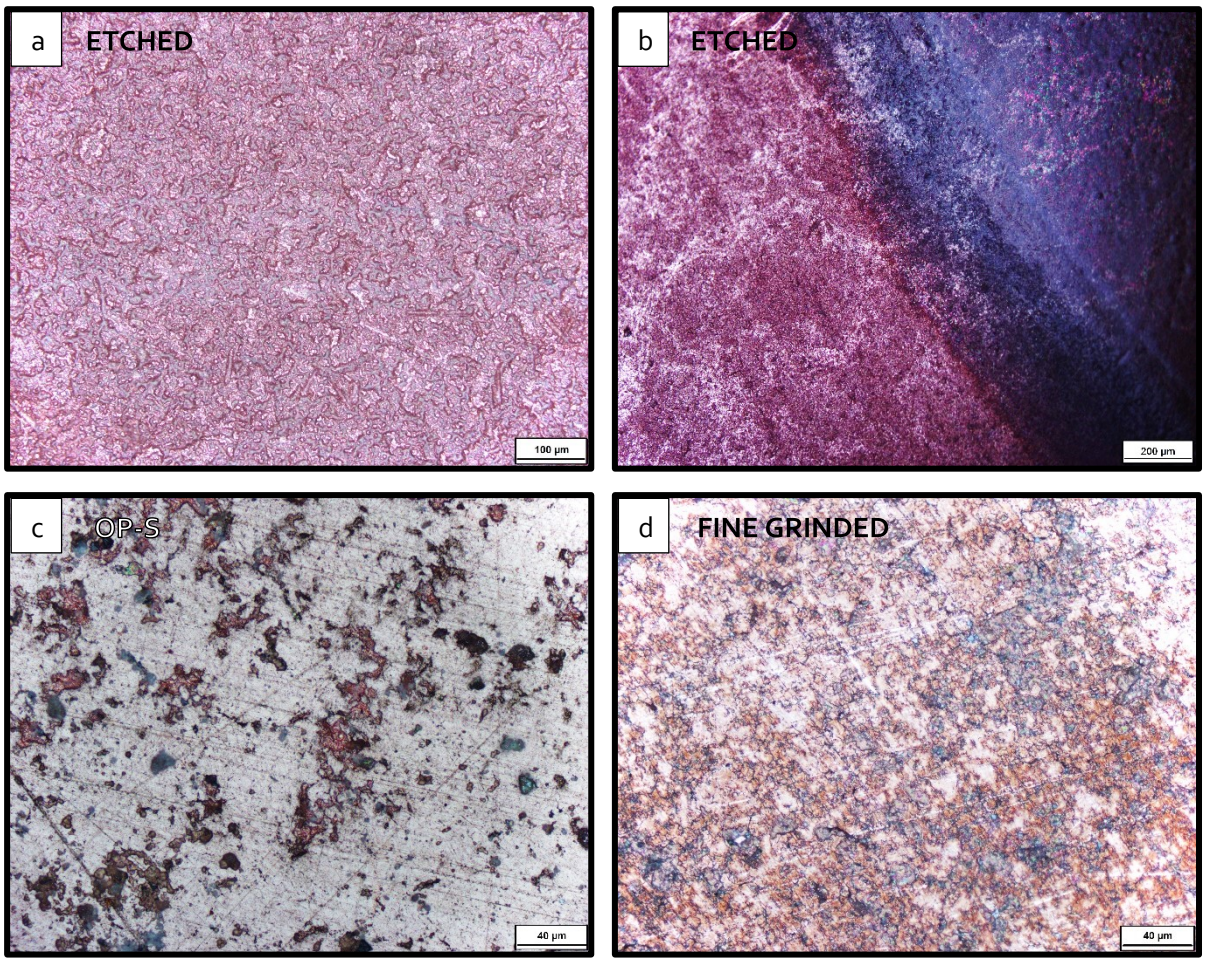

Figure 22; Different surfaces after preparation documented using a LIMI. A) ***etched*** *b)* ***border line between etched and soaked material*** *c)* ***OP-S*** *d)* ***fine grinded****. In a) the shine appearance of the crystal bond can be guessed. At a lower magnification, the border between the etched and non-etched can be seen clearly. Waviness, due to the partly infiltration by the crystal bond, aggravate the polishing and grinding process.*

4.1.5. Nanoindentation of the Pre-test and Phase 1

(1) PRE-TEST (Depth): The ideal depth has to be settled between a from roughness uninfluenced depth, as recommended by M. Laurent-Brocq et. al [8] and the 10 % rule, which insists that the indentation depth should never exceed more than 10% of the total thickness of the layer, otherwise the substrate will affect the measurement [50]. In the following Figure 23 the load-displacement, Modulus and Hardness curve

over indentation depth are illustrated. Through the CSM a continuous function of the mechanical behaviour can be observed [31]. This gives the opportunity to determine the depth when the modulus and Hardness values stabilise. The measurement is depth-controlled, means all indents to a predefined depth. Therefore, the load maxima deviate, resulting in different levels of load-plateaus, this can be seen in Figure 23 a) The spread of the plateaus and the scattering of the different measurements can be seen in relation to the total value, this indicates a high deviation value. In Figure 23.b) the influence of the surface roughness is shown. The broad scattering is identical with findings in published papers [10], [11], [51]. The deviation behaviour along the displacement seems to be similar for all indents, regardless if the indentation is deeper than the others. Figure 23 c) illustrates the Young`s modulus and d) Hardness as a function of the indentation depth. The scattering at the beginning of the Young`s modulus as well as the Hardness, is related to the roughness of the sample similar to the behaviour shown by Laurent-Brocq et al. *[8]*. But both functions run into a divers plateau at around 4500 nm.

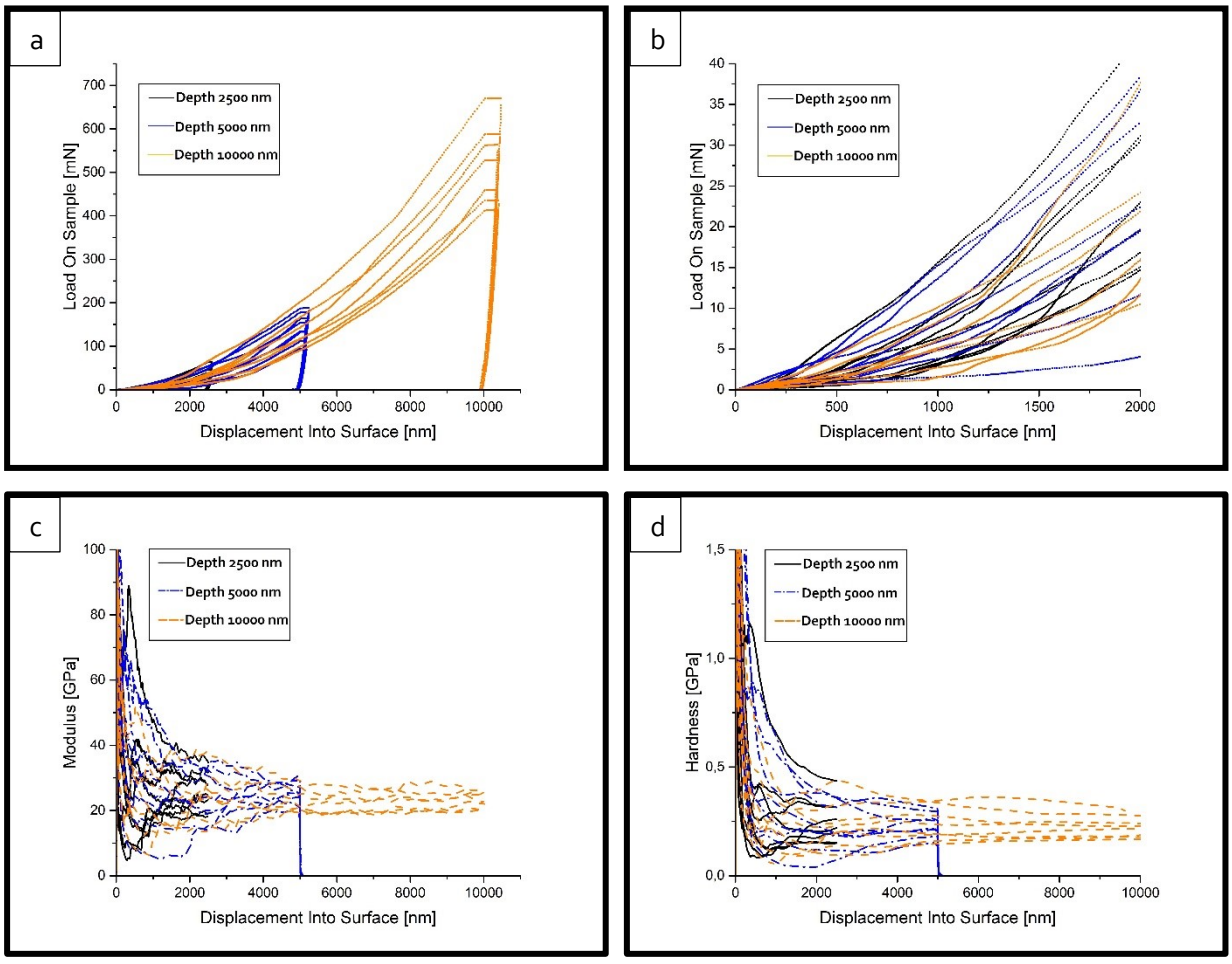

Figure 23; The load-displacement curve for J1. In a) all indentations are shown over their entire indenter depth. The deviation of the values is similar b) is focused on the start, where a broad scattering occurs. c) illustrates the modulus curve over indentation depth, while d) shows the Hardness curve. The broad scattering at the beginning is highly influenced through roughness. A plateau can be seen at around an indentation depth of4500 nm.

In Table 12 the different E^* and H values and deviations along the indenter depth are listed. The deviation of the Hardness is nearly twice as high as the one of the Young's modulus. This confirms the conclusion of M. Laurent-Brocq [8], that the Hardness is more affected by roughness, than the Young's modulus.

Table 12; Young's modulus and Hardness values from the Pre-Tests, together with deviation distribution over displacement. After 5000 nm the values seem to be stable. The Hardness deviation values are twice as high, as the Young's modulus deviation values.

	2500 nm		**5000 nm**		**10 000 nm**	
	Red. Modulus	Hardness	Red. Modulus	Hardness	Red. Modulus	Hardness
	GPa	GPa	GPa	GPa	GPa	GPa
Mean	**26.3**	**0.25**	**25.2**	**0.23**	**22.83**	**0.22**
Std. Dev.	*6.3*	*0.1*	3.4	0.06	3.34	0.06
% COV	**23.84**	**41.19**	**13.51**	**27.44**	**14.62**	**27.49**

(2) PHASE 1 (Surface preparation): The surface preparations alternated the roughness of the top layer. As a consequence, it might not be the true material. The indentation depth has been the same for all the measurements. In Table 13 lists the measured nanoindentation values for all performed surface preparation techniques on J1. The values deviate from high values with little deviation e.g. fine mechanical treatment $E^* = 56.6 \pm 1.5$ *GPa* to low values with high deviation e.g. ion milling $E^* = 21.5 \pm 30.38$ *GPa*. These values in combination with the surface images in Figure 21 give the assumption, that for the fine mechanical treatment results in a severe material structure loss, while the ion milled surface became even rougher, due to access to the inner pore system. The OP-S values are similar to the pre-test values and the deviation for the Youngs's modulus is sufficient, whereas the Hardness deviation is still too high. Why the values after etching deviate so extreme from the pre-test values, could not be explained.

Table 13; Measured nanoindentation values of the reduced Young's modulus (E^*), Young's modulus (E) and Hardness (H) from Phase 1. Different surface preparation techniques on J1 (etching, fine grinding, OP-S and Ion milling)

		Red. Modulus	Modulus	Hardness	Drift Corr.	Temperature
		GPa	**GPa**	**GPa**	**nm/s**	**°C**
Etching	*Mean*	**41.3**	**38.5**	**0.42**	0.064	26.1
	Std. Dev.	4.9	4.7	0.1	0.02	
	% COV	**11.81**	**12.28**	**23.29**	31.25	
Fine mechani	*Mean*	**56.6**	**53.5**	**1.27**	0.12	25.5
	Std. Dev.	1.5	1.5	0.05	0.012	
	% COV	**2.6**	**2.73**	**4**	10.28	
OP-S	*Mean*	**30.9**	**28.5**	**0.41**	0.077	25.8
	Std. Dev.	2.5	2.4	0.06	0.011	
	% COV	**8.18**	**8.41**	**15.89**	14.61	
Ion Milling	*Mean*	**21.5**	**19.7**	**0.28**	-0.022	27.1
	Std. Dev.	6.5	6.1	0.1	0.015	
	% COV	**30.38**	**30.92**	**34.44**	-69.36	

In Table 14 the values of the nanoindentation measurements of all performed surface preparation techniques on J2 are listed. Due to the production process, the foil consisted out of a rough top side and a flat bottom side. The etching has been performed on both sides, the etching on the bottom side is referred as "Etching 180°". Here the values for OP-S and both etching processes seem reasonable, but cannot be trusted, due to the infiltration with crystal bond.

Table 14; Measured nanoindentation values of the reduced Young's modulus (E), Young's modulus (E) and Hardness (H) from Phase 1. Different surface preparation techniques on J2 (etching, fine grinding and OP-S).*

		Red. Modulus	Modulus	Hardness	Drift Correction	Temperature
		GPa	**GPa**	**GPa**	**nm/s**	**°C**
OP-S	*Mean*	**32.3**	**29.8**	**0.71**	-0.151	26
	Std. Dev.	1.4	1.3	0.1	0.038	
	% COV	**4.36**	**4.49**	**13.79**	-25.2	
Fine grinding	*Mean*	**29.4**	**27.1**	**0.81**	-0.164	25.7
	Std. Dev.	0.6	0.6	0.1	0.029	
	% COV	**1.98**	**2.03**	**12.95**	-17.74	
Etching	*Mean*	**24**	**22**	**0.43**	-0.787	26.3
	Std. Dev.	3.2	3	0.09	0.178	
	% COV	**13.19**	**13.46**	**21.7**	-22.67	
Etching 180°	*Mean*	**26.8**	**24.6**	**0.43**	-0.321	26.2
	Std. Dev.	2.7	2.5	0.1	0.079	
	% COV	**10.1**	**10.33**	**22.13**	-24.59	

Different techniques have been used to alternate the surface roughness of the samples J1 and J2, but due to the application problems of J2, as a result of infiltration with the crystal bond, a closer look has been taken only on the surface preparation of J1. Here, the preparation technique of fine grinding possessed the most problems. Through this method significant layer reduction and deformation occurred, which leads to problems with thin layers and material structure alteration. Through ion milling the wide and open pore system inside the material becomes accessible for the indentation. The material roughness is increased due to this preparation technique. Therefore, ion milling without infiltration is no option for this porous copper material.

In a copper surface with a low arithmetic roughness, Sa, the residual indent should be seen [21]. Figure 24 illustrates, that the indent is only visible at OP-S and fine grinding. When the indenter geometry matches the roughness, the effective area is alternated which affects the load curve and leads to Hardness and Young's modulus overestimations [7].

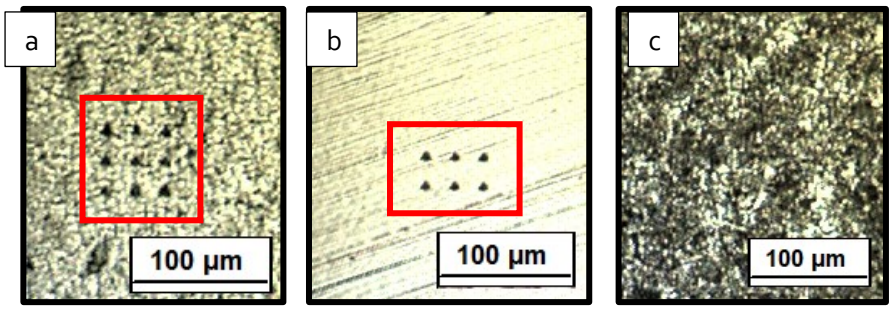

Figure 24; Surface after indentation provided through the light microscope included in the KEYSIGHT NanoIndenter G200. Residual indents are only visible at a) OP-S and b) Fine grinding. Exemplary for the other methods c) etching is shown. Here the roughness covers the indents.

4.2. Phase 2 – Infiltration techniques and main measurements

Through surface preparation no sufficient nanoindentation values could have been produced. Since, sample J2 has been infiltrated by crystal bond during the preparation process and the measured values, infiltration seemed to be a reasonable next step to obtain reproducible and stable nanoindentation values.

Thus, for Phase 2 the main samples (J2, J3, J4, J5) for this thesis have been delivered as foils. The term "foil" describes the state of a pure copper layer without a substrate. The foils have been stripped from the substrate, therefore every foil possesses a flat side (bottom side) and a structured side (top side). The samples have been produced with different paste material as given in Table 5, which has an effect on the material structure. First of all, a detailed characterisation regarding the surface and material structure of the samples J2, J3, J4 and J5 will be given before addressing the nanoindentation issue.

4.2.1. Surface microstructure of J2, J3, J4 and J5

Figure 25 shows only the four high contrast images of the four different batches, instead of a colour image and a high contrast one. This has been done because the high contrast image of the laser microscopy gives more information about the structure, than the colour image.

On first sight, the different paste material influenced the surface structure of the samples. Paste J1, used for the foil samples J2 and J4, results in a similar structure with big round particles and fine structured areas, but the shape of the pores is different. While for J2 the pores are elongated and look like rifts, the pores of J4 are round and look like dimples. The two remaining samples J3 and J5 possess both a different structure compared to J2 and J4, it is quite homogeneous and the particle size distribution is significantly smaller, than the one of Paste J1 samples. J3 and J5 have different pastes and it can be seen that from J3 to J5 the particles again got smaller and no pores can be defined inside the homogenous structure of J5. The sample J5 seems to consists only of fine structured area, similar to the one occurring in J2 and J4.

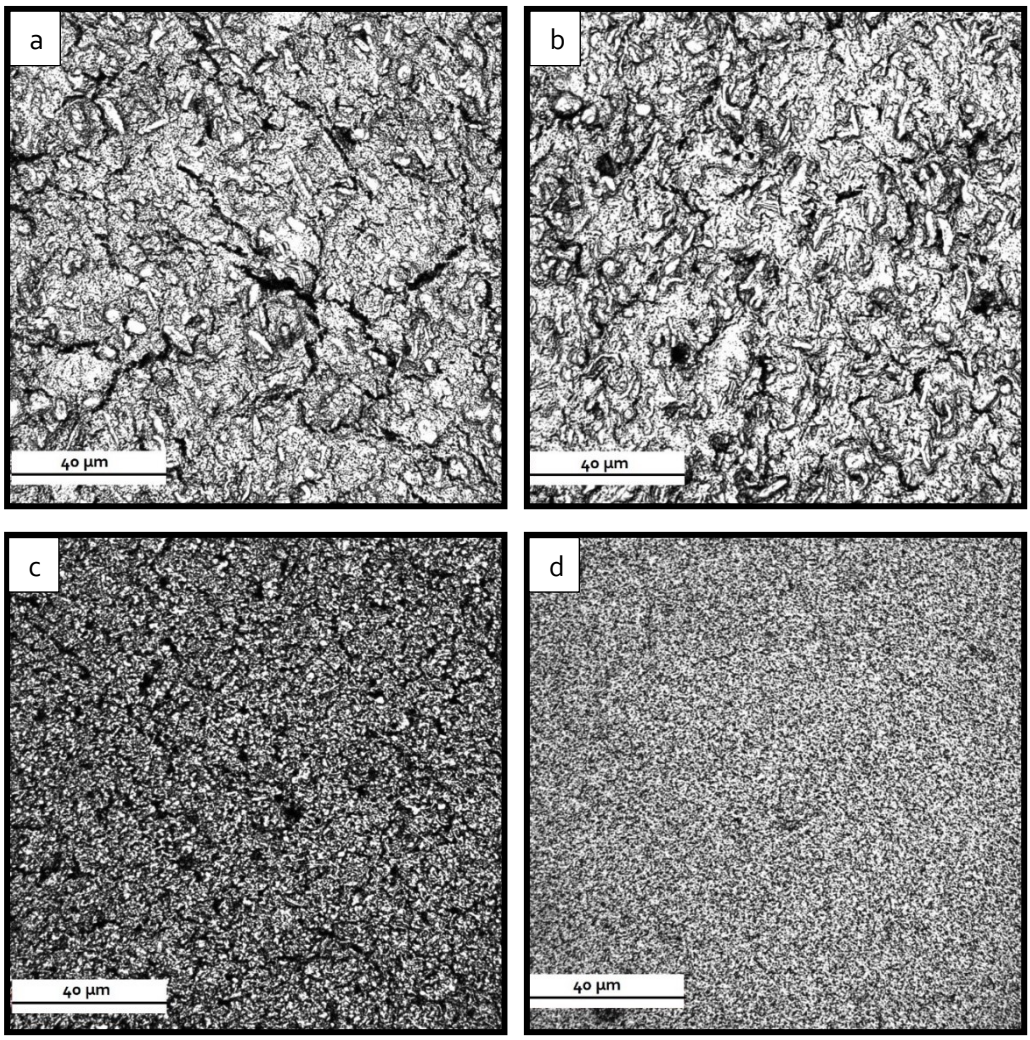

Figure 25;High contrast images from the LEXT laser microscope of a) J2, b) J4, c) J3 and d) J5. It can be observed, that for Paste J1 (a-b) a similar structure occurs. In a) and b) big round particles and fine structured areas can be observed, whereas the shape of the pores differs. For c) and d) the material looks homogeneous. Nevertheless, J5 possesses no detectable pores anymore, while J3 does.

4.2.2. Roughness parameters of J2, J3, J4 and J5

The roughness comparison of the four foils in Figure 26 shows that, as already declared in the previous chaptero the material J2 and J4 are similar, whereas differences of J3 and J5 could be seen clearer through the roughness analysis. In terms of the range one colour scale per line is given to indicate the colour of the lowest point (violet) and of the highest point (red).

The images give an area of 129 x 129 µm and for samples of Paste J1 the volume ratio of surface below and above the average line is, due to the colouration, nearly the same. In case of J3 there are concluded areas of dimples and tops with some peaks, but most of the surface is at one height level range (green to yellow). While for J5 most of the surface is at one level (all the same colour) with only some very small elevated areas, sinks are non-existing.

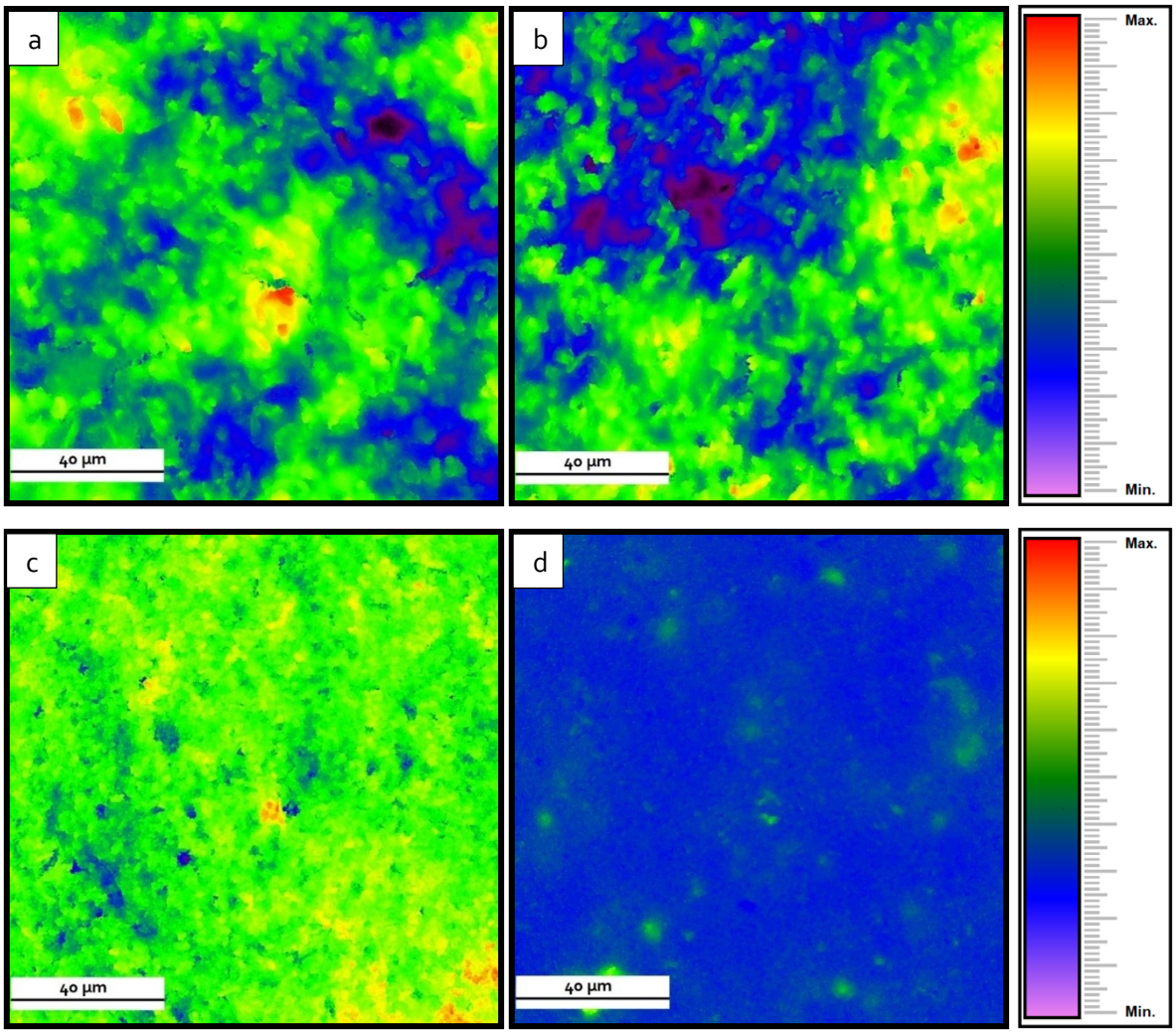

Figure 26; The topological charts of the surfaces a) J2, c) J3, b) J4 and d) J5 provided by the LEXT laser microscope. D) shows nearly no roughness, while c) seems mostly even with small peaks and dimples. A) and b) are identical from the roughness' point of view. There ratio between surface above and below the average roughness line is near to 50/50.

Table 15 and the Abbot-curves in Figure 27 confirm the conclusions of the height images in Figure 26. Again, a similarity between the samples J2 and J4 can be seen. Their maximum roughness height Sz is around 10.5 µm and their arithmetic roughness Sa is at 1.042 µm. Such a high value would neglect proper nanoindentation until an indentation depth of 20 µm according to M. Laurent-Brocq [8]. Between J3 and J5 no similar behaviour can be determined. But the values of J3 are better than those of Paste J1 samples. From the topological image of J3 unapparent but by the low value of the skewness (Ssk= 0.03) indicated, is that here also the ratio between surface below and above the average surface line is even. This is entirely different for the sample J5. Already guessed, but through the values confirmed is that the surface of J5 is settled at one height level (Sa = 0.12 ±0.01 µm) with only some inquiries. Especially mentioned should be the values of the kurtosis (Sku= 48.7 ±13.35). In combination with the topological image, where no peaks could be observed, the values indicate a few very small sized sharp asperities.

Table 15; Height roughness parameter values of the sample J2, J3, J4 and J5.

		Sq [µm]	Ssk []	Sku []	Sp[µm]	Sv [µm]	Sz [µm]	Sa [µm]
J2	**Mean**	1.321	0.315	3.233	5.659	4.692	10.351	1.042
	Deviation	0.145	0.183	0.400	1.319	0.334	1.651	0.106
J3	**Mean**	0.653	0.026	3.389	2.949	3.887	6.835	0.515
	Deviation	0.028	0.021	0.221	0.093	0.194	0.103	0.024
J4	**Mean**	1.341	0.733	4.258	6.763	4.213	10.976	1.042
	Deviation	0.032	0.504	1.514	1.077	0.448	1.244	0.039
J5	**Mean**	0.199	4.621	48.704	3.499	0.935	4.434	0.121
	Deviation	0.015	0.804	13.349	0.096	0.251	0.287	0.009

In the Abbott-curve the height [µm] is linked to the areal material ratio [%]. Out of Figure 27 (a), b), c) and d)) the values for the core roughness depth (Sk) the reduced peak height (Spk) and the reduced dale height (Svk) have been evaluated. The results are listed in Table 16.

The course of the Abbot-curve represents the structure of the surface. The Abbott-curve of J2 and J4 went up to around 7.7 µm, J3 only reaches 4.8 µm and J5 was not above 2. 9 µm. Surprisingly the course of the J2 and J3 curve are similar, only the range of the height for J3 is diminished. This led to considerations of a similar structure, but with a smaller dimension of particles and pores. The course of J4 is alike J2, but shows a characteristic of J5, the curve's end. This one ends in a shallow way, whereas J2 and J3 have been more pointed at the end. This indicates less steeper dales, respectively pores. This is verified by the intensity images in Figure 25. Where it can be seen, that the pore shape is round, while the pores of J2 are elongated. For J4 this cause, less pore closure and therefore a residual core roughness of 3.35 µm, the highest value of all the compared samples. With J5 the initial surface did not possess such high roughness. Mentionable is that only 3% of the surface of J5 possess roughness tips higher than 1 µm. Therefore, an initial abrasion process or surface preparation like polishing lead to a strong reduction of height (from a Sz of 4.3 µm to a Sk of 0.34 µm). To getter with the skewness (4.621) and the extreme kurtosis (48.704) the conclusion is that on the even levelled surface randomly scattered slightly elevated areas occur and on top them very small particles are located.

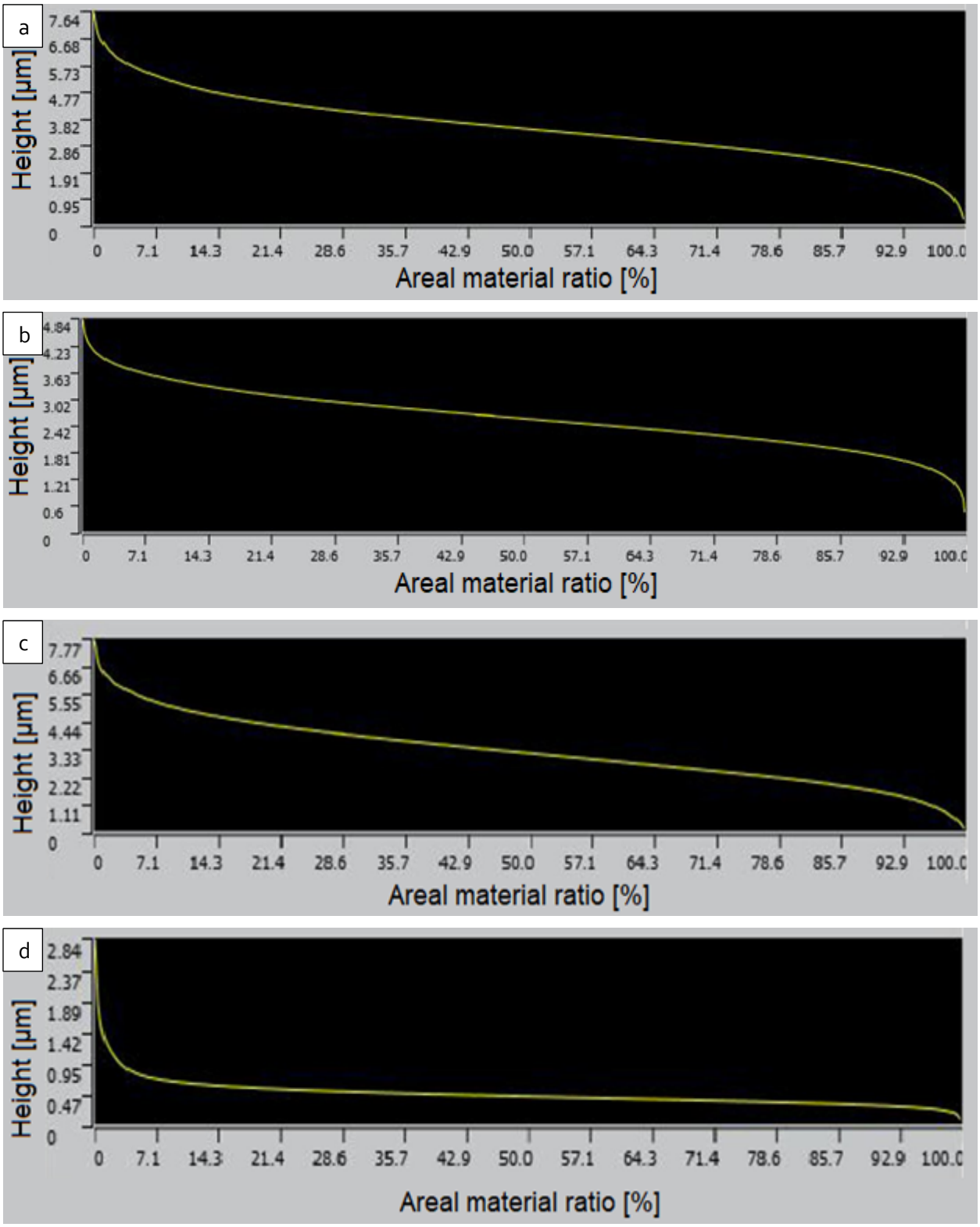

Figure 27; Abbott-curve of a) J2, b) J3, c) J4 and d) J5. The course of the curve are similar in a) and b), except of the height range. Some characteristic of the curve of c) can be found in an exaggerated way in the curve of d). The course of the Abbott-curve gives some conclusions in the surface structure, therefore, similarities between those samples. J5 is the only material where less than 4% of the areal material ratio have a roughness over 1 µm. For the other samples, nearly 99% of the areal material ratio are rougher than 1 µm.

Table 16, Functional roughness parameters (core roughness Sk, reduced peak height Spk, reduced dale height Svk) calculated from the Abbot-curve for J2, J3, J4 and J5. In comparison J5 is the most promising sample, based on homogeneous structure and uniformity of the surface.

	Sk [µm]	Spk [µm]	Svk [µm]	Areal material ratio [%]
J2	2.85	2.64	2.01	~99% of roughness tips > 1 µm
J3	1.71	1.22	1.47	~99% of roughness tips > 1 µm
J4	3.35	2.54	1.27	~99% of roughness tips > 1 µm
J5	0.34	2.05	0.26	~3% of roughness tips > 1 µm

4.2.3. Cross-section microstructure of J2, J3, J4 and J5

All cross-section of the samples J2, J3, J4 and J5 are illustrated in Figure 28. A similar structure for Paste J1 samples (J2 and J4) regarding the surface, as stated in chapter 4.2.1, can be verified. The surfaces possess a significant waviness with a height difference of about > 5 µm, whereas for the two homogeneous samples J3 and J5 no waviness can be observed and the height difference is < 5 µm.

The sample J2 is identical to J1, this is also concluded by the broad distribution of pore and particle sizes, shown in Figure 28 a). The material is made up by the big compact particles consisting of a number of grains, the sponge-like structure, which appears bluish in the light microscope and the highly connected pore system. The pores sizes in J2 are highly scattered.

From the sample of J3, in Figure 28 b), it can be guessed, that the porosity is higher. While the particles are less distributed than with base material J2. The top surface roughness is compared to J2, significantly smaller, which agrees with already measured roughness parameters. Small spired and dimples can be seen (white arrow), the dimensions are in the range of the particle size. The reddish glow might be from the backside of the pores, because nothing was changes at the microscopy during the measurements.

J4 is illustrated in Figure 28 c). The compact particles seem to be shaped more elongated and they are not as concluded as the round particles in J2. They resemble dendrites. Compared to J2, the area of fine structured material seems to be diminished, as are the pores. The porosity seems to be lower than the base material, but the compact grain size is smaller and there are more small pores. The top surface roughness is similar to J2.

At least Figure 28 d) shows the structure of J5. A homogeneous structure with a mostly even top and bottom surface with a homogeneous sponge-like structure consisting out of small pores and particles, can be seen. Some spires can be observed on the surface of J5 (white arrow). They have the dimension of one particle. The thickness is compared to the other samples significantly smaller. Due, to the light microscopy the structure of the sample cannot be defined, but the SEM measurement clarified the sponge structure.

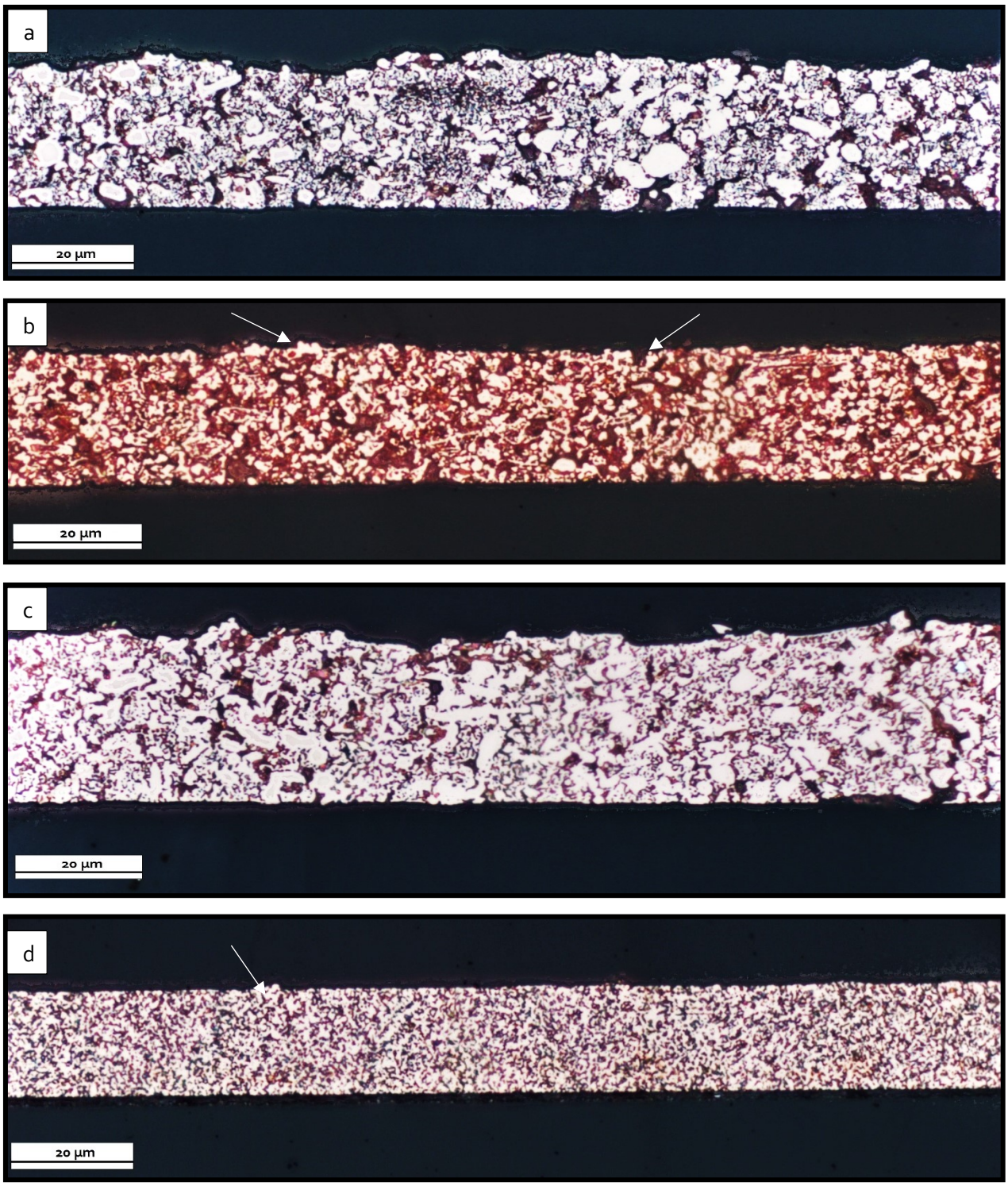

Figure 28 LIMI-images. a) Structure of J2 is identical to J1. Particles with sizes between some hundred nanometres and a few micrometres are surrounded by pores of different sizes. b) describes the structure of J3. Smaller particles and a higher ratio of pores are part of the appearance of J3. Compared to J2 and J4 the surface is flatter. Surface structures are at the range of its particles (arrows). The reddish glow might be from the backside of the pores, but this cannot be confirmed sufficiently. c) illustrates the structure of J4. The compact grains seem to be shaped more elongated and not as concluded as the round particles in J2. Compared to J2 and the area of fine structured material seems to be diminished, as are the pores. d) shows the structure of J5. A homogenous structure with an even top and bottom surface with sometimes small spires (arrow) can be observed. The thickness is compared to the other samples significantly smaller. The fine structure consists out of nanoscale pores and particles, this was confirmed through a SEM.

4.2.4. Porosity measurement

The porosity has been measured in two ways and also compared with the ongoing work of A. Wijaya dissertation [23]. The porosity measurement have been performed on two different kinds of images. First a coloured image was used and second a binary image. The colour images have already been discussed and illustrated in Figure 28. In the binary images of J2, J3, J4 and J5 are shown in Figure 30. For a better comparison, altogether they have been shifted to the next page. Through the change to binary a clearer image on the sponge structure has been expected. Through the higher contrasting a better differentiation could be made, especially if combined with the image preparation steps of dilation and erosion, the particles should be more defined.

From the binary images, the conclusion can be made that J2 and J4 are characterised through their wide scattering of particle size, while J3 and J5 mainly composed out of one particle size. The particle size distribution causes the effect, that J2 and J4 include particles which are smaller than those of J3. Especially J4 shows, compared to J2 and J3, more fine structure similar to J5 in the region of the surface. This might explain the similar Abbott-curves characteristics of J4 and J5, whereas the particle distribution of Paste J1 sampls leads to the identical rising of the Abbott-curves. For J3 and J5 the total height and Sk are lower, due to their homogeneous particle dimension. The binary images agree with our previous findings.

For the porosity measurement, the ROI have to be defined, some examples are illustrated in Figure 29. Both methods have their problems due to the threshold adjustments of the images. For the binary image transformation, the different grey values have to be considered, while with the coloured image the definition of a particle boundary is the main source of error. More sophisticated method to analyse the porosity are performed in the connected dissertation [23] regarding CT and SEM/FIB Tomography for 3D analysis of the material and pore structure, one example is listed in Table 17.

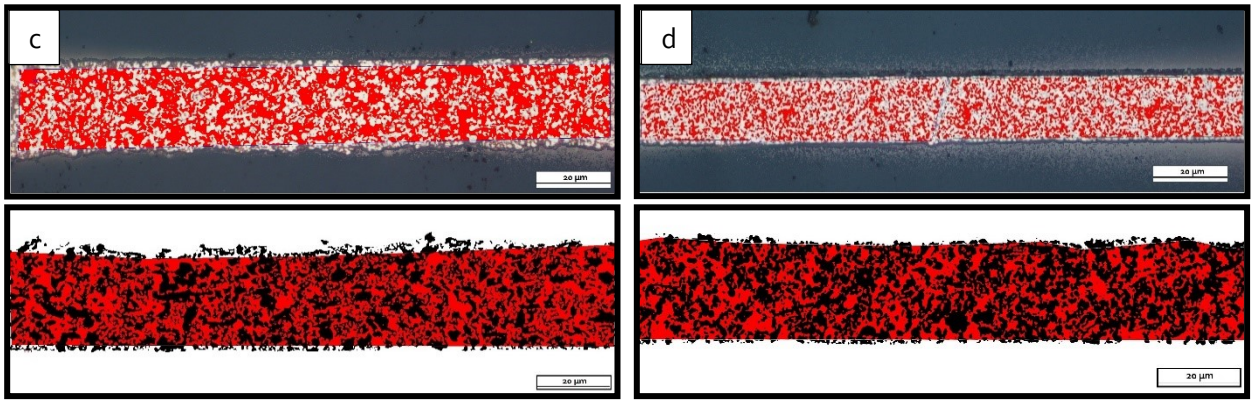

Figure 29; Exemplary images of the ROI analysis on the samples done with the Motion STREAM software included at the LIMI. a) colour image of J3 b) colour image of J5 c) binary image of J4 d) binary image of J2.

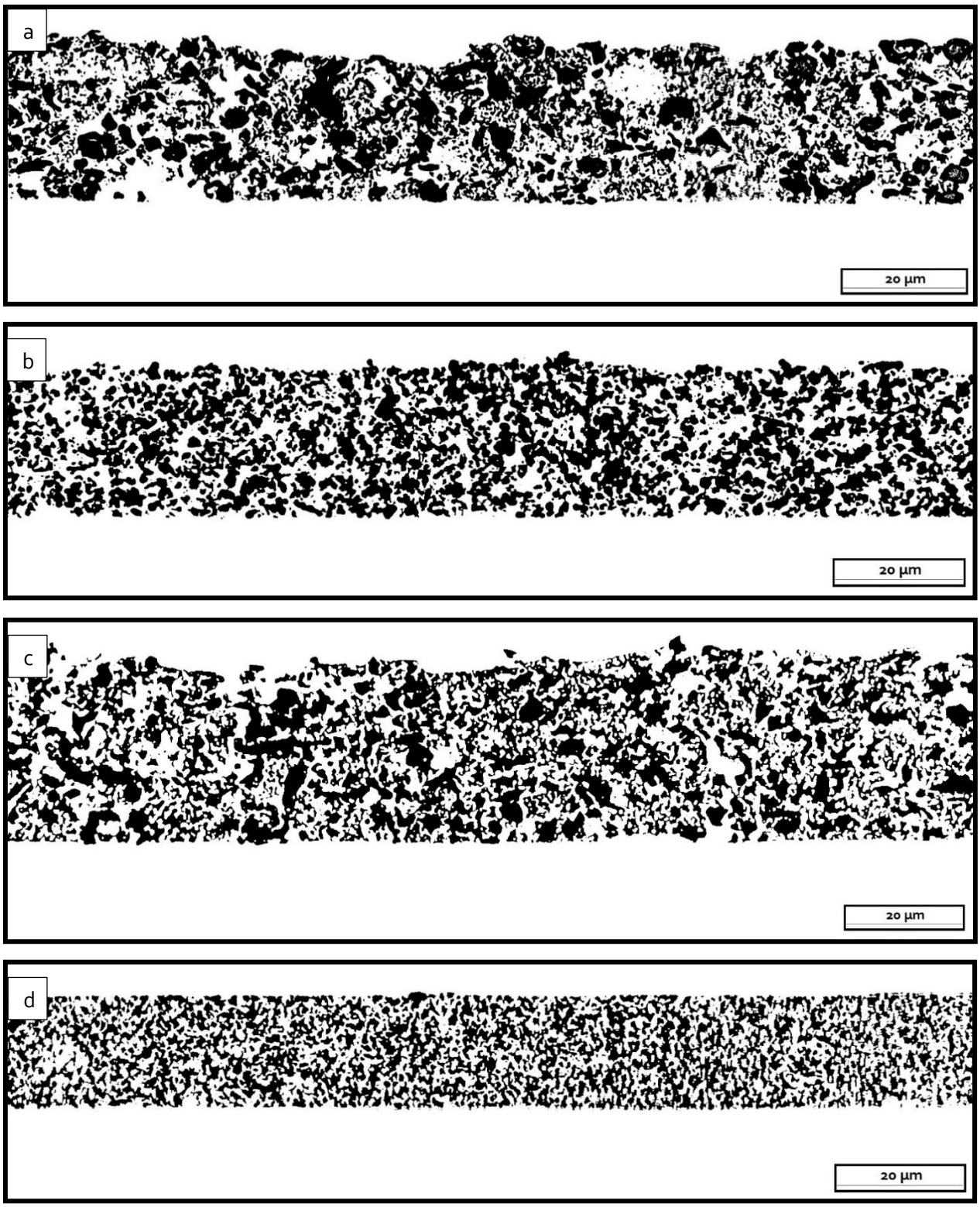

Figure 30;Through Motion STREAM converted Binary images a) Structure of J2 as binary image. A high particle and pore size distribution can be seen, along with a wavy top surface. b) Structure of J3 as binary image. It seems to be quite homogenous regarding the particle size. But the material is lacking the fine structured particles seen at the other samples c) Structure of J4 as binary image. Pore structure seems to be more homogenous than in J2. Also the particle structure differ from J2, because they seem to be more elongated with a higher ratio of fine structured particles d) Structure of J4 as binary image. It looks homogenous and fine structured. The surface appears flat.

In Table 17 the results from the porosity measurements and the comparison values are listed. It can be seen that the deviations between the different methods are significant.

Table 17; Porosity values for different analysis methods like gravimetry, binary and coloured porosity measurement. The sophisticated method of the SEM/FIB Tomography preliminary bymanual segmentation have been provided by A. Wijaya [23] *(effect. 15-Sept-17).*

Porosity analysis	Gravimetric (company) [%]	Binary image LIMI [%]	Colour image LIMI [%]	SEM/FIB Tomo. manual seg. [%]
J2	30	38.6	36	33.5
J3	60	44.0	55.4	55.1
J4	40	55.1	43.1	31.1
J5	20	49.6	36.7	36.1

4.2.5. Material preparation – Infiltration possibility and methods

Tests on J1 showed insufficient infiltration. This caused a three-phase system, which is way more complex for handling and calculation than the desired two-phase system. Air is still entrapped inside the material, especially near the silicon wafer. In Figure 31.a) a light microscope image is shown, while b) is a laser microscopy image. The entrapments are marked with arrows. From the light microscopy image, the air bubbles could be guessed, due to darker parts inside some pores, but not clarified. The laser microscopy (Figure 31 b) with its different intensity levels made the identification of the residual air easy. Additional air bubbles on the surface could be seen as well. Those would not affect the measurements, but may indicate insufficient infiltration. Since the location of the entrapments is mainly close to the wafer, a repetition of the infiltration experiment without silicon seemed to be promising.

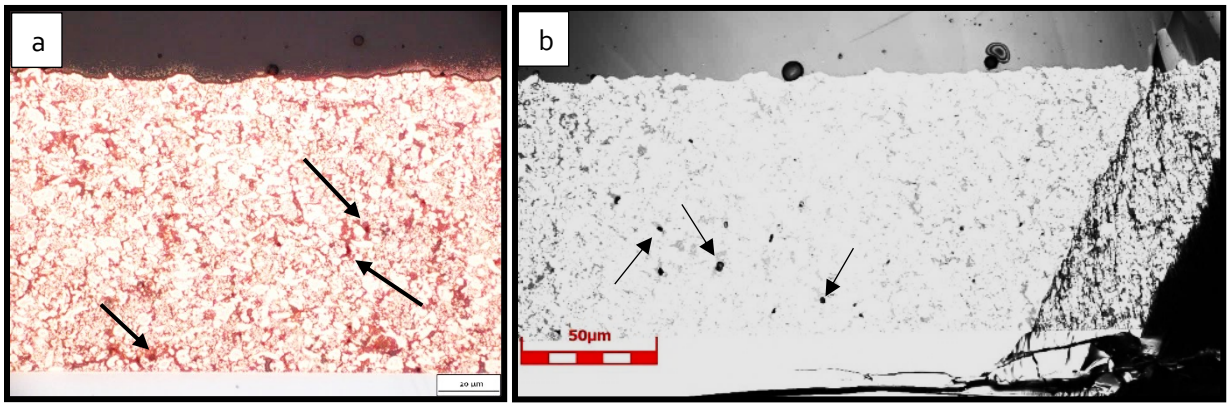

Figure 31; Entrapments of air can be seen in a) as slightly darker spots (provided by LIMI). Better is the use of the LEXT laser microscope, as can be seen in b) Here the entrapped air can be seen as dark dots on the bright surface.

All further experiments to infiltrate the material have been performed on J2. Ultrasonic enhanced infiltration failed already at the first visual inspection after sample preparation, due to insufficient filling. Therefore, nanoindentation had only be accomplished for the acetone diluted and the vacuum enhanced infiltrated samples.

Due to similar performance of both techniques (chapter 4.2.6), but the advantage of time saving in case of vacuum enhanced infiltration, all the samples for the main nanoindentation measurements have been infiltrated though the vacuum enhanced method. After infiltration, cutting and the final ion milling the samples reside with a polished surface in the shape of a lens, as seen in Figure 32. The boarders of the lens are steep with a drop of around 70 µm. To prevent the indenter from contacting the boarder of the lens, it has to be wide enough, which is possible but to the expanse of time during the ion milling process.

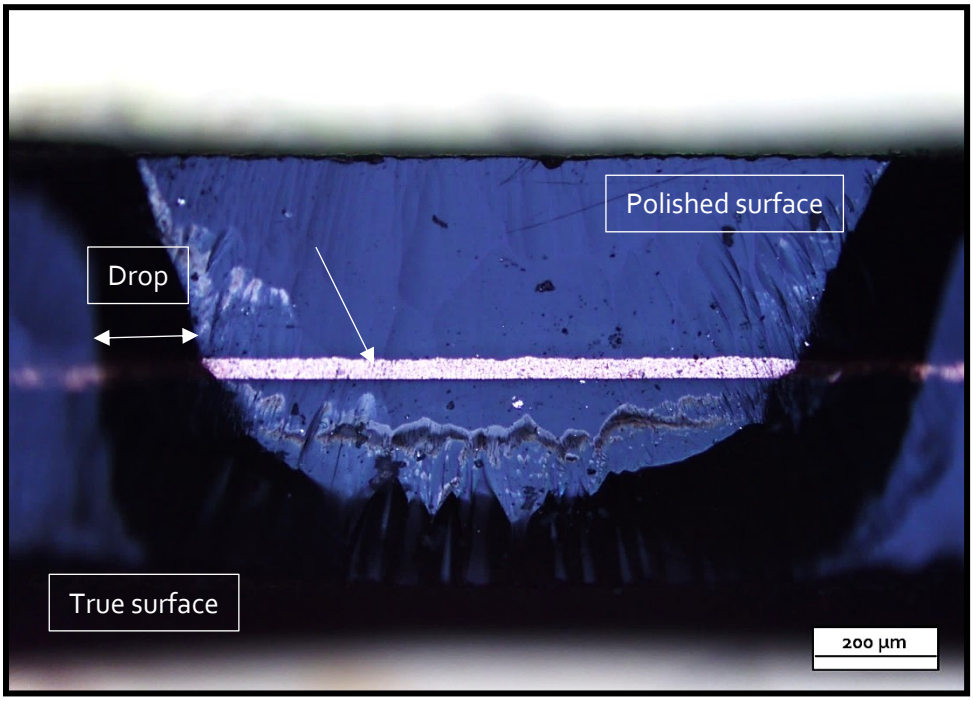

Figure 32; Exemplary picture for the infiltrates after ion milling process using the LIMI. The arrow marks the infiltrated samples. Around the foil is the epoxy resin. Between the polished surface and the true surface is a height difference of minimum 70 µm. The residual lens has to be broad enough to guarantee the indenter to penetrate the surface and not rest on the boarder. The sample on the picture is J5.

4.2.6. Nanoindentation of the infiltrates

Infiltration method: After dismissing Ultrasonic, the two residual methods, acetone dilution and vacuum enhancement, have both been indented. After accurate viewing of every value of the (Figure 33, a) load-displacement curve, b) plateaus of load-displacement curve) and scrapping the outliers the acetone values have possessed the smaller deviation, but both deviations have been under 10% and therefore been valid. As can be seen in Figure 33 c) and d), where the curves are stable in the analysis range of 800-1000 nm. The production of the vacuum assisted samples was less time consuming, as a result, vacuum enhanced infiltration has been considered for all further experiments.

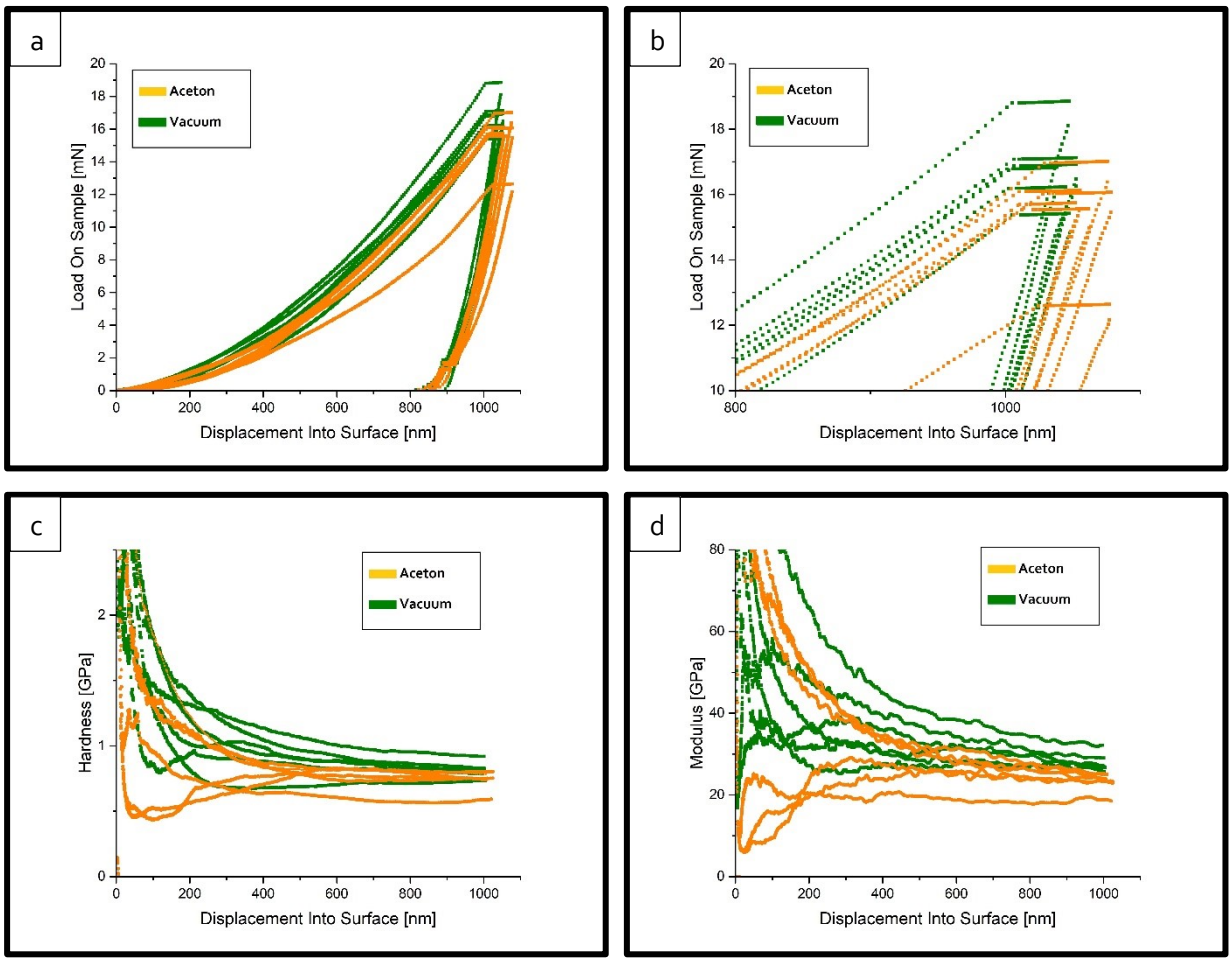

Figure 33; The indenter curves of J2, where the comparison of the two remaining infiltration techniques are illustrated in a) load-displacement-curve, b) focus on the plateaus, c) Hardness-curve and d) Young's modulus-curve. Both material still show deviation, but it is inside the allowed limits for vacuum and after scrapping of the outlier also for acetone.

The values differ from each other, as can be observed in Table 18. The determined values of J2 with acetone have been $E^* = 26.2 \pm 3.5$ *GPa* and $H = 0.74 \pm 0.09$ *GPa* and for vacuum, those have been $E^* = 31.6 \pm 2.5$ *GPa* and $H = 0.83 \pm 0.07$ *GPa*. After elimination of the outliers the acetone values have been $E^* = 25.3 \pm 1.4$ *GPa*, $H = 0.78 \pm 0.02$ *GPa* and therefore be valid, but Vacuum was chosen, due to less time-effort.

Table 18; Comparison of the two remaining infiltration techniques, vacuum enhancement and acetone diluted samples. Those have been performed on the sample J2.

		Red. E-Modulus	E-Modulus	Hardness	Drift Corr.	Temperature
		GPa	GPa	GPa	nm/s	C
Acetone	Mean	26.2	24	0.74	-0.087	27.1
	Std. Dev.	3.5	3.3	0.09	0.027	
	% COV	13.33	13.59	11.96	-31.19	
Vacuum	Mean	31.6	29.2	0.83	-0.011	27.1
	Std. Dev.	2.5	2.4	0.07	0.025	
	% COV	7.84	8.07	8.98	-225.49	

Infiltrates: After vacuum enhancement has been defined as the infiltration technique for usage, all foils have been infiltrated and measured with the nanoindentation parameters mentioned in Table 10. In Figure 34 the nanoindentation load-displacement curves of the composites are shown. The measurements of all samples are illustrated in relation to each other. The scattering and the range of J2 and J4 are similar. For J5 all ten measurements look nearly as one. This is caused by the homogeneous fine structure. The small structure of J5 promotes that every indentation tests the same material structure. The sample J3 as seen in the Figure 34 can be distinguished in two groups. The structure of J3 is homogeneous, but due to the high porosity it originates in 2 plateaus for a composite, Group 1 with mainly copper with a plateau level around 11 mN and Group 2 for mainly epoxy resin with a plateau level at 9 mN. This is caused by the material structure. For a homogeneous structure the covariance is lower, as for a heterogeneous structure. But, if the dimension of the epoxy resin areas increases, the possibility for the indenter tip to contact a high ratio of epoxy increase as well. In case of the heterogenic J2 and J4 a clear separation of the plateaus could not be observed.

In Figure 36 and Figure 35, the Young's modulus and Hardness curves focused on the analysis range [800 -1000 nm]. As given in the legend, the dotted lines are displayed in different symbol for every sample to make it possible to distinguish them better. A more detailed look on J5 is given in Figure 41 and Figure 42. The samples are easier to separate at the Hardness measurements (Figure 35). The highest Hardness values are measured for J5 (Figure 35). The measurements of J2 and J4 are intertwined with each other. The values of J3 again are settled at lowest, here again two clear separated groups (Group 1 > 0.5 GPa, Group 2 < 0.5 GPa) can be seen. This, as already explained, originates in a level for mainly copper volume or mainly epoxy resin volume beneath the indenter tip. In case of the Young's modulus (Figure 36) J3 values are twice as low as the other samples, which are resting around a value of 32 GPa. J4 is located at the upper end and slightly mingles with the measurements of J2, which is located at the lower end. For the values of J5 the scattering is minimal and can be found in between the main areas of J2 and J4.

In Table 19 all the values as measured are given. The covariance of the samples are below the 10% threshold except the Hardness from J3, but after further examination of the values and elimination of the lower mainly epoxy resin influenced group the residual values for the Hardness settled at H= 0.58 ± 0.03 GPa, which is equivalent to a covariance of 4.41 % and the E^*= 17.00 ± 0.60 GPa with a covariance of 3.51% Additional to the outstanding performance of J5 with a covariance of < 2%, it can be said, that the homogeneous structures results in a stable nanoindentation measurement. The deviation of the modulus is similar to the one of the Hardness, not like in the former nanoindentation where the Hardness deviation commonly was twice the deviation of the modulus.

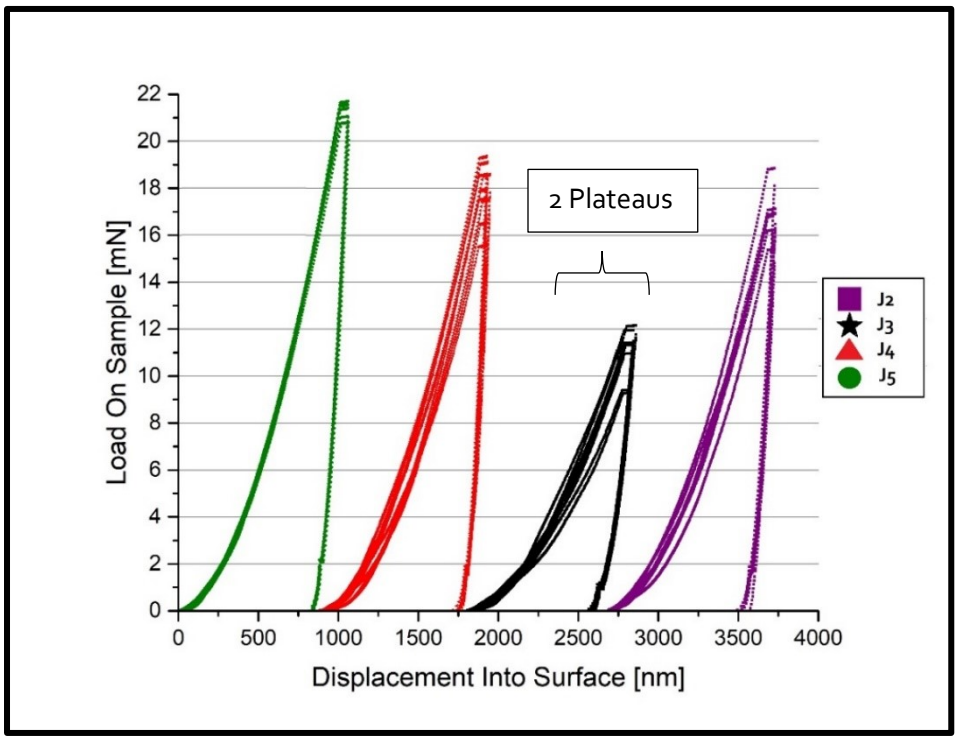

Figure 34; Load-curves of J2, J3, J4 and J5 over the indentation depth. The samples indent curves are shifted to see each on their own. J5 possesses nearly no scattering, the values are highly reproducible. J3 is recognisable smaller, due to its higher porosity. There are two groups of load plateaus visible, those might depend on the ratio of epoxy resin beneath the indenter. J2 and J4 are similar in their scattering and plateaus.

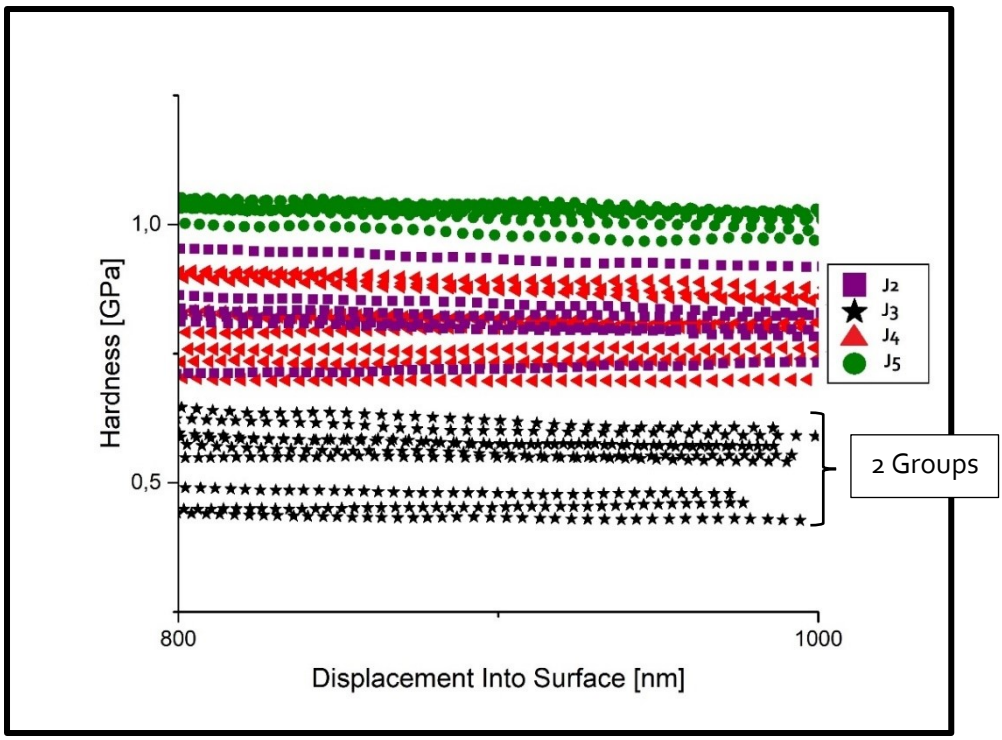

Figure 35; Hardness of the samples J2, J3, J4 and J5 are shown. J3 consists of two plateaus, one for mainly copper volume beneath the indenter tip and the other one for mainly epoxy resin. J5 is settled at the top end of the sample values, while the measurements of J2 and J$ are intertwined. The value of J5 are nearly congruent.

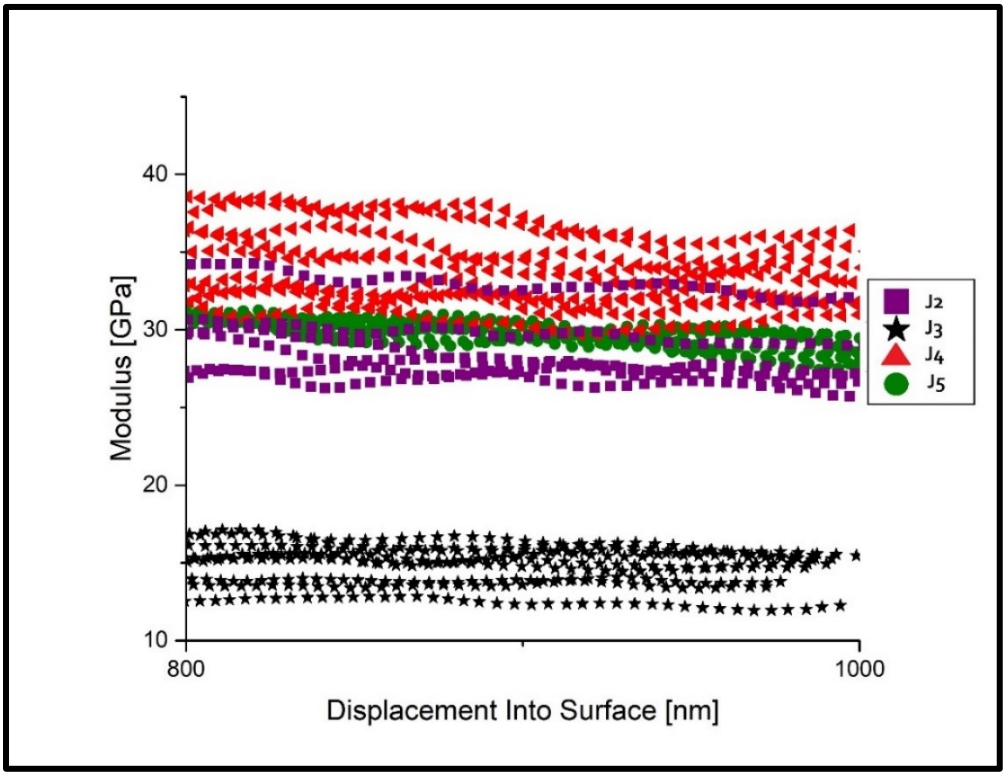

Figure 36; Diagram of the Young's modulus values in the area of analyzation [800-1000 nm]. The values of J3 are significantly lower than the rest. The measurements of J2, J4 and J5 are intertwined in a field around a value of 32 GPa. Nevertheless, J5 measurements are nearly congruent, while the measurements of J2 and J4 a broadly scattered. J4 is settled at an upper end of the field, while J2 is settled at the lower end of the field

Table 19; Measured values of J2, J3, J4 and J5 infiltrated through vacuum enhancement. Next to the Young's modulus the shear modulus is given, it will be needed for the calculation of the advanced models of mechanical behaviour. The Hardness covariation values are above the threshold of 10 %. However, if only the values of J3 for the upper level are considered, the %COV is beneath 4% for Hardness and the reduced Young's modulus.

		Red. E-Modulus	E-Modulus	Red. G-Modulus	G-Modulus	Hardness
		GPa	GPa	GPa	GPa	GPa
J2	Mean	**31.6**	**29.2**	**11.70**	**10.81**	**0.83**
	Std. Dev.	2.5	2.4	0.92	0.87	0.07
	% COV	*7.84*	*8.07*	*7.84*	*8.07*	*8.98*
J3	Mean	**16.2**	**14.8**	**6.00**	**5.48**	**0.54**
	Std. Dev.	1.4	1.3	0.52	0.48	0.07
	% COV	*8.62*	*8.74*	*8.62*	*8.74*	*12.55*
J4	Mean	**36.2**	**33.8**	**13.41**	**12.52**	**0.81**
	Std. Dev.	2.3	2.2	0.85	0.82	0.07
	% COV	*6.35*	*6.56*	*6.35*	*6.56*	*8.45*
J5	Mean	**32**	**29.8**	**11.85**	**11.04**	**1.02**
	Std. Dev.	0.5	0.5	0.18	0.17	0.02
	% COV	*1.49*	*1.53*	*1.49*	*1.53*	*1.75*

4.3. Nanoindentation Progress

4.3.1. Nanoindentation Progress using the example of J1/J2

For a better understanding of the progress the nanoindentation has been taken, three measurements of the sample J1/J2 from the different phases will be compared to each other. To make the comparison of the measurements easier the range of all the figures is the same. Thus, the Phase 1 and 2 measurements have been performed with a determined depth of 1000 nm, the pre-test data is also given only until this range. The diagrams Young's modulus and Hardness start with 200 nm, because at the beginning the scattering is not relevant for the analysis.

The basis of the nanoindentation performance has been determined at pre-tests. Here a broad scattering and deviation have been characteristic. Phase 1 involved surface preparation, where the OP-S was the leading method. Especially the offset was improved through this method. The roughness of the material could be diminished to level the surface and the true material structure at the surface was still intact after this polishing process. But the uncertainty of the pore geometry and system influence on the measurement regarding a proper hydrostatic core of the Poisson's ratio occur. This especially affects the Hardness. At the end Phase 2 included the material preparation through infiltration. Here the material performance in total has been improved, through minimisation of the pore influence inside the material and a smooth surface through ion milling.

As can be seen in Figure 37 a) the plateau scattering of the base material reaches from 4 to 18 mN, whereas for the two preparation techniques this could be diminished in an acceptable range (Figure 37.b) and c)). The set-off of Figure 37 b) is better than the one in Figure 37 c) but the further course of the load-displacement curves are more uniform with the infiltration. This relates to the stable hydrostatic core beneath the indenter tip, which is possible, due to infiltration.

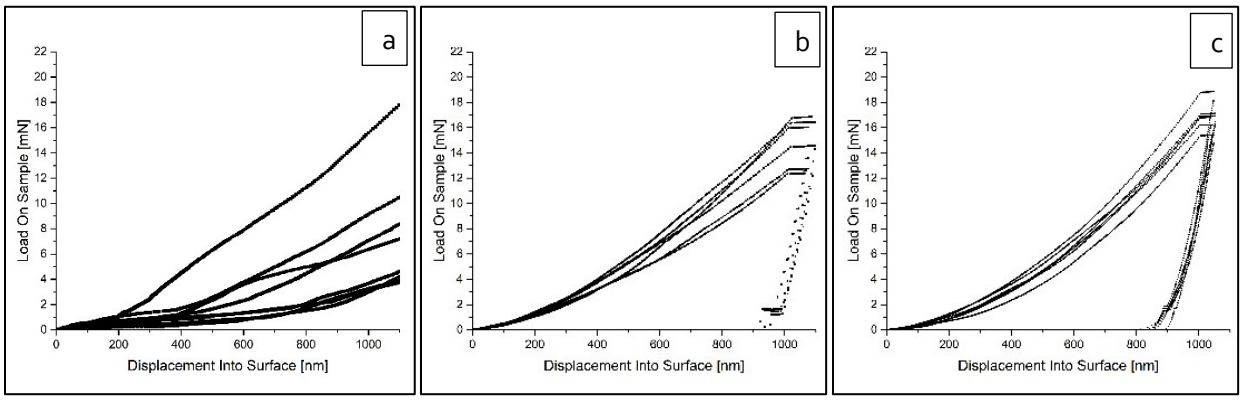

Figure 37; Development of the load curve behaviour a.) Pre-test J1 b.) OP-S J1 c.) Infiltrated sample J2 (same structure as J1, but sufficient filling)

In Figure 38 a closer look at the offset has been taken. At the basis material (Figure 38 a)), next to the broad scattering some pop-ins, marked through red arrows, could be seen, which indicates immediate deformation or lose breaking of oxides at the surface. As already mentioned the offset of b) presents itself as more uniform than c). This is related to the good surface preparation, where material structure is still intact, but no large pores or particles lead may cause surface roughness. While in case of c) the ion slicing produces a surface where copper particles and epoxy resin fields of different size exist next to each other. Copper and epoxy possess different material properties. If the indenter tip indents an area mainly of epoxy resin, the response would be different than for an area which consists of copper sponge or copper particles.

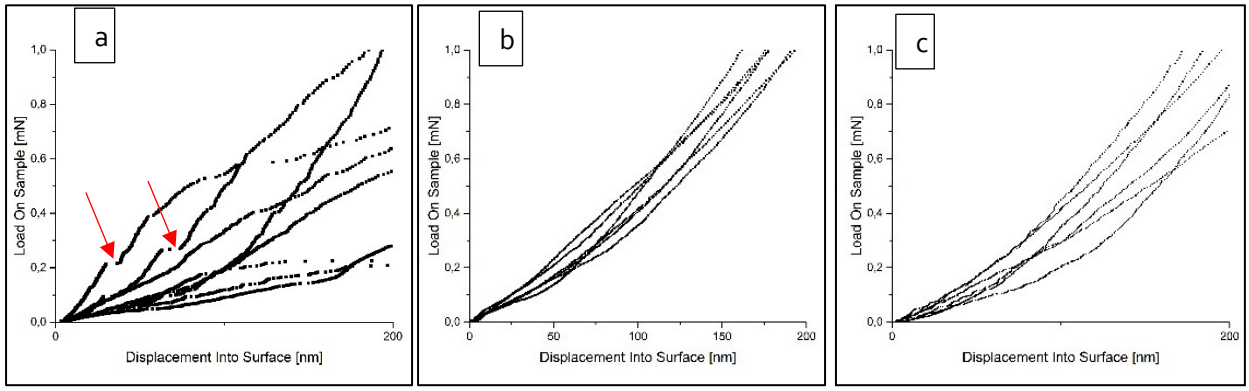

Figure 38; Development of the load curve focusing on the offset a.) Pre-test J1. Red arrows mark two examples of pop-in effects. b.) OP-S J1 c.) Infiltrated sample J2

The Hardness development, as can be seen in Figure 39 show that a) is of no use with a range from 0.1 up to 0.75 GPa. When b) is compared with c) the deviation from c) is better, due to the severe falling of the values in b). The deviation of the infiltrated material c) is similar for modulus and Hardness, but for the OP-S material while the modulus is extremely well, the Hardness is not sufficient, because the deviation value is higher than the recommended 10%, as can be seen in the Table 13.

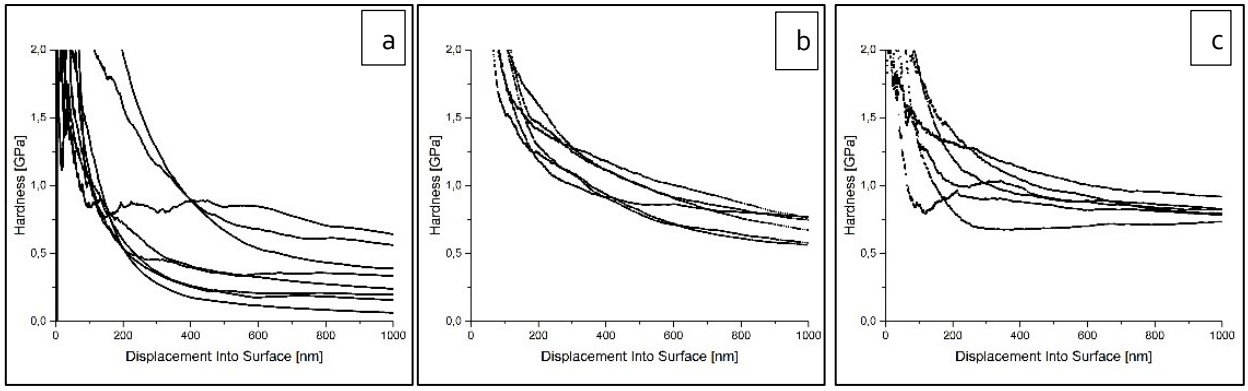

Figure 39; Development of the Hardness curve a.) Pre-test J1 b.) OP-S J1. The values are still falling at the end. c.) Infiltrated sample J2. Here the values run into a steady level at the end.

The development of the Young's modulus can be seen in Figure 40. The scattering at the first measurement made the evaluation worthless. Through the preparation techniques this has been be changed. The Young's modulus had been sufficient for both techniques, the values of b) have been even better than the infiltrated material, as can be seen if Table 13 gets compared with Table 19. The values should stable to use them without further questioning. This can be said for c) but in b) the settling was not finished.

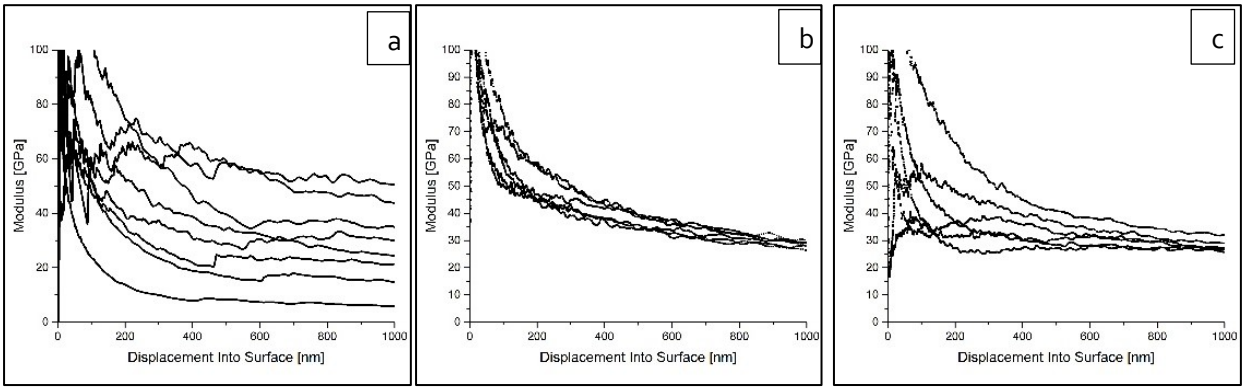

Figure 40; Development of the modulus curve a.) Pre-test J1 b.) OP-S J1 c.) Infiltrated sample J2

Finally, it can be said that the both preparation techniques have their advantages, but to generate sufficient Hardness and modulus values without further investigation the infiltration seems to be more reasonable. With just a few enhancements the nanoindentation measurement could be stabilised. If the material is able to be infiltrated, as in case of the open-porous copper, stable values can be guaranteed. But it is still a time-consuming procedure, which need a minimum of three days until nanoindentation measurement can be done. Whereas with the OP-S the surface is prepared in about a half day. But there are still problems depending on the material structure, like if a homogeneous structure is present, pore shapes, pore density, etc. to completely accomplish the task of sufficient values, for Hardness it is even more critical than for the Young's modulus.

4.3.2. Stabilisation through infiltration using J5 as example

With the infiltrated sample J5 an outstanding reproducibility of nanoindentation values could be reached (COV = 1,53%). As an additional confirmation of the good stabilisation effect, a sample of J5 but without infiltration, called J5 SK, has been measured with the nanoindenter. The stabilisation due to the infiltration process is illustrated in Figure 41 and Figure 42. Here the load-displacement, Young's modulus and Hardness curves of the infiltrated J5 are opposed to the samples without infiltration.

In Figure 41 a) the load-displacement curve of J5 is shown, and it cannot be denied, that the single measurements are congruent. For the sample J5SK (b) the plateau scattering is again significant. Even if

the offset of J5 scatters (Figure 42 c), it is nothing compared to previous measurements. An uniformity in the course of the curves can be seen, unlike with the J5SK sample (d), where pop-ins can be seen, additional to the broad scattering, due to the surface roughness.

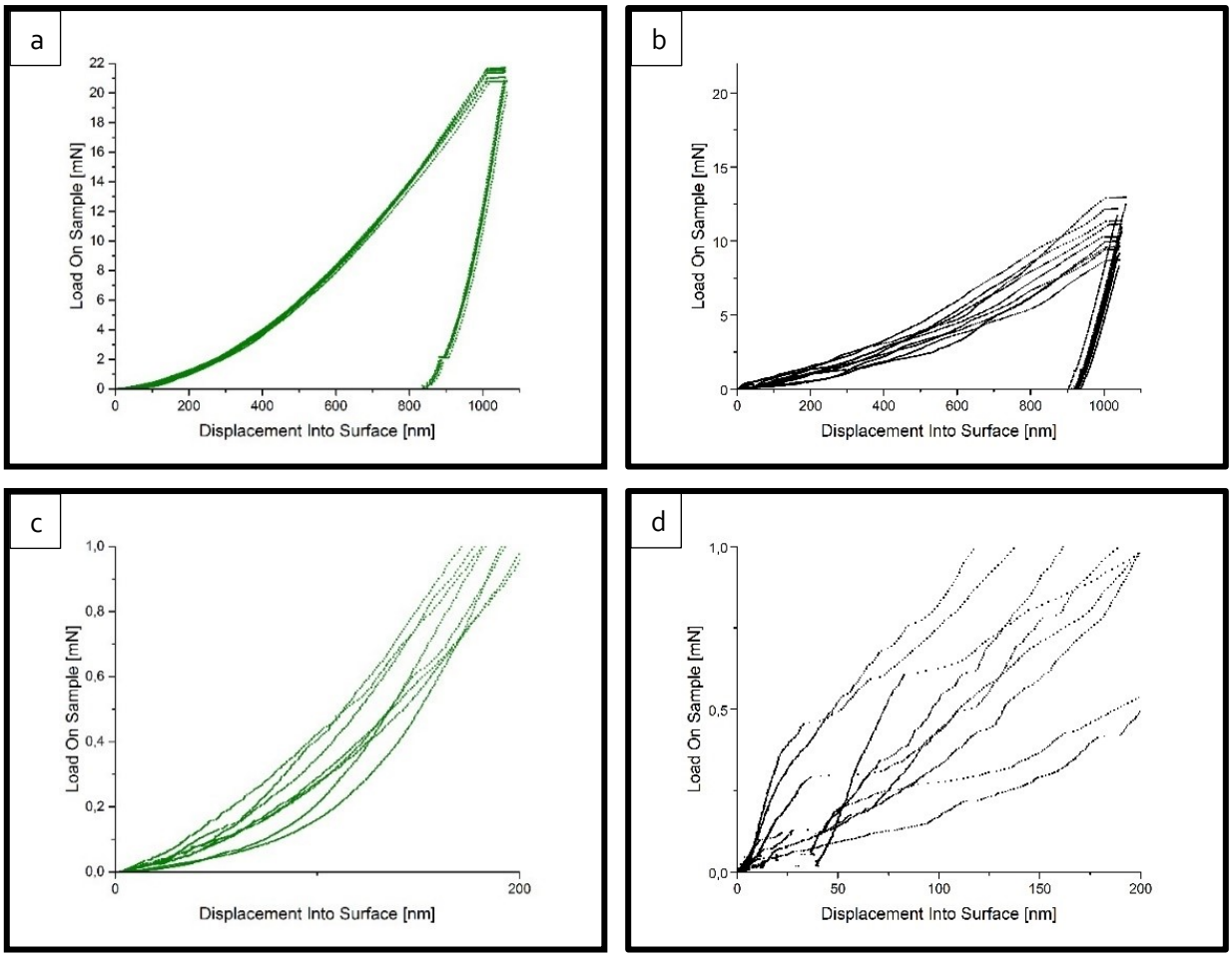

Figure 41; Comparison of indentation of the infiltrated composite sample J5 (green, left side) and the open-porous material as produced J5SK (black, right side) All diagrams are given for the same range. Next to each other are illustrated the Load-displacement curve of a) J5 and b.) J5 SK; The plateau of the composite is higher. This is reasonable, due to the fact, that the mechanical properties of both components in a composite add up. Load-displacement curve focus on offset of c) J5 and d) J5 SK; The surface roughness of J5 SK has a severe effect on the measurement. The error propagates along the entire measurement.

In Figure 42 a) and b) the two Hardness curves can be compare with each other. The Hardness curve agrees to the former discussed case illustrated in Figure 39. The deviation of the infiltrated material is similar to the deviation of the Young's modulus, whereas the deviation of J5SK is nearly three times higher, as can be seen in Table 20. The modulus of J5 in Figure 42 c) is even better than the OP-S worked sample discussed in Figure 40 b). Even the unaltered sample J5SK possess a sufficient modulus, as can be seen in Figure 42 d). With the infiltrated sample J5 it can be stated that until an indentation depth of 350 nm, marked through the orange box, the values are stable. This is exact the value of the core roughness Sk, given in Table 16. This seems reasonable, because Sk gives the residual roughness of a worked surface.

Beneath this depth the indenter is in full contact with the "average" material volume and the values stabilise. For J5 SK the values also settle for a level at around 400 nm, but the open-porous structure and the porosity lead to a heterogeneous response beneath the indenter tip and cause the scattering.

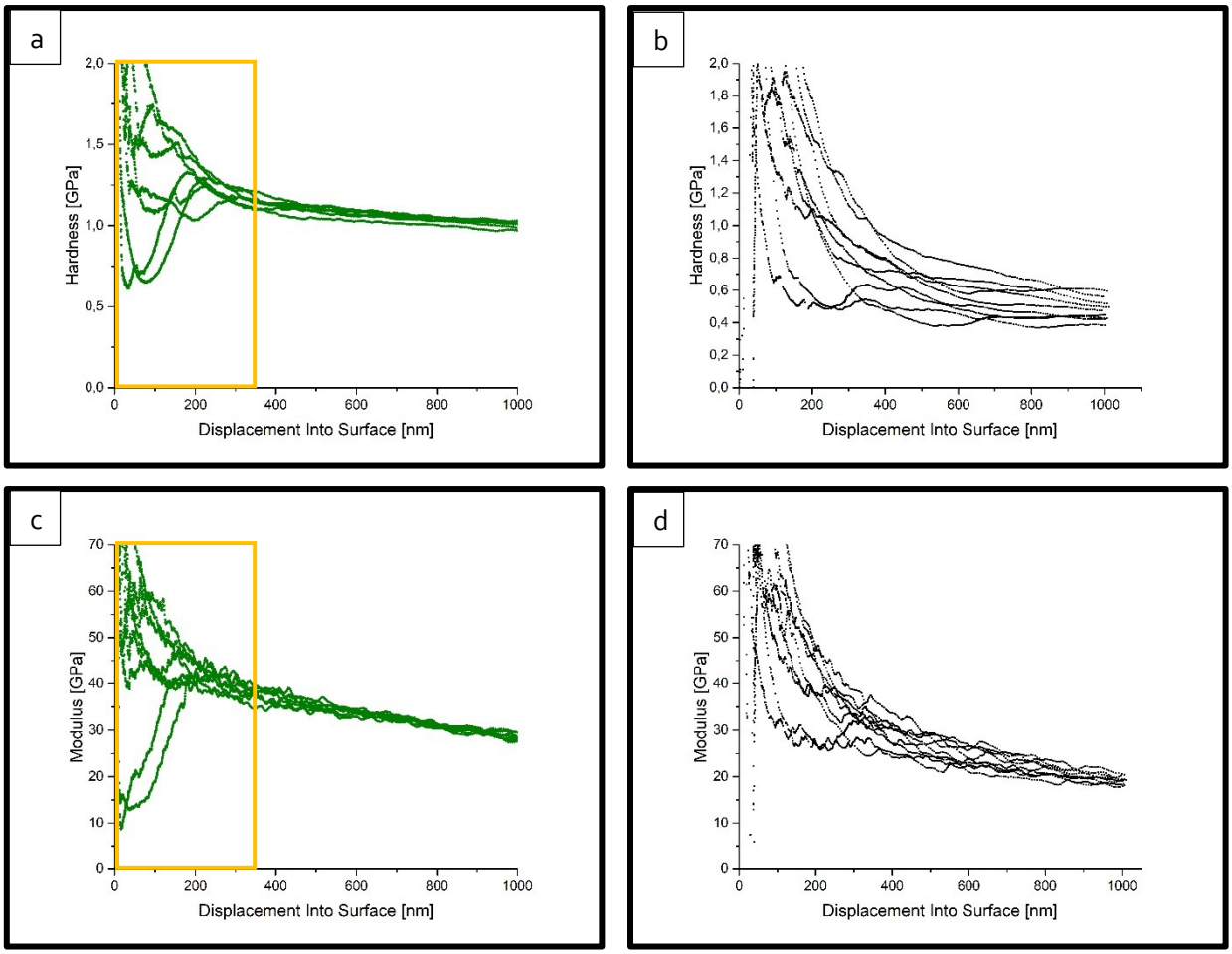

Figure 42; Comparison of indentation of the infiltrated sample J5 (green, left side) and the material as produced J5SK (black, right side). All diagrams are given for the same range. Next to each other are illustrated Hardness curve of a) J5 and b) J5 SK; The Hardness values is higher, because it is a composite not a porous material. Nevertheless, the covariance is remarkable small, whereas the Hardness value of the J5 SK is above the allowed threshold. Both curves settle at a level. Young's modulus curve of c) J5 and c) J5 SK; After reaching a depth beneath the core roughness Sk (orange box), the measurement became more congruent. In case of j5 SK the Young's modulus values scatter less than the Hardness values, which agrees with previous findings in this thesis.

The two measurements are numerical compared to each other in Table 20. The covariance (COV%) of J5SK for Young's modulus is below 10%, therefore the nanoindentation measurements are valid. But as for the OP-S worked material the covariance on the Hardness is more than twice as high as the COV% of the modulus and therefore, it is not valid. The values of J5SK are expected to be lower, than the values of the infiltrated sample J5, because it is not a composite and the ratio of the epoxy resin is missing.

It can be concluded, that infiltration is a good method to stabilise the nanoindentation measurements of open-porous copper materials. It should be mentioned, that for open-porous structures a residual

roughness, even if infiltrated, will always affect the measurement. However if the indentation depth of the infiltrated samples is beneath their core roughness, Sk, all nanoindentation measurements of the infiltrated samples will be as congruent, as it can be observed for the infiltrated sample J5.

Table 20; Comparison of composite J5 and as produced open-porous J5 SK to confirm the stabilisation effects of infiltration. The deviation values of the composite J5 are outstanding. For the J5 SK sample the Young's modulus is beneath the threshold and therefore valid. But the Hardness covariance is way too high. Similar behaviour has been observed for all samples without infiltration. To finally compare the values of the composite with the values of the open-porous material, the values of pure epoxy resin need to be subtracted.

		Red. Modulus	Modulus	Hardness	Drift Corr.	Temperature
		GPa	GPa	GPa	nm/s	°C
J5	Mean	**32**	**29.8**	**1.02**	-0.03	26.6
	Std. Dev.	0.5	0.5	0.02	0.01	
	% COV	**1.49**	**1.53**	**1.75**	-33.62	
J5 SK	Mean	**22.7**	**20.8**	**0.51**	-0.023	27.3
	Std. Dev.	1.3	1.3	0.09	0.008	
	% COV	**5.95**	**6.07**	**18.08**	-36.22	

4.4. Mechanical models of open-porous Cu and Cu-composite

4.4.1. Ashby-Gibson model for porous materials

A first attempt in Phase 1 was to connect porosity and Young's modulus through the well-established Ashby-Gibson model (APPENDIX A). The aim was to calculated the porosity for the measured reduced Young's modulus values of the surface preparation samples and see if those would be congruent with the gravimetric determined porosity value of J2.

That is illustrated in Figure 43. The porosity determined through gravimetric by the company for J1/J2 was 30 % (Table 17). To give an impression where the desired values are heading a point was inserted in the diagram. Marked by a green star a point was inserted. This point possesses the gravimetric porosity of J2 and the determined Young's modulus for J2 listed in Table 22. As can be seen in Figure 43, the values of the different surface preparations scatter along the graph and none of them are really near the expected porosity of 30%. Through ion milling (violet star) the access to the pore system is increased, which leads to severe roughness effects and low Youngs's modulus values. The fine grinding (red triangle) altered the surface material severely, the porosity has been diminished through material deformation, as a result the Young's modulus values have been higher than with all the other preparation techniques. Finally, the OP-S values are at a similar modulus level than the final determined Young's modulus values, but the porosity is still not near the given 30%.

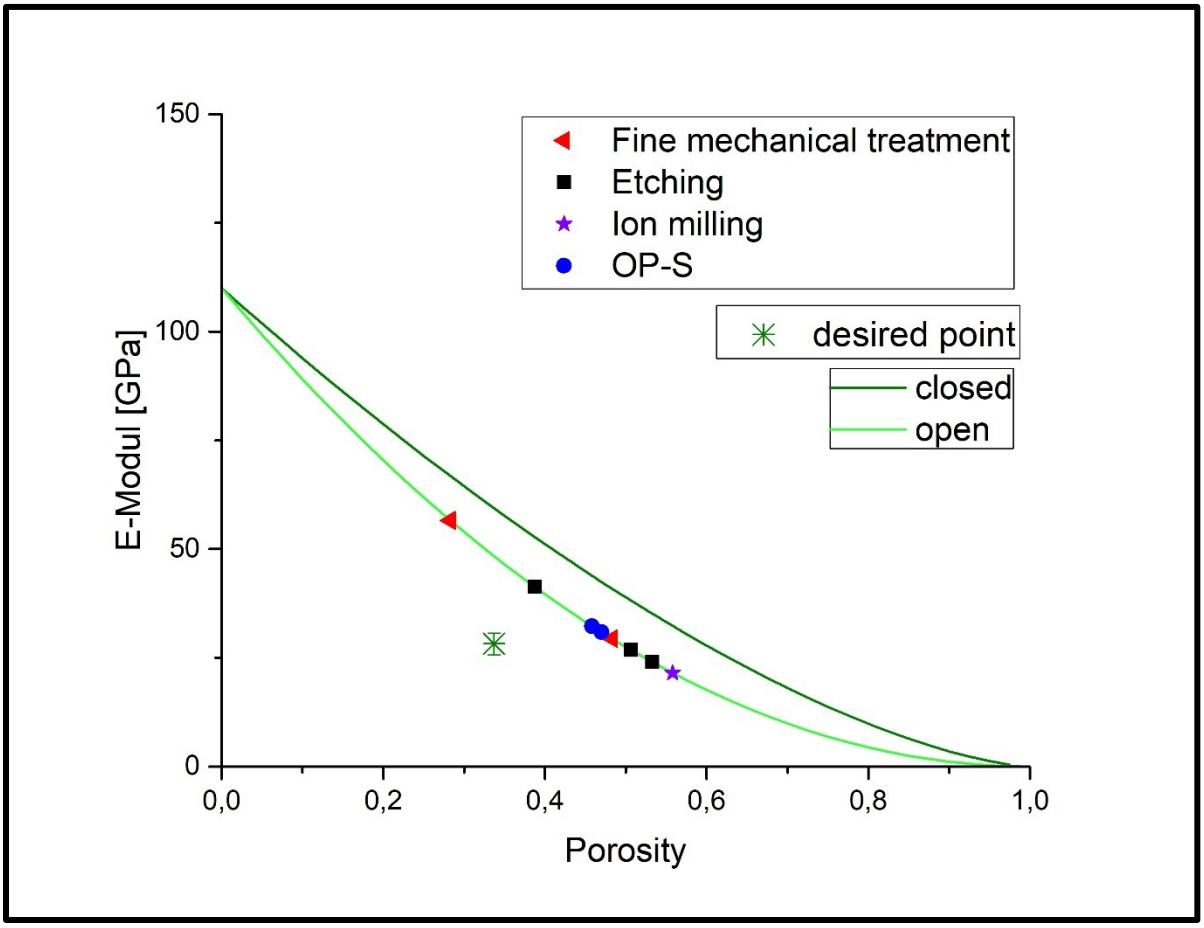

Figure 43; Illustration of the calculated values of the Ashby-Gibson model on open and closed cell structure. Additional the values from the surface preparation test (Table 13 and

Table 14) have been included into that model of open cell structure. As comparison, the J2 value from Phase 2 have been included to give an estimation, where the porosity might really be.

The exact calculated porosity values can be seen in Table 21. The porosity was calculated trough the Ashby-Gibson model for open-porous cell structures. The values scatter from 28 to 56 % porosity. Both boundary values are not reasonable due to severe material alteration (affected surface or high roughness). The OP-S modulus values are in the range, but the porosity cannot be reached, because it has to follow the Ashby-Gibson model for open-cell structure.

As a result, it is clear from the graph and calculation, that the Ashby-Gibson model for open-porous material is not congruent with the determined values of porosity and Young's modulus of this thesis. The Ashby Gibson model for open-cell structure overestimates the porosity values of the material. This agrees with data from different papers [1 ,12, 19], where it was stated that for sintered porous material the Ashby-Gibson model for open-cell structures is not useable.

Table 21; Calculated Porosity of the measured Young's modulus values of Phase 1 surface preparation samples. The values have been calculated regarding the Ashby-Gibson model for open-porous cell structure. The expected value was 30%, therefore no reasonable match between Ashby-Gibson and the open-porous sintered copper material could be found. For better orientation the values of J1 have been highlighted.

Preparation technique	Sample	Measured E*- Modulus [GPa]	calculated Porosity [%]
OP-S	J1	30.90	47.00
OP-S	J2	32.30	45.81
Fine grinding	J1	56.60	28.27
Fine grinding	J2	29.40	48.30
Etching	J1	41.30	38.73
Etching	J2 (top side)	24.00	53.29
Etching	J2 (bottom side)	26.80	50.64
Ion milling	J1	21.50	55.79

4.4.2. Advanced models for infiltrated materials

In Phase 2 the step toward infiltration was taken to minimise the influence of roughness, pore shape and obscured material properties of air on Hardness and Young's modulus. In a composite, the mechanical properties of copper become add up with the properties of epoxy resin. The aim was to find a proper behaviour model for the mechanical properties of the copper material, to make predictions on porosity and mechanical behaviour. Different models have been calculated (APPENDIX B). The measured values of the samples J2, J3, J4 and J5 (Table 19) have been inserted into the graph, firstly with the porosity values determined from the simple 2D analysis based on the coloured images, second the porosity values of the sophisticate 3D SEM/FIB Tomography and finally the through gravimetry determined porosity values, all data sets are taken from Table 17. This was done to see how the different models correlate with the values, to decide which model work at best.

For composite the maximum mechanical properties are reached through a unidirectional material structure, as given by the Voigt (ε = constant) and the Reuss model (σ = constant). Both models are used together to define the range of possible mechanical values, as can be seen in Figure 44 (compact lines). All the values are inside the range of validity. Therefore, further models have been investigated to see if one of these can be used as trendline for the material behaviour or minimise the range of validity for the possible material properties, like the Hashin-Shtrikman (HS) model, followed by the Mori-Tanaka (MT) model and finally the Self-consistency (SC) model. The models for this thesis have been chosen based on the dissertation of A. Kraatz [24]. The Self-consistency model was disqualified, because it was too complex. The MT model (dotted line) in cooperates the Poisson's ratio, but it is similar to the Reuss model. As a result, this model would only make sense, if the material behaviour follows the model. Then it could be used as trendline, but this has not been the case. At least, only the Hashin-Shtrikman (HS) model

(dashed line) brought a useful narrowed range of validity. All measured values of J_2, J_3, J_4 and J_5 are inside this range, but some are more reasonable than others. The 2D and 3D analysis values are alike, except the value for J_4. Those two analyses showed regarding the nanoindentation values and structure reasonable values, whereas the gravimetric values are inside the model, but are not reasonable regarding the nanoindentation values and structures. As a result, the HS model seems to be sufficient for the 2D analysis of the porous copper and gives an information of the material behaviour, because all values are settled inside in between the limits and are more or less set near the midst.

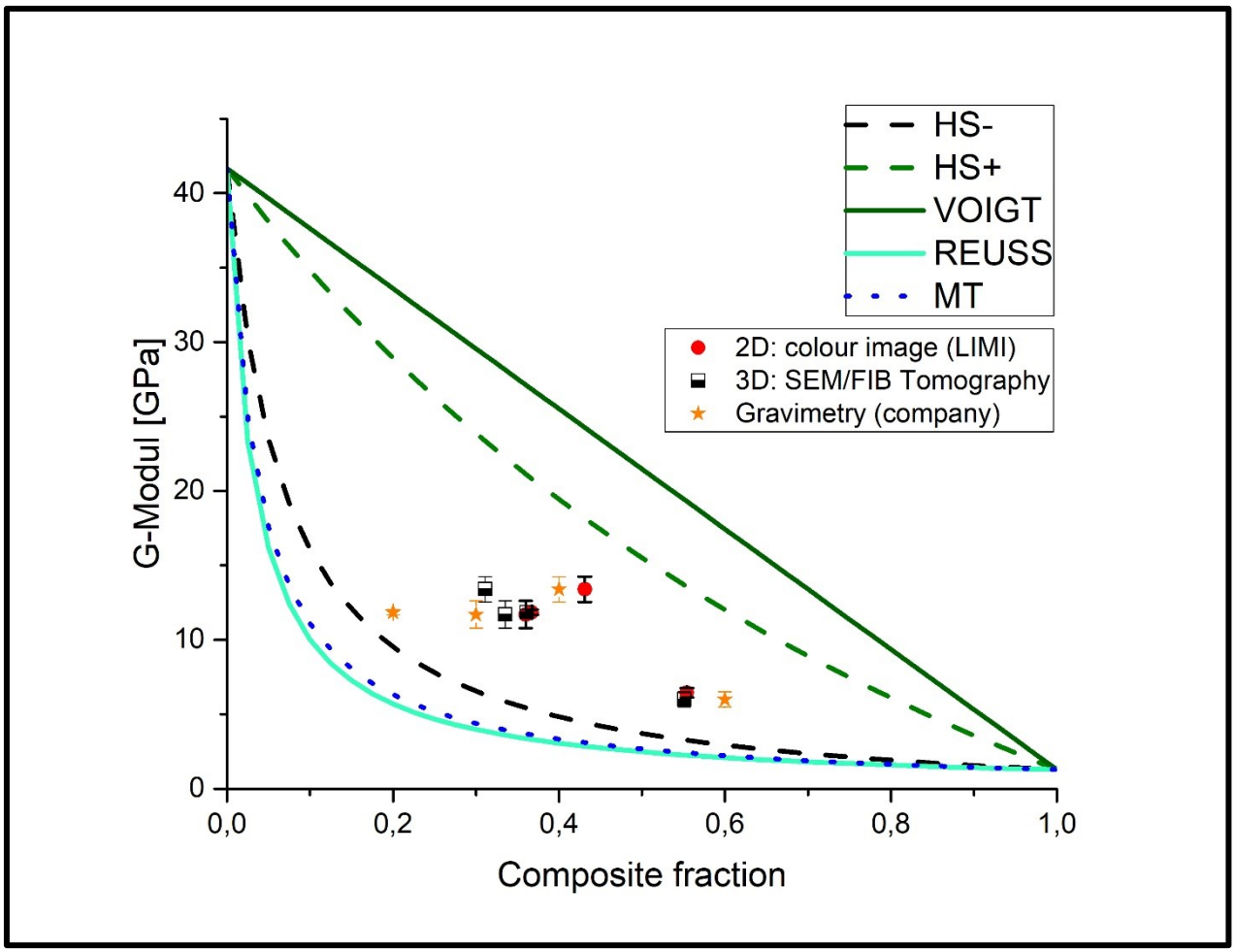

Figure 44; Advanced models (Reuss, Voigt, upper (HS+) and lower (HS-)Hashin-Shtrikman limits and Mori-Tanaka (MT)) and values with their porosity measured with the different methods, all listed together in one diagram to illustrate the scattering of the possible porosities.

Consequently, no model could be found to be used as a trendline for the material behaviour for the newly developed open-porous copper material, but a model can be given which narrows down the range of validity for values of the moduli, the Hashin-Shtrikman model for coated spheres. Nevertheless, the porosity measurement influences the position of the values considerably, therefore additional research on the 3D structure of the material are recommended for following pursuits.

5. DISCUSSION

5.1. Material structure and porosity

Material structure: After intensive investigation of the material, it can be assumed, that the difference in the sample structure and appearance is mainly based on different pastes and production parameters. The paste shift explains the similarities between materials with the same paste like J1, J2 and J4 and a different structure for J3 and J5.

J2 and J4 have been produced with the same paste material (Paste J1) and can be described as heterogenic. Next to the preferred nanoscale particles and pores, still some larger compact particles are seen. The roughness parameters show a similar surface behaviour (Table 15 and Table 16). Nevertheless, the maximum pore and grain sizes decrease from J2 to J4, which is confirmed by the Abbott-curve, skweness and kurtosis (Figure 27 a) and c), Table 15). The extreme difference of the the core roughness Sk indicates that in use the material has still tremendous roughness. After a look at the images, those might be, because of its pore shapes. While the pores of J1 and J2 have a very high length-width ratio and peak to peak distance, the length-width ratio for J4 is close to 1 (round shape). This indicates, that J1 and J2 surfaces might be subjected to higher deformation, especially around their pores. J3 and J5 can be described as homogeneous, where all particles and pores seem to be in a similar range. The size decreases from J3 to J5 as well as the roughness parameters (Table 15 and Table 16). J5 shows the best values of the investigated samples. The high kurtosis value of J5 is an additional indication of extremely fine particles, which leads to small points on the surface. Whereas the kurtosis of J3 indicate more semi-circular shapes. The roughness of all the samples can be traced back to their particle and pore sizes (Figure 28). In case of J1 and J2 the large round particles lead to semicircle roughness tips. For J3 the particles are significantly smaller and the roughness diminishes as well. In J4 the particle maximum is larger than J3, but also particles smaller than J3 appear, especially on the surface. In total, the geometry of J4 particles is more elongated and lead to a more pointed surface. J5 consists of fine particle structure, which leads to an arithmetic mean roughness Sa of 120 nm, a respectable value for an open porous material. All the structural analysis tools confirm the findings observed by the other tools.

Porosity: From the nanoindentation behaviour's point of view the gravimetric porosity values have a large error. Therefore, additional analysis for verification of the porosity have been needed. The values from nanoindentation as given are, J2 with an E^*=29.2± 2.4 GPa, J3 possesses an E^*=17.0± 0.6 GPa, followed by J4with an E^*= 33.8± 2.2 GPa and finally J5 with an E^*=29.8±0.5 GPa. That would predict the

following relative ratio: J2 should be somewhere around the porosity level of J5, due to the high deviation of J2. Whereas J4 is settled on a lower porosity level, but still near the lower limit of J2. J3 is around half the value of J4, which means that the porosity is around double the value of J2. A quick listing from the lowest porosity to highest would be J4< (J2, J5)< J3. With the given gravimetric values of 30 (J2), 60 (J3), 40 (J4) and 20 (J5) percent, the prediction could not have been valid. Therefore, further analysis methods have been tried. Here the value of J2 rose and settled between 30 and 38%, whereas the porosity of J3 decreased. The prediction with double the value could no longer be made, but linked to the exponential decay of most of the prediction models (e.g. Figure 44), this could be reasonable. The porosity is then settled around 44 to 56%. J4 was predicted to have a lower porosity, but the 2D analysis methods settled the value at the same or a higher porosity level (36 to 55%). For this structure, it was difficult to determine the porosity.Only the advanced method of 3D SEM/FIB Tomography was able to set the porosity to the expected range (~30%). The former lowest porosity sample J5 rose to porosity levels between 36 and 50%. This illustrates the uncertainty of an accurate porosity prediction. In this work, the 2D: coloured images ROI analysis was similar to the predicted porosity (J2, J3, J5) and some values are near the through SEM/FIB Tomography analysis method determined values (J2, J5, J3), a more sophisticated 3D method (Table 17 and Figure 44).

5.2. Modified Ashby-Gibson model

The Ashby-Gibson model has been calculated for open- and closed-cell porous copper, but the model was not coherent with the measured values for Young's modulus and porosity, as could be seen in Figure 43. This supports the topic of discrepancy between the Ashby-Gibson model for open-cell structure and sintered products published in different papers [1, 19]. In the paper of S.O. Kuchevey et al. [32] it is mentioned that low density nanoporous solids decrease with a higher exponent than the one given for open-cell structure (q=2). This is caused by the fact, that M. Ashby and L. Gibson mainly researched foams with porosity of 70% and higher, for material with those porosity values the model fits quite well. But for low-density sintered material with a porosity <70% Kuchevey predict the exponent q to be between 3 and 4. This would cause a modification like in Figure 45, where the calculated AG-model for sintered material has been illustrated (values at APPENDIX A).

To implement the values in the diagram, the "pure" copper values need to be calculated from the determined composite values. This is done by subtracting the epoxy value from Table 3 from the nanoindentation values given in Table 19. The results for the Young's modulus can be seen in Table 22.

Table 22; Through nanoindentation measured material properties on infiltrated samples J2, J3, J4 and J5and their "pure" copper values calculated through a simple subtraction of the Youngs's modulus of epoxy resin from the measured values.

Red. Modulus	J2 [GPa]	J3 [GPa]	J4 [GPa]	J5 [GPa]
Composite	29.2±v2.4	17.0± 0.6	33.8± 2.2	29.8± 0.5
Copper	25. 75± 2.4	13.55± 0.6	30.35± 2.2	26.35± 0.5

It can be seen that the porosity determined through the simple 2D analysis on coloured images would just fit the model, like J2 and J5, also J3 but only through its deviation range. But the value for J4 is far away from the predicted range for sintered materials (Figure 45, red dots). Whereas the values determined through the sophisticated analysis method done by the dissertation of A. Wijaya [23] (black and white boxes) are a match for the for the samples J2, J4 and J5. The sample J3 is only reaching the limits with its deviation range. Concluding, it can be said that with a sophisticated porosity measurement (SEM/FIB Tomography, etc.) and the modified Ashby-Gibson model a guideline for the open-porous copper material can be given. But further investigations are needed to consolidate the use of the modified exponents 3 and 4.

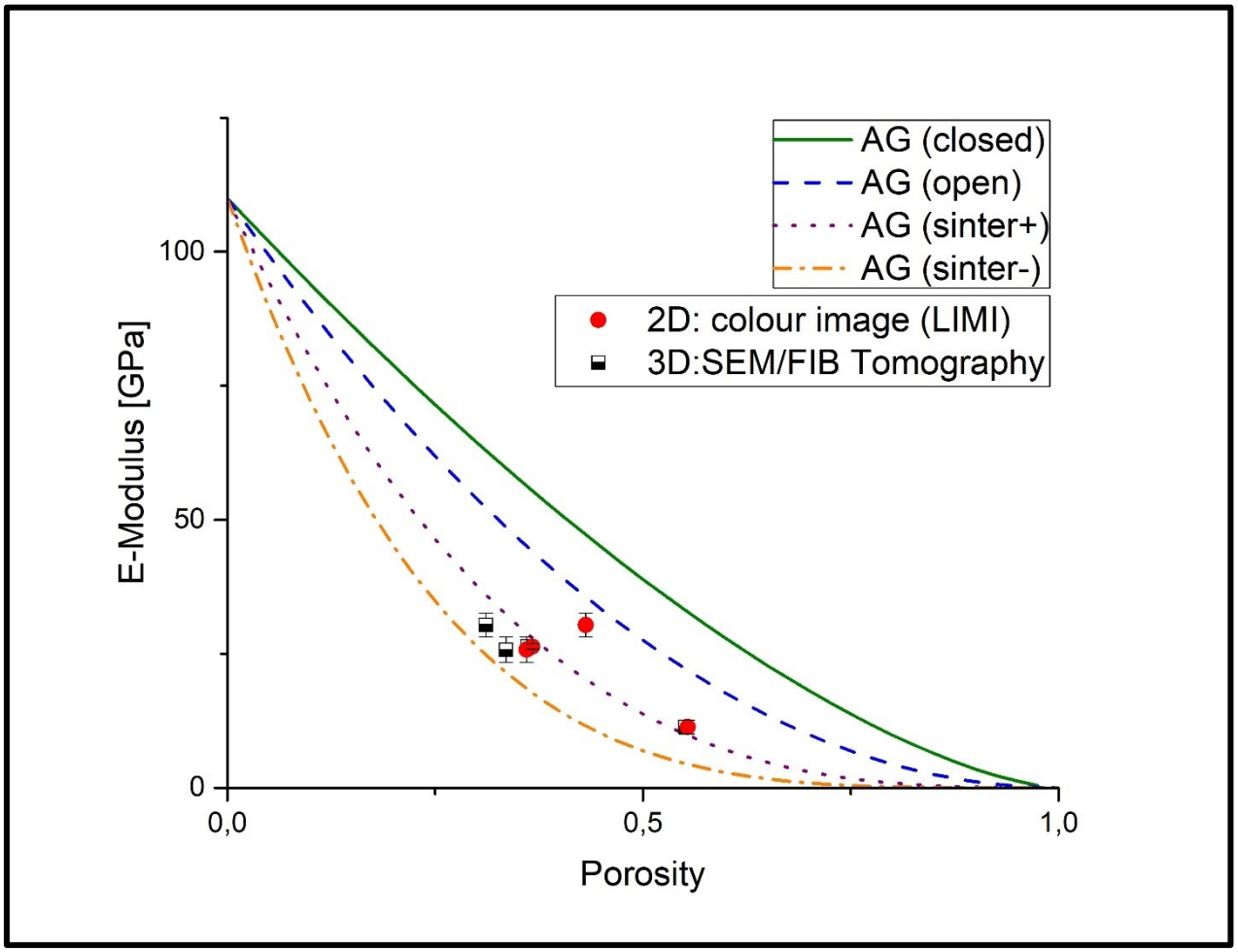

Figure 45; Modified Ashby-Gibson for sintered porous material with a predicted exponent between 3 (sintered +) and 4 (sintered-). Those upper and lower limits would include the measured values with the porosity values determined through the sophisticated method, whereas the 2D analysis shows here some misfit for J4. This illustrates the necessity of an exact porosity determination.

5.3. Final advanced model for the infiltrated samples

For the infiltrates the prediction model of Hashin-Shtrikman have been chosen, due to narrowing down the range of validity for the moduli. Into the model the 2D porosity analysis on coloured images have been more included additional to the sophisticated methods for the porosity analysis. The final model and porosity can be seen in Figure 46.

The advantage of the HS model is, that an upper and a lower limit can be given and in between those limits a prediction on the material composition can be made. While, the ratio between matrix radius and the radius of the inhomogeneity is constant, the composition of the matrix and the inhomogeneity is variable. The values are mainly settled in the middle of the HS limits, which seems reasonable due to the composition of the matrix and inhomogeneities in this area. In the middle of the two limits the model predicts that the matrix and inhomogeneity both are made out of 50% copper and 50% epoxy resin. This resembles the sponge material structure more than the structure of the limits itself, because for a sintered copper sponge the particles need to be in contact with each other. This would only be possible if the inhomogeneity and the matrix both include copper.

The Young's modulus of 2D analysed J5 and J2 as well as the 3D analysed J2 value are very similar, as can be seen in Figure 46. The 2D analysed J4 value is the only sample set on the upper half of the HS range of validity. Here the porosity determination should be done with more sophisticated methods, because the measured porosities for J4 are set between (30% and 55%). J3 is plausible closer to the lower limit of the HS-model, because of the structure of the material as seen in Figure 28 b) Through the higher ratio of epoxy resin and the homogeneous round copper particles a higher resemblance of the ideal HS model than the fine sponge structure of the other samples can be observed.

Based on the dissertation of A. Kraatz [24], the self-consistency method would have been predicted near the middle of the two HS limits and therefore might be very interesting to investigate, which could not been done due to necessary complex calculations. In conclusion, the HS limits and its centre line can be used as a guideline. Further research is recommended for more sophisticated models like the self-consistency model.

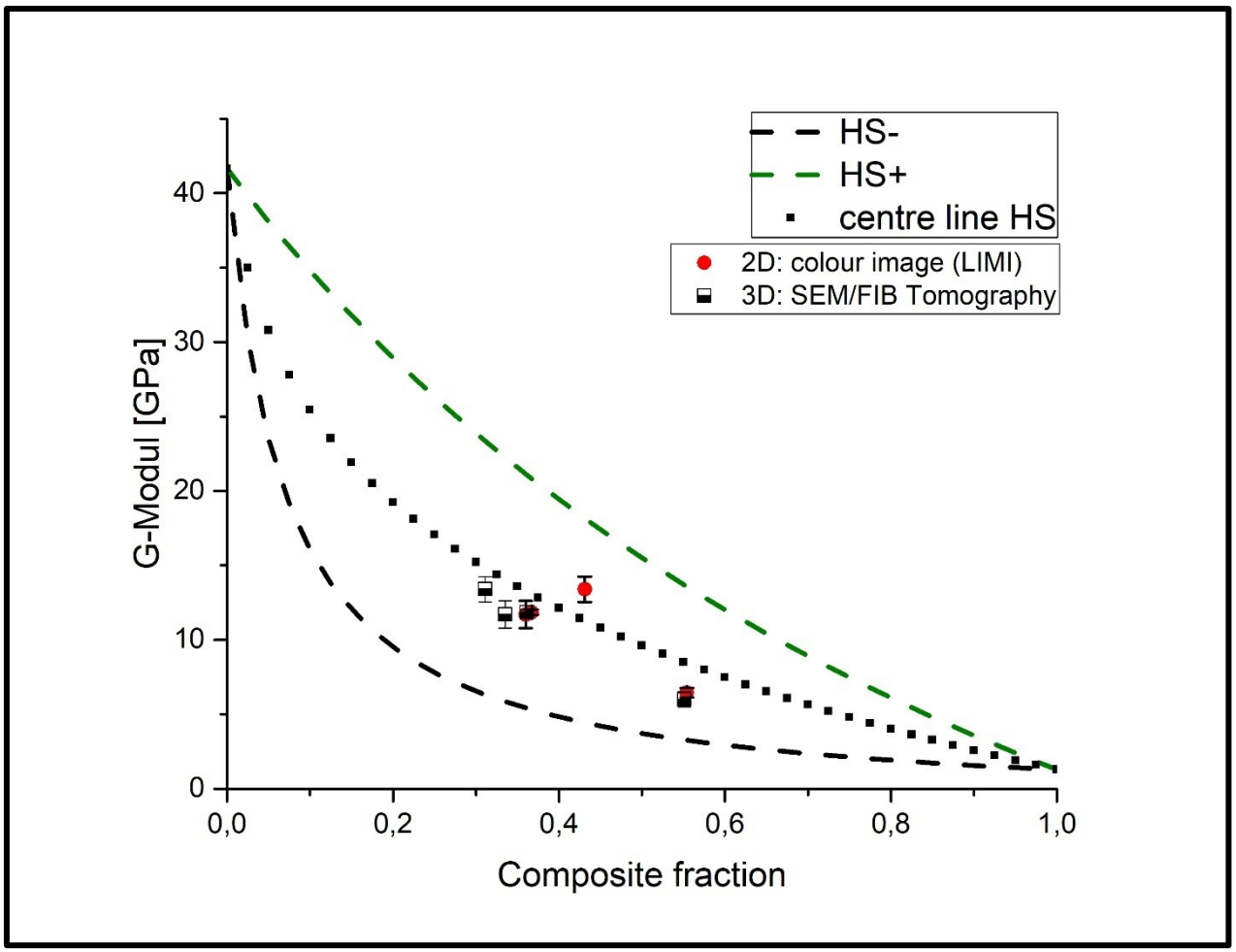

Figure 46; HS-model with an additional centre line. At the centre line the model structure resembles the fine sponge structure the most. The porosity values evaluated through 2D analysis on colour images are used and they are mostly set near the centre line. The value of J4 in the upper half of the HS-model is a clear indication of a wrong porosity determination. More sophisticated analysis methods for the porosity determination like SEM/FIB Tomography are recommended.

6. CONCLUSION

The task for this thesis was to investigate the structure and material influence of open-porous copper samples on nanoindentation measurements.

In conclusion, **infiltration is a useful method to stabilise nanoindentation experiments on materials like open-porous copper layers**. All values measured on the infiltrated samples are below a covariance of 10% and therefore they are valid (Table 19 and the pure copper values listed in Table 22). Infiltration annihilates the influence of the unknown Poisson's ratio of air and guarantees the necessary building of a homeostatic core beneath the indenter tip [50].

Furthermore, under reservations it can be concluded, that a material behaviour prediction for open-porous copper layers can either be made through a **modified Ashby-Gibson model** (Figure 45) or the **Hashin-Shtrikman model** (Figure 46).

For further investigations regarding the indentation behaviour, it can be said, that because of the open-porosity the residual roughness will always affect the top surface of the samples, infiltrated or not. But the residual roughness can be estimated through the functional roughness parameter, core roughness Sk given in Table 16. In case of J5 the best results could be provided, maybe because the indentation depth was deeper than Sk of this sample. Because the values stabilised after passing the values of Sk (Figure 42). It might be interesting to repeat the nanoindentations for the other samples with indentation depth beneath their core roughness values, according to Table 16. To make this possible for all samples listed in this thesis, the sample thickness has to be raised, to a minimum of 40 µm.

Huge discrepancies of the porosity occur due to the material structure and porosity determination. Here further investigations, regarding 3D material structural response through SEM/FIB- and X-ray computed tomography and EBSD are necessary to sufficiently understand the material, its structure and the different models.

BIBLIOGRAPHY

[1] C. Wen, Y. Yamada, K. Shimojima, and Y. Chino, "Processing and mechanical properties of autogenous titanium implant materials," *J. Mater.*, vol. 13, pp. 397–401, 2002.

[2] L. Hou, L. Li, and Y. Zheng, "Fabrication and Characterization of porous sintered Ti-Ag Compacts for Biomedical Application Purpose," *J. Mater. Sci. &Technology*, vol. 29, pp. 330–338, 2013.

[3] S. Hardt, W. Ehrfeld, V. Hessel, and K. M. Vanden Bussche, "Strategies for size reduction of microreactors by heat transfer enhancement effects," *Chem. Eng. Commun.*, vol. 190, no. 4, pp. 540–559, 2003.

[4] J. Biener *et al.*, "Surface-chemistry-driven actuation in nanoporous gold," *Nat. Mater.*, vol. 8, no. 1, pp. 47–51, 2009.

[5] J. Banhart, "Manufacture , characterisation and application of cellular metals and metal foams," vol. 46, pp. 559–632, 2001.

[6] L. J. Gibson and M. F. Ashby, *Cellular solids Structure and properties*, Second. Cambridge: The Press syndicate of the university of cambridge, 1997.

[7] S. Bigl, T. Schöberl, S. Wurster, M. J. Cordill, and D. Kiener, "Correlative microstructure and topography informed nanoindentation of copper films," *Surf. Coatings Technol.*, vol. 308, pp. 404–413, 2016.

[8] M. Laurent-Brocq, E. Béjanin, and Y. Champion, "Influence of roughness and tilt on nanoindentation measurements: A quantitative model," *Scanning*, vol. 37, no. 5, pp. 350–360, 2015.

[9] V. Madhavan and M. S. Kashani, "Analysis and correction of the effect of sample tilt on results of nanoindentation," *Acta Mater.*, vol. 59, pp. 883–895, 2011.

[10] C. Walter, T. Antretter, R. Daniel, and C. Mitterer, "Finite element simulation of the effect of surface roughness on nanoindentation of thin films with spherical indenters," *Surf. Coatings Technol.*, vol. 202, no. 4–7, pp. 1103–1107, 2007.

[11] L. Chen, A. Ahadi, J. Zhou, and J.-E. Stahl, "Modeling effect of surface roughness on nanoindtation tests," *Procedia CIRP*, vol. 8, pp. 334–339, 2013.

[12] B. Wang and E. Zhang, "On the compressive behavior of sintered porous coppers with low-to-medium porosities-Part II: Preparation and microstructure," *Int. J. Mech. Sci.*, vol. 50, no. 3, pp. 550–558, 2008.

[13] B. Schulz, "Thermal conductivity of porous and higly propus materials," *High Temp. Press.*, vol. 13, pp. 649–660, 1981.

[14] H. Park, C. Ahn, H. Jo, and M. Choi, "Large-area metal foams with highly ordered sub-micrometer-scale pores for potential applications in energy areas," *Mater. Lett.*, vol. 129, pp. 174–177, 2014.

[15] B. K. Park, D. Kim, S. Jeong, J. Moon, and J. S. Kim, "Direct writing of copper conductive patterns by ink-jet printing," *Thin Solid Films*, vol. 515, no. 19 SPEC. ISS., pp. 7706–7711, 2007.

[16] X. Wang, J. Liu, Y. Wang, and Y. Fu, "Fabrication of friction-reducing texture surface by selective laser melting of ink-printed (SLM-IP) copper (Cu) nanoparticles(NPs)," *Appl. Surf. Sci.*, vol. 396, pp. 659–664, 2017.

[17] H. Nakajima, S. . Hyun, K. Ohashi, K. Ota, and K. Murakami, "Fabrication of porous copper by unidirectional solidification under hydrogen and its properties," *Colloids Surfaces A Physicochem. Eng. Asp.*, vol. 179, no. 2–3, pp. 209–214, 2001.

[18] R. Kay and M. Desmulliez, "A review of stencil printing for microelectronic packaging," *Solder. Surf. Mt. Technol.*, vol. 24, no. 1, pp. 38–50, 2012.

[19] B. Wang and E. Zhang, "On the compression behaviour of sintered porous coppers with low medium porosities-Part I:Experimental study," *Int. J. Mech. Sci.*, vol. 47, pp. 744–756, 2005.

[20] "Kupfer." [Online]. Available: www.chemie.de/lexicon/Kupfer html. [Accessed: 20-Apr-2017].

[21] H. Oettel and H. Schumann, *Metallografie- Mit einer Einführung in die Keramografie*, 15. Auflag. Weinheim: WILEY-VCH GmbH & Co. KGaA, 2011.

[22] S. M. Sze and M.-K. Lee, *Semiconductor Devices - Physics and Technology*, Third Edit. John Wiley & Sons Inc., 2012.

[23] A. Wijaya, "Development of an Advanced Characterisation - Toolbox for Porous Copper Layers (effective 15-September-2017)," MU Leoben (unpublished), 2020.

[24] A. Kraatz, "Anwendung der Invariantentheorie zur Berechnung des dreidimensionalen Versagens- und Kriechverhaltens von geschlossenzelligen Schaumstoffen unter Einbeziehung der Mikrostruktur," Martin-Luther-Universität Halle-Wittenberg, 2007.

[25] D. Gross and S. Thomas, *Bruchmechanik*, 5. Auflage. Heidelberg: Springer Verlag, 2011.

[26] Z. Hashin, "Analysis of Composite Materials - A Survey," *J. Appl. Mech.*, vol. 50, pp. 481–505, 1983.

[27] R. M. Christensen, *Mechanics of Composite Materials*. New York: Wiley & Sons, 1980.

[28] "HS-model." [Online]. Available: http://silver.neep.wisc.edu/~lakes/MSE541.dir/CoatedSpher.gif. [Accessed: 12-Jan-2017].

[29] P. K. Sinha, "Chapert 4: Composite properties - Micromechanics," in *Composite materials and structures*, Kharagpur: Composte Centre of Excellence, AR &DB Department of Aerospace Engineering, 2006.

[30] V. Maier, A. Hohenwarter, R. Pippan, and D. Kiener, "ScienceDirect Thermally activated deformation processes in body-centered cubic Cr – How microstructure influences strain-rate sensitivity," *Scr. Mater.*, no. May, pp. 1–4, 2015.

[31] J. Hay, P. Agee, and E. Herbert, "Continuous stiffness measurement during instrumented indentation testing," *Exp. Tech.*, pp. 86–94, 2010.

[32] S. O. Kucheyev, A. V. Hamza, J. H. J. Satcher, and M. A. Worsley, "Depth-sensing indentation of low-density brittle nanoporous solids," *Acta Mater.*, vol. 57, pp. 3472–3480, 2009.

[33] W. Oliver and J. Pethica, "Method for Continuous Determination of the Elastic Stiffness of Contact Between Two Bodies," US4848141 A, 1989.

[34] W. Oliver and G. Pharr, "An Improved Technique for Determining Hardness and Elastic Modulus using load and Displacement Sensing Indentation Experiments," *J. Mater. Res.*, vol. 7, pp. 1564–1583, 1992.

[35] Y. Xia, M. Bigerelle, J. Marteau, P.-E. Mazeran, S. Bouvier, and A. Iost, "Effect of Surface Roughness in the Determination of the Mechanical Properties of Material Using Nanoindentation Test," *Scanning*, vol. 9999, pp. 1–16, 2013.

[36] J.Hay, "Introduction to instrumented indentation testing," *Exp. Tech. Featur. Nanomechanical Charact. Mater. by nanoindentation Ser.*, vol. November/D, 2009.

[37] *DIN EN ISO 25178-2*. 2013.

[38] C. Wiehr and J. Seewig, "3D Kennwerte nach ISO 25178," 2014. [Online]. Available: http://ak-rauheit.de/files/3D Kenngr%F6%DFen.pdf. [Accessed: 25-Aug-2017].

[39] H. Sorg, *Praxis der Rauheitsmessung und Oberflächenbeurteilung*. München: Carl Hansen Verlag, 1995.

[40] KEYENCE-Corporation, "3D Surface parameters," 2017. [Online]. Available: http://www.keyence.com/ss/products/microscope/roughness/surface/parameters.jsp. [Accessed: 25-Aug-2017].

[41] OLYMPUS-ims, "3D Surface Parameters," 2017. [Online]. Available: http://www.olympus-ims.com/de/knowledge/metrology/roughness/3d_parameter/. [Accessed: 20-May-2017].

[42] V. Liedtke and Y. Hruvy, "Verbundwerkstoffe und Verfahren zu dessen Herstellung," EN1457472 A1, 2004.

[43] Mikroskopie-Forum, "Dünnflüßiges Epoxid zum Infiltrieren in Gewebeporen." [Online]. Available: http://www.mikroskopie-forum.de/index.php?topic=2476.0. [Accessed: 02-Mar-2017].

[44] F. H. Gojny, "SCIENCE AND Carbon nanotube-reinforced epoxy-composites : enhanced stiffness and fracture toughness at low nanotube content," vol. 64, pp. 2363–2371, 2004.

[45] F. H. Gojny, M. H. G. Wichmann, B. Fiedler, and K. Schulte, "SCIENCE AND Influence of different carbon nanotubes on the mechanical properties of epoxy matrix composites – A comparative study," vol. 65, pp. 2300–2313, 2005.

[46] K. Wang, A. Kobler, C. Kübel, H. Jelitto, G. Schneider, and J. Weissmüller, "Nanoporous-gold-based composites: toward tensile ductility," *NPG Asia Mater.*, vol. 7, no. 6, p. e187, 2015.

[47] OLYMPUS-ims, "Olympus LEXT." [Online]. Available: http://www.olympus-ims.com/de/metrology/ols4100/. [Accessed: 22-May-2017].

[48] OLYMPUS -ims, "Olympus STREAM." [Online]. Available: http://www.olympus-ims.com/de/microscope/stream2/. [Accessed: 22-May-2017].

[49] L. Zheng, A. W. Schmid, and J. C. Lambropoulos, "Surface effects on Young ' s modulus and hardness of fused silica by nanoindentation study," *J. Mater Sci.*, vol. 42, pp. 191–198, 2007.

[50] A. C. Fisher-Cripps, *The Handbook of Nanoindentation*, no. 1. 2005.

[51] W.-G. Jiang, J.-J. Su, and X.-Q. Feng, "Effect of surface roughness on nanoindentation test on thin films," *Eng. Fract. Mech.*, vol. 75, pp. 4965–4972, 2008.

APPENDIX

A. Values for Ashby-Gibson closed-, open-cell structure and sintered powder

$$E^* = C_2 * E_s * \left(\frac{\rho^*}{\rho_S}\right)^q$$

Porosity []	Young's modulus E^* [GPa] of the Cell-structure			
	Closed-cell structure q = 1.5	Open-cell structure q = 2	Sintered-powder upper limit q = 3	Sintered-powder lower limit q = 4
0	110.00	110.00	110.00	110.00
0.025	105.90	104.57	101.95	99.41
0.05	101.85	99.28	94.31	89.60
0.075	97.86	94.12	87.06	80.53
0.1	93.92	89.10	80.19	72.17
0.125	90.03	84.22	73.69	64.48
0.15	86.20	79.48	67.55	57.42
0.175	82.43	74.87	61.77	50.96
0.2	78.71	70.40	56.32	45.06
0.225	75.05	66.07	51.20	39.68
0.25	71.45	61.88	46.41	34.80
0.275	67.91	57.82	41.92	30.39
0.3	64.42	53.90	37.73	26.41
0.325	61.00	50.12	33.83	22.84
0.35	57.65	46.48	30.21	19.64
0.375	54.35	42.97	26.86	16.78
0.4	51.12	39.60	23.76	14.26
0.425	47.96	36.37	20.91	12.02
0.45	44.87	33.28	18.30	10.07
0.475	41.84	30.32	15.92	8.36
0.5	38.89	27.50	13.75	6.87
0.525	36.01	24.82	11.79	5.60
0.55	33.21	22.28	10.02	4.51
0.575	30.48	19.87	8.44	3.59
0.6	27.83	17.60	7.04	2.82
0.625	25.26	15.47	5.80	2.18
0.65	22.78	13.48	4.72	1.65
0.675	20.38	11.62	3.78	1.23
0.7	18.08	9.90	2.97	0.89
0.725	15.86	8.32	2.29	0.63

0.75	13.75	6.88	1.72	0.43
0.775	1174	5.57	1.25	0.28
0.8	9.84	4.40	0.88	0.18
0.825	8.05	3.37	0.59	0.10
0.85	6.39	2.48	0.37	0.06
0.875	4.86	1.72	0.21	0.03
0.9	3.48	1.10	0.11	0.01
0.925	2.26	0.62	0.05	0.00
0.95	1.23	0.28	0.01	0.00
0.975	0.44	0.07	0.00	0.00
1	0.00	0.00	0.00	0.00

B. Values for Advanced models – Voigt, Reuss, Hashin-Shtrickman, Mori-Tanaka

Porosity []	**Shear modulus G [GPa]**				
	Voigt	Reuss	HS-	HS+	MT
0	41.67	41.67	41.67	41.67	41.67
0.025	40.66	23.29	30.15	39.85	24.78
0.05	39.65	16.16	23.48	38.10	17.59
0.075	38.64	12.38	19.13	36.43	13.62
0.1	37.63	10.03	16.08	34.82	11.09
0.125	36.62	8.43	13.81	33.27	9.35
0.15	35.61	7.27	12.06	31.77	8.07
0.175	34.60	6.39	10.67	30.33	7.09
0.2	33.59	5.70	9.54	28.95	6.32
0.225	32.58	5.14	8.60	27.61	5.70
0.25	31.57	4.69	7.81	26.32	5.18
0.275	30.56	4.31	7.13	25.07	4.75
0.3	29.55	3.98	6.55	23.87	4.38
0.325	28.54	3.70	6.03	22.70	4.07
0.35	27.53	3.46	5.59	21.57	3.79
0.375	26.52	3.25	5.19	20.48	3.55
0.4	25.51	3.06	4.83	19.42	3.33
0.425	24.50	2.89	4.51	18.40	3.14
0.45	23.49	2.74	4.22	17.41	2.97
0.475	22.48	2.61	3.96	16.44	2.81
0.5	21.47	2.48	3.72	15.51	2.67
0.525	20.46	2.37	3.50	14.60	2.54
0.55	19.45	2.27	3.30	13.72	2.43
0.575	18.44	2.18	3.11	12.86	2.32

0.6	**17.43**	**2.09**	**2.94**	**12.03**	**2.22**
0.625	16.43	2.01	2.78	11.22	2.13
0.65	15.42	1.94	2.63	10.43	2.04
0.675	14.41	1.87	2.49	9.66	1.96
0.7	13.40	1.80	2.36	8.91	1.89
0.725	12.39	1.75	2.24	8.19	1.82
0.75	11.38	1.69	2.13	7.48	1.75
0.775	10.37	1.64	2.02	6.79	1.69
0.8	9.36	1.59	1.92	6.11	1.64
0.825	8.35	1.54	1.82	5.46	1.58
0.85	7.34	1.50	1.73	4.82	1.53
0.875	6.33	1.46	1.65	4.19	1.48
0.9	5.32	1.42	1.57	3.58	1.44
0.925	4.31	1.38	1.49	2.99	1.40
0.95	3.30	1.35	1.42	2.40	1.36
0.975	2.29	1.31	1.35	1.84	1.32
1	1.28	1.28	1.28	1.28	1.28

C. MatLab calculation for Self-consistency model

```
% (c) Juliane Kampichler 2017
%
clear;
close all;

iK = 101.85;
iG = 41.67;
mG = 1.28;
mK = 3.83;

%syms mG iG iK mK
syms sK ci
syms alpha sG
syms beta


% Perform arithmetic computations
alpha = 3*sK / (3 * sK + 4 * sG);

eqn1 = sK == mK + ci * (iK-mK) / (1 + alpha*((iK/sK)-1));

sK = solve(eqn1, sK);

beta = (6 * (sK + 2*sG))/(5 * (3*sK + 4 * sG));
```

```
eqn2 = sG == mG + ci * (iG - mG) / (1 + beta * ((iG/sG) -1));

% Solve for G* and return the conditions and parameters under which the
% solution holds true.
[sG, param, cond] = solve(eqn2, sG,'ReturnConditions',true);

% Refine Solution
% assume(cond);
%
% interval = [sG > mG, sG<iG];
%
% sGk = solve(interval, param);
%
% valsG = subs(sG, param, sGk)
```

SOLUTION

The program gives for the shear modulus of the porous material, G^* (= sG in MatLab nomenclator) four approximations, which are necessary to enable a solution. The variable z, is a substitution variable, to transform the not solvable polynomial of fifth order into a solvable polynomial fourth order.

```
sG =

 root(z^4 - (z^3*(10274800000*ci - 22707400000))/160000000 - (z^2*(1533122100000*ci - 806421568500))/160000000 - (z*(3231310409505*ci - 393178694490))/160000000 - 29258753013/2500000, z, 1)

 root(z^4 - (z^3*(10274800000*ci - 22707400000))/160000000 - (z^2*(1533122100000*ci - 806421568500))/160000000 - (z*(3231310409505*ci - 393178694490))/160000000 - 29258753013/2500000, z, 2)

 root(z^4 - (z^3*(10274800000*ci - 22707400000))/160000000 - (z^2*(1533122100000*ci - 806421568500))/160000000 - (z*(3231310409505*ci - 393178694490))/160000000 - 29258753013/2500000, z, 3)

 root(z^4 - (z^3*(10274800000*ci - 22707400000))/160000000 - (z^2*(1533122100000*ci - 806421568500))/160000000 - (z*(3231310409505*ci - 393178694490))/160000000 - 29258753013/2500000, z, 4)
```